Material anisotropy in Wire and Arc Additively Manufactured structures

Ben Weber

WAAM in the construction industry

Additive manufacturing has found widespread research interest and industrial applications over the past decades. However, the construction industry is only starting to explore the benefits of this promising technology, mainly due to a lack of design guidelines that provide the necessary quality assurance procedures and standardise the manufacturing process [1,2,3]. Wire and Arc Additive Manufacturing (WAAM) is a metal 3D printing technique where an industrial robotic arm is used in conjunction with a conventional welding unit to deposit metal and create objects, with few limitations to their size or shape (Fig 1) [4].

Compared to other additive manufacturing methods, WAAM is especially interesting for the construction industry due to its high deposition rate (4-9 kg/h [5]) and the inherent surface tension of the molten metal which allows for overhanging structures to be printed without the need for support material [5]. Topologically optimised structures made possible by the digitally enabled manufacturing process, can exhibit the same structural strength but with considerably reduced material compared to conventional manufacturing techniques, which reduces the weight of the printed part and also its cost owing to the shorter manufacturing time [6]. These benefits also present interesting opportunities for the aerospace construction sector, which could allow for the production of large structural metal parts in space or other planetary bodies [7].

In contrast with conventionally produced stainless-steel structures, which behave in an isotropic way, those produced by WAAM can present considerable anisotropy [8,9,10]. Owing to the production process, where the crystallographic structure of the metal orientates itself relative to the distinct thermal gradient of the different layers during solidification, the mechanical behaviour of a structure is dependent on the printing direction relative to the loading direction [11]. An additional factor contributing to the anisotropic material behaviour is the surface finish of printed structures; surface undulations lead to a nonhomogeneous cross-sectional area, further increasing the directional dependency of the material [11]. Mainly owing to a scarcity of testing data [12], this anisotropic material behaviour is currently not fully understood, and no design and reliability recommendations can be given [5].

Material analysis

Prior work on analysing the material behaviour of Grade 308LSi stainless-steel WAAM [11] has determined that thin-walled stainless-steel WAAM can best be characterised as a planar orthotropic material. Proof and yield stresses as well as Young's moduli of the printed material have been derived for different printing directions, thicknesses and surface finishes. However, to accurately model the complete planar orthotropic behaviour and be able to simulate the material in finite element analysis (FEA), additional material characteristics, such as the Poisson's ratios and plastic behaviour, are needed.

This thesis uses the data of tensile tests from 37 as-built coupons (undulating surface from production still present) and 12 machined coupons (undulating surface removed using an end-mill, see Fig 2) to determine the missing material characteristics. The coupons were cut from larger plates at three different angles (0°, 45° and 90°) to the printing orientation to determine the material characteristics in these directions (see Fig 3) and at 2 different thicknesses for the as-built coupons (3.5 mm and 8.0 mm). Surface strain fields of the coupons during testing were determined via digital image correlation (DIC) which allowed, in addition to the longitudinal and transverse strains, for thickness strain measurements, which are very difficult to accurately determine with traditional methods. From the stress-strain curves produced by these tests, a clearly anisotropic behaviour can immediately be detected (Fig 4). All three test orientations (0°, 45° and 90°) exhibit a distinctly different behaviour.

Elastic material behaviour

Elastic Poisson's ratios are determined from longitudinal and transverse surface strains in the elastic range. Fig 5 shows the individual Poisson's ratios derived from each machined coupon test as well as a numerically optimised model fitting the experimental data to a theoretical planar orthotropic material model. It can clearly be seen that the individual tests follow the expected model very closely. Fig 5 additionally shows how the Young's and shear moduli change over different off-axis loading angles. The elastic material constants derived from the tests: Young's moduli E, Poisson's ratios ν and shear moduli G, see Table 1, show an anisotropic material behaviour of the WAAM structures and correlate well between the different material thicknesses and surface finishes. The variations in the material characteristics between the different coupon types was attributed to the varying influence of surface undulations depending on the coupon's thickness and surface finish. It is shown that the influence of the surface undulations becomes less important in thicker cross sections and approaches the material characteristics of machined structures.

Table 1: Material parameters WAAM [14]

	Machined coupons			As-built 3.5 mm			As-built 8.0 mm		
θ (°)	E_x (GPa)	ν_{xy} ()	G_{xy} (GPa)	E_x (GPa)	ν_{xy} ()	G_{xy} (GPa)	E_x (GPa)	ν_{xy} ()	G_{xy} (GPa)
0	143.7	0.419	100.9	137.4	0.458	98.1	142.8	0.443	95.0
45	219.5	0.088	50.1	188.5	-0.039	41.0	196.3	0.033	44.9
90	139.2	0.406	100.9	96.0	0.320	98.1	110.4	0.343	95.0

Plastic material behaviour

To accurately model the plastic material behaviour, the standard unidirectional yield model needs to be expanded to adapt to different material orientations. Plastic yield ratios (R-values), which can be determined from yield stresses using the Hill's yield criterion, are used. Their effect can be seen in the change of shape from the widely used von Mises yield surface (for isotropic materials) to the Hill's yield surface, see Fig 6. These yield stress ratios are used in FE to change the shape of the unidirectional material yielding curve at the different orientations.

The research from this thesis was used as a basis for the publication of two papers exploring the anisotropic material response of additively manufactured stainless steel using WAAM [13,14].

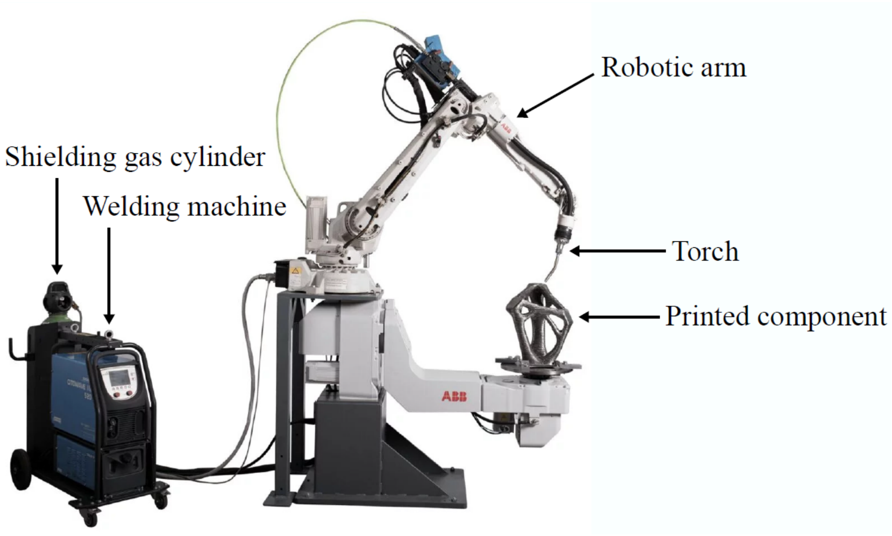

Fig 1: WAAM system [14]

Fig 2: (a) As-built coupon and (b) Machined coupon [11]

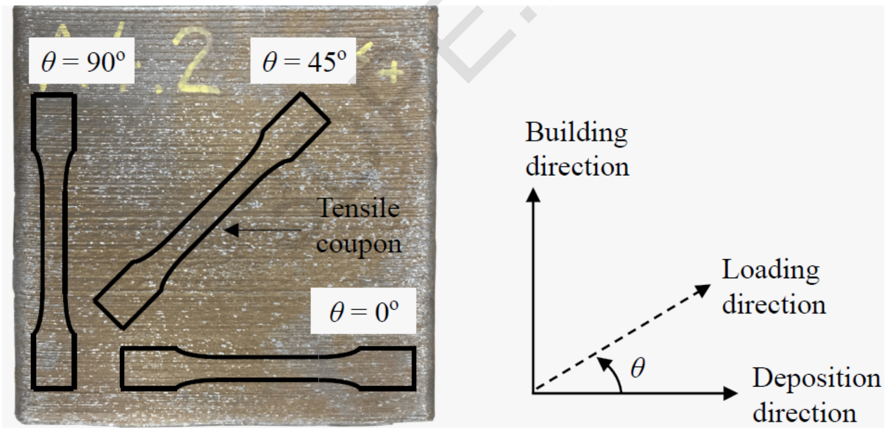

Fig 3: Coupon orientation relative to the deposition and building direction [14]

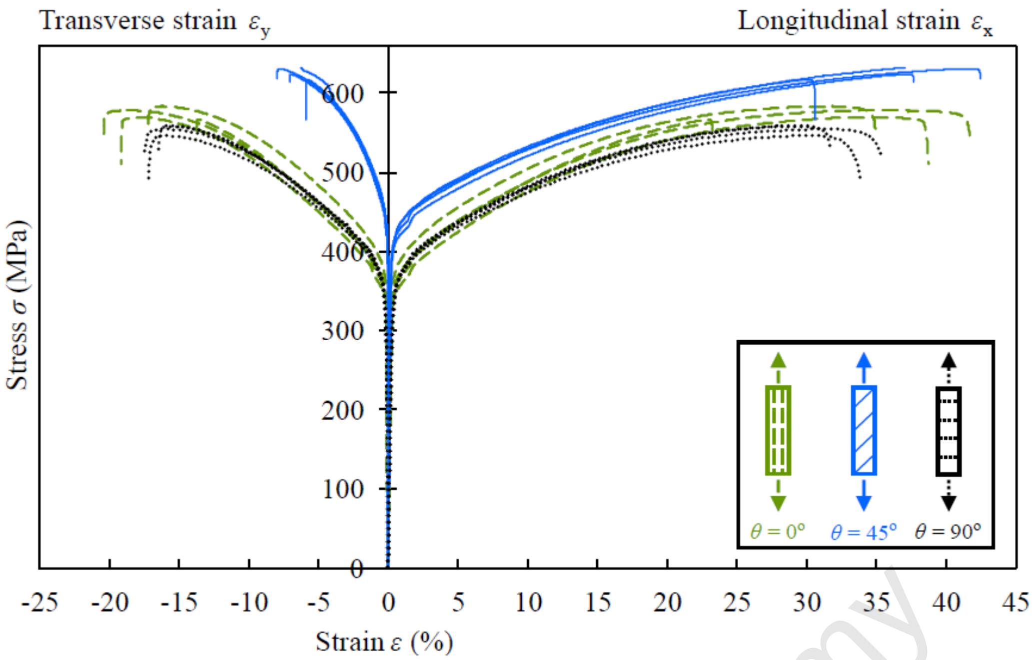

Fig 4: Stress–strain responses of the machined specimens [14]

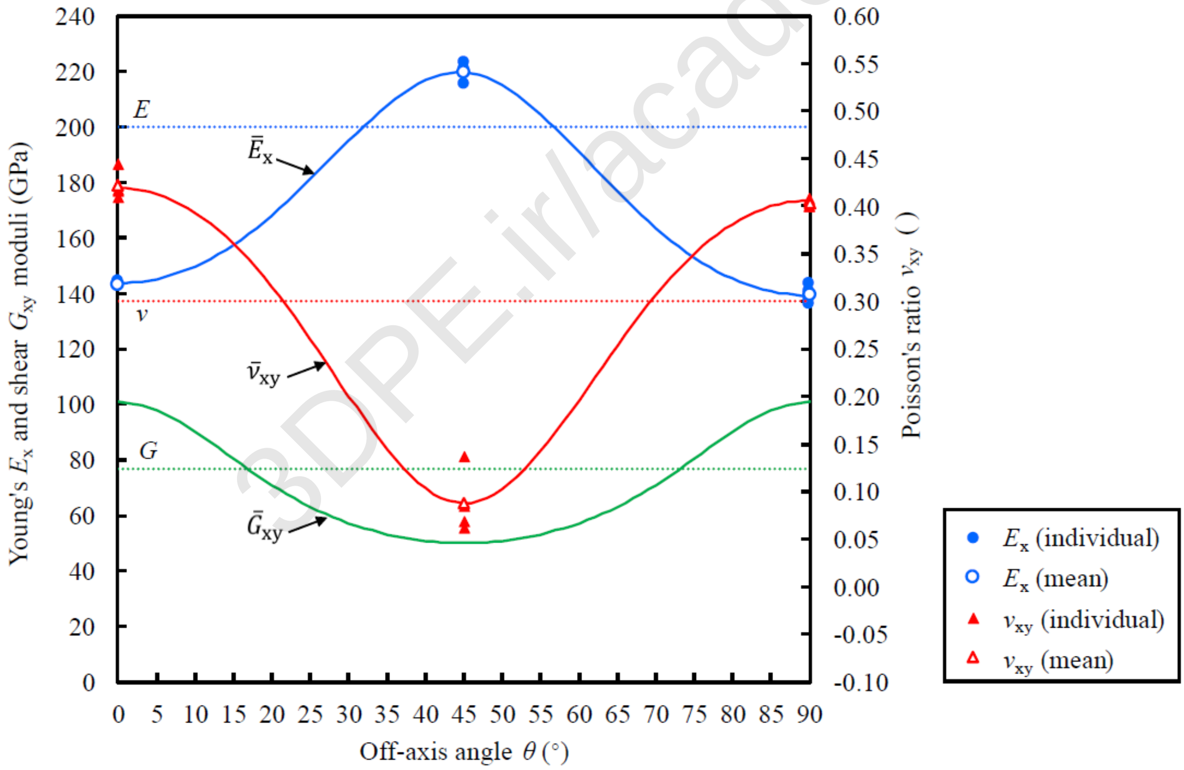

Fig 5: Variation of elastic constants with θ in the machined coupons. The horizontal dotted lines indicate the typical properties of conventionally produced (isotropic) stainless steel. [14]

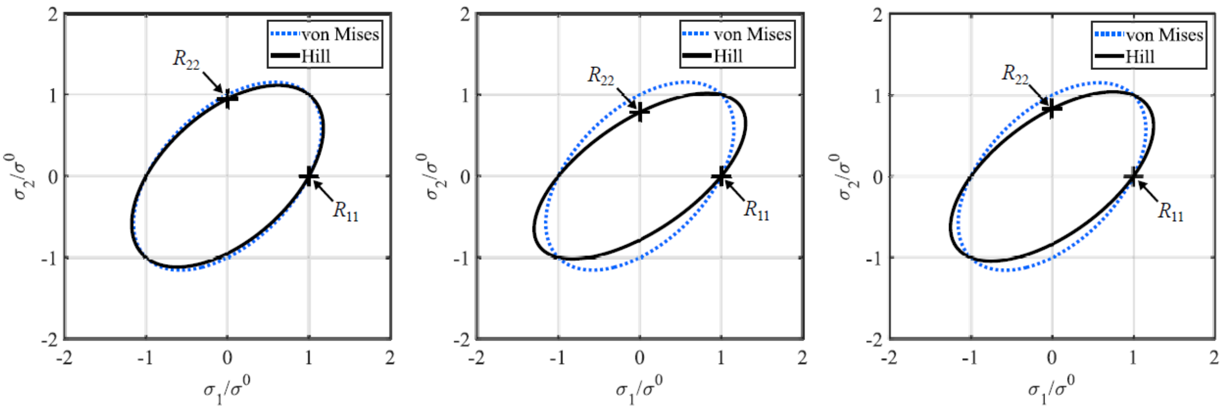

(a) Machined coupons (b) As-built 3.5 mm coupons (c) As-built 8.0 mm coupons

Fig 6: Normalised yield surfaces for the 3 coupon types using the von Mises and Hill yield criteria. [14]

[1] Gao, W.; Zhang, Y.; Ramanujan, D.; Ramani, K.; Chen, Y.; Williams, C.B.; Wang, C.C.L.; Shin, Y.C.; Zhang, S.; Zavattieri, P.D. (2015) *The status, challenges, and future of additive manufacturing in engineering*. Computer Aided Design **69**, 65–89.

[2] Wu, P.; Wang, J.; Wang, X. (2016) *A critical review of the use of 3-D printing in the construction industry*. Automation in Construction **68**, 21–31.

[3] Gardner, L.; Kyvelou, P.; Herbert, G.; Buchanan, C. (2020) *Testing and initial verification of the world's first metal 3D printed bridge.* Journal of Constructional Steel Research **172**, 106233.

[4] Lange, J.; Feucht, T.; Erven, M. (2020) *3D printing with steel: Additive Manufacturing for connections and structures*. Steel Construction **13**, 144–153.

[5] Buchanan, C.; Gardner, L. (2019) *Metal 3D printing in construction: A review of methods, research, applications, opportunities and challenges*. Engineering Structures **180**, 332–348.

[6] Cavazutti, M.; Baldini, A.; Bertocchi, E.; Costi, D.; Torricelli, E. (2011) *High performance automotive chassis design: a topology optimization based approach*. Structural and Multidisciplinary Optimization **44**, 45-56.

[7] Joshi, S.C.; Sheikh, A.A (2015) *3D printing in aerospace and its long-term sustainability*. Virtual and Physical Prototyping **10**, 175-185.

[8] Laghi, V.; Palermo, M.; Tonelli, L.; Gasparini, G.; Ceschini, L.; Trombetti, T. (2020) *Tensile properties and microstructural features of 304L austenitic stainless steel produced by wire-and-arc additive manufacturing*. International Journal of Advanced Manufacturing Technology **106**, 3693–3705.

[9] Wang, L.; Xue, J.; Wang, Q. (2019) *Correlation between arc mode, microstructure, and mechanical properties during wire arc additive manufacturing of 316L stainless steel*. Materials Science and Engineering A **751**, 183–190.

[10] Haghdadi, N.; Laleh, M.; Moyle, M.; Primig, S. (2021) *Additive manufacturing of steels: a review of achievements and challenges*. Journal of Materials Science **56**, 64–107.

[11] Kyvelou, P.; Slack, H.; Mountanou, D.D.; Wadee, A.M.; Britton, T.B.; Buchanan, C.; Gardner, L. (2020) *Mechanical and microstructural testing of wire and arc additively manufactured sheet material*. Materials and Design **192**, 108675.

[12] Luecke, W.E.; Slotwinski, J.A. (2014) *Mechanical properties of austenitic stainless steel made by additive manufacturing*. Journal of Research of the National Institute of Standards and Technology **119**, 398–418.

[13] Hadjipantelis, N.; Weber, B.; Gardner, L. (2021) *Characterisation of the anisotropic response of wire and arc additively manufactured stainless steel.* ce/papers **4**, 1757-1766.

[14] Hadjipantelis, N.; Weber, B.; Buchanan, C.; Gardner, L. (2021) *Description of anisotropic material response of wire and arc additively manufactured thin-walled stainless steel elements*. Thin-walled structures (Accepted).

materials

Article

Optimization of Wire Arc Additive Manufacturing (WAAM) Process for the Production of Mechanical Components Using a CNC Machine

Anamaria Feier [1,*], Ioan Buta [1], Cosmina Florica [2,3] and Lucian Blaga [4]

[1] Department of Materials and Manufacturing Engineering, Mechanical Faculty, Polytechnic University Timisoara, Bl. Mihai Viteazu No. 1, 300222 Timisoara, Romania
[2] Department of Computers and Exact Sciences, Faculty of Engineering, Ioan Slavici University, Paunescu Podeanu Street No. 144, 300569 Timisoara, Romania
[3] Mechanical Faculty, Polytechnic University Timisoara, Bl. Mihai Viteazu No. 1, 300222 Timisoara, Romania
[4] Department Solid State Materials Processing, Institute for Materials Mechanics, Helmholtz Zentrum Hereon, 21502 Geesthacht, Germany
* Correspondence: anamaria.feier@upt.ro; Tel.: +40-256-403-612

Abstract: The paper presents a CNC component manufacturing process using the WAAM process. The study depicts all the execution steps of a component from the CAD drawing, deposition procedure (technological parameters, times, layers, etc.), examination, and economic calculation. The manufacturing of this component using WAAM is more advantageous given the fact that the execution time and delivery are significantly shorter, mainly when a single piece is required and also when discussing the raw material used, usually expensive titanium alloys. For example, for Ti-6AI-V used in the aircraft industry, for which the material price is about 90 Euro/kg, the costs for obtaining a given component using the WAAM process will be about 497 Euro/piece compared to 1657 Euro/piece when using another manufacturing process, as it is shown in this paper. In conclusion, additive manufacturing can easily become a feasible solution for several industrial applications when it replaces a classic manufacturing process of a single component or replacement products, even simple-shaped.

Keywords: additive manufacturing; automotive; manufacturing costs; wire arc additive manufacturing

Citation: Feier, A.; Buta, I.; Florica, C.; Blaga, L. Optimization of Wire Arc Additive Manufacturing (WAAM) Process for the Production of Mechanical Components Using a CNC Machine. *Materials* **2023**, *16*, 17. https://doi.org/10.3390/ma16010017

Academic Editors: Stanislaw Legutko and Antonino Recca

Received: 14 October 2022
Revised: 23 November 2022
Accepted: 12 December 2022
Published: 20 December 2022

1. Introduction

Additive manufacturing (AM) is a production method based on the addition of layered material, thus obtaining functional products. Additive fabrication or 3D printing is very popular nowadays because it covers a series of processes designed to produce parts or assemblies from different types of materials. Basically, 3D printing turns a three-dimensional design into a physical object. The common element of all 3D printing technologies is the way of obtaining these components—overlapping layers of material that lead to the final shape of the printed object [1].

In 3D-printing processes, several materials can be used, some of which we expect—plastic, metals, ceramics, or even concrete, but also surprisingly paper or edible materials such as chocolate. Regarding the 3D printing of metals, in 1926, Ralph Baker (USA) patented the use of the electric arc as a heat source to generate 3D objects by layer by layer-by-layer deposition [2–4].

As shown in Figure 1, the WAAM—Wire Arc Additive Manufacturing—process offers advantages over other processes in terms of the mechanical properties obtained, the dimensions that can be achieved, the deposition rate, and low costs. The disadvantages of this process are the limitations related to the complexity of the shapes that can be achieved as well as the low accuracy that involves further machining [5].

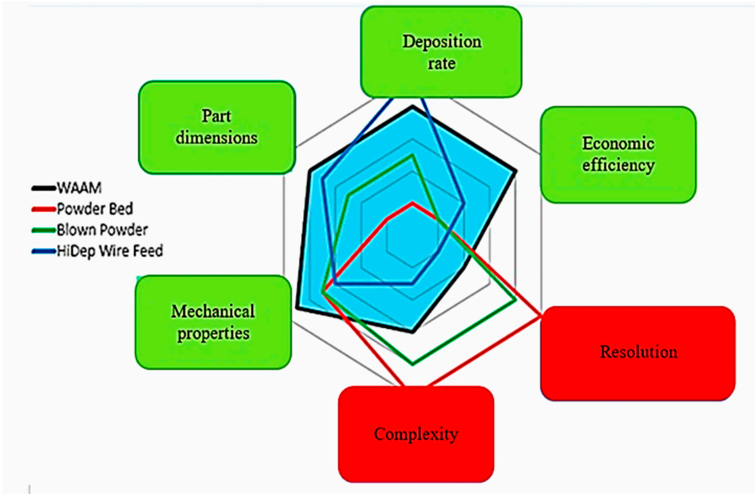

Figure 1. Comparison of advantages and disadvantages between different methods of AM [5].

Wire Arc Additive Manufacturing (WAAM) is a manufacturing process with arc energy used to melt and deposit the filler material in successive layers to form parts with homogeneous structure [6,7]. Using this process, different components or entire structures such as the 3D-printed pedestrian bridge designed by Joris Laarman and built by Dutch robotics company MX3D can be obtained [8].

Unlike the most common AM processes in cases where metal powders are used, the WAAM principle is melting metal wire using the electric arc as a heat source. The process is controlled by a robotic arm and the work piece is built on a substrate material (a support plate), and, in the end, the workpiece/component can be cut once finished or the substrate material can be embedded in the finished product. The wire, when melted, is deposited in the form of a welded seam on the substrate. As the successive seams are deposited, they create a layer of metal material. The process is then repeated, layer by layer, until the metal piece is completed [5,9,10].

The research in wire arc additive manufacturing (WAAM) is being driven by the need to further improve the manufacturing efficiency of engineering structures. Using WAAM, components very near to net shape preforms can be produced without the need for complex tooling or dies, thus showing potential for significant cost and lead-time reductions, increased material efficiency, improved mechanical performance, and reduced inventory and logistics costs. The process was patented in 1920 and is probably the oldest but least talked about of the range of additive manufacturing (AM) processes (commonly known as 3D printing) [8,11,12]. By using wire as feedstock, the basic process has been used to perform local repairs on damaged or worn components, and to manufacture round components and pressure vessels in the past. The advantage of computer-aided design and manufacturing (CAD/CAM) software has made Additive Manufacturing, in general, possible, with this process being an area of significant development in recent years, with a resolution of approximately 1 mm and deposition rate between 1 and 10 kg/hour or more (depending on type of arc source) [13–15].

The present study highlights the possibility of producing some components using the WAAM (Wire Arc Additive Manufacturing) process. In Figure 2, an example of an exploratory automotive component manufactured and designed using WAAM is presented by the same working collective that also developed this CNC component from the present research. A support plate was used to manufacture the product; after optimizing the deposition parameters, the piece was obtained in a short time, with the unprocessed specimen (only the deposited area) obtained in 54 min. Subsequent machining on the latter took an additional 2–3 h [16,17]. The component obtained in Figure 2 was produced using the same principle as the component that is described in detail in this study from the procedure of deposition to the part of examination and cost.

(**a**) (**b**)

Figure 2. Exploratory study—automotive component using the WAAM—of first trials to obtain finished products with this process, prior (**a**), post-finishing (**b**).

2. Materials and Methods

This section presents the procedure of obtaining the piece/component. The piece was obtained by deposition layer-by-layer using the WAAM process. The material used was S355J0, and the filler material was G 42 4 M21 3Si1 with the following mechanical characteristics:

- Yield strength of 380 N/mm^2 (depending on shielding gas);
- Tensile strength of 490 N/mm^2 (depending on shielding gas).

The shielding gas used was Ar85%-$CO_2$15%. Technological parameters of the working procedure of wire arc additive manufacturing (WAAM) are presented in Table 1.

Table 1. Technological parameters of working procedure of wire arc additive manufacturing.

Technological Parameters	Value
Polarity	CC+
Amperage Is (A)	125
U_a operation voltage (V)	21.8
Rate of welding (m/min)	5.4
Gas flow Ar85%-$CO_2$15% (L/min)	15
Medium linear energy (J/cm)	3096
Length of the free end (mm)	9
Positioning rotational speed (°/s)	4.93

The minimum required width of the deposited material should be 10 mm to provide sufficient material as machining addition. Initially, a trial was conducted for producing the piece in one single pass/layer, but the width of the deposited material, 8 mm, was not sufficient. Consequentially, the amperage (Is) was increased from 130 A to 180 A. It was observed that the first 2 layers reached the desired width, but the excessive residual heat accumulated in the workpiece or the too short of a cooling time led to an excessive melting of the layers deposited in the 3rd pass.

Taking these aspects into consideration, the following was established:

- The final part was produced with 2 passes/layer with a gap between layers of 4 mm;
- Amperage of 130 A;
- 15 L/min gas flow.

The infrastructure used in the experimental tests is the following:

1. Welding source: Sincosald Nova Plus 500 e inverter with Feeder 4R NSP wire feeder.
2. Shielding gas used: Argon 85% + CO_2 15% mixture (Corgon 18-Linde).
3. Yaskawa robot model MH 24—for welding gun operation.
4. Yaskawa positioning device model DK 250—capacity of 2500 kg used to fix and rotate the substrate material.
5. Protection, control, and robot control panel and positioning device.

The piece was obtained by depositing layer-by-layer on a pipe, as can be seen in Figure 3.

Figure 3. Steps from the working procedure of wire arc additive manufacturing.

2.1. Residual Stresses and Strains

To reduce the effects of stress and deformations, but also to guarantee the necessary processing addition, the workpiece was made by deposition/welding in a pilgrim's step in such a way as to allow sufficient cooling of the part between 2 consecutive layers.

During preliminary tests, it was established that a temperature of 300 °C at the beginning of consecutive layer deposition guarantees optimal deposition conditions. It was also checked that the temperature variation between the deposition of two consecutive layers was not greater than 5 °C. Temperature control during deposition was carried out using a Testo thermal imaging camera [18–20].

To monitor the temperatures in an efficient and consistent way, a reference point was chosen where temperatures were measured at the beginning of the weld/deposition seam and at the end of the weld/deposition seam on both welded sectors/diameters. For this purpose, the temperature measurement point was set as the end of the weld seam [21–24].

As seen in Figures 4 and 5, the temperature of the layer deposited at the end of the deposition was located around 500–540 °C, and before starting the deposition of the successive layer, a cooling time of the part down to 300 °C was required. Therefore, a cooling time between 2 and 2.5 min was applied.

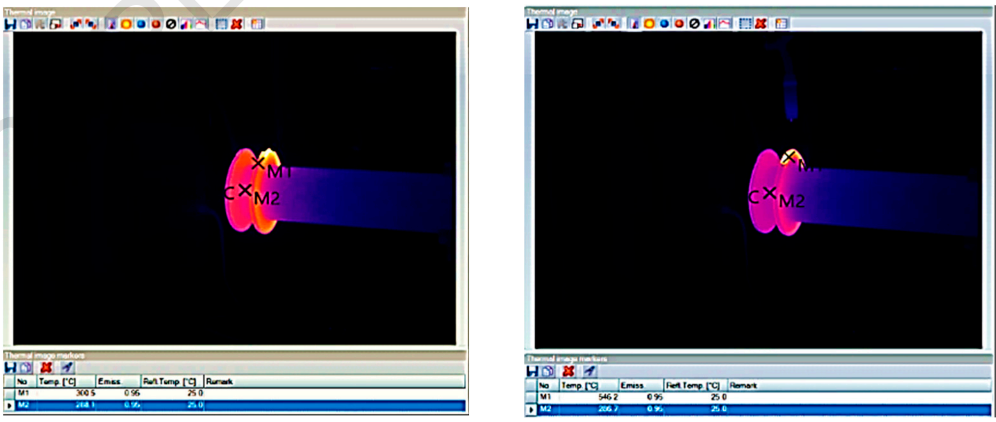

(**a**) (**b**)

Figure 4. Thermography of the weld seam at the diameter of 170 mm, layer no. 10. Before welding (**a**) and after welding (**b**).

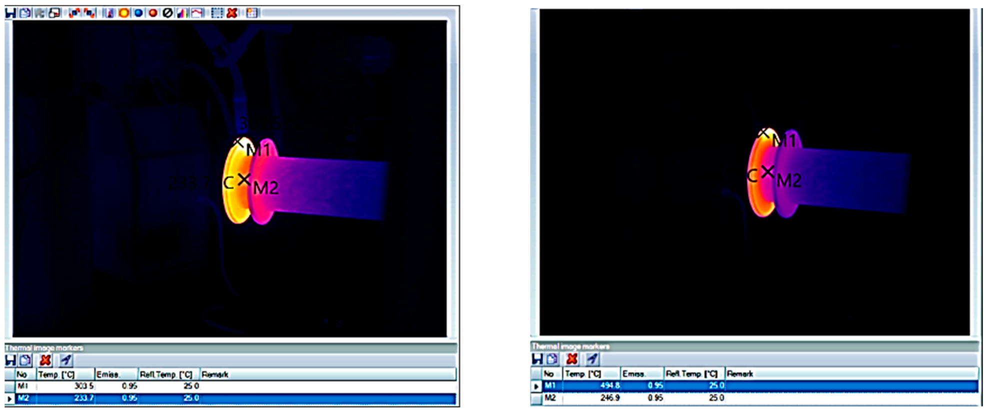

Figure 5. Thermography of the weld seam at the diameter of 195 mm, layer no. 15. Before welding (**a**) and after welding (**b**).

By analyzing the data, some preliminary conclusions can be drawn:

- The efficiency of the process for a single piece was only 45%. From a productive point of view, there were apparently massive losses. Nonetheless, the inefficiency of the process can be significantly diminished if two components were produced in parallel or by implementing an efficient cooling system.
- Deposition rate: it was necessary to perform 4 seams/layer instead of 2. If two parts had been produced in parallel, the amperage (Is) could have been higher because there would have been enough cooling time between the deposits.
- The maximum temperature of the deposited layer, i.e., 300 °C, before the start of the welding/deposition of the consecutive layer proved to be correct because, following the controls carried out, the deformation of the substrate material was less than 0.5 mm—measured at the inner diameter of the tubular substrate blank [25].

2.2. *Preparation of the Piece for Turning*

2.2.1. Cutting

The length of the tubular blank used as a substrate material was greater than the length required to manufacture the flange. Accordingly, excess material was removed with the help of an angle grinder.

2.2.2. Turning

Before the start of the turning operation, difficulties were encountered in centering the part in the lathe due to deformations of the inner diameter of the pipe (substrate material). These deformations were noticed before starting the welding/deposition process but were neglected because the clamping was carried out on the outer diameter that showed no deformations. Subsequently, in the turning phase, it was noticed that this deformation created positioning problems, so it was decided to build elements that would help center the piece in the lathe at the final turning phase. A phase of this procedure is shown in Figure 6 [26,27].

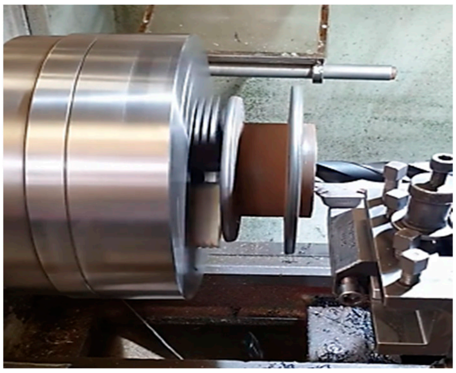

Figure 6. Excess material removals from the substrate.

2.2.3. Blasting and Preparing the Part for 3D Scanning

As shown in Figure 7a, a small number of oxides and silicates were formed on the surface of the work piece. These deposits were removed by sandblasting with Corindom to prepare the part for 3D scanning.

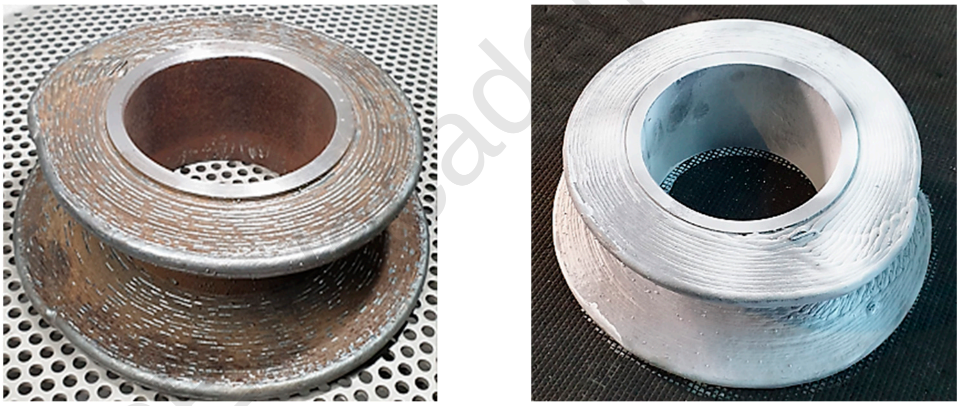

(**a**) (**b**)

Figure 7. Sandblasting of part. (**a**) Before sandblasting; (**b**) after sandblasting.

Three-dimensional scanning (Figure 8)—The purpose of this procedure was to check the deviations in the shape and quantity of the processing addition material of the part/component obtained in comparison with the 3D-designed model of the component [28].

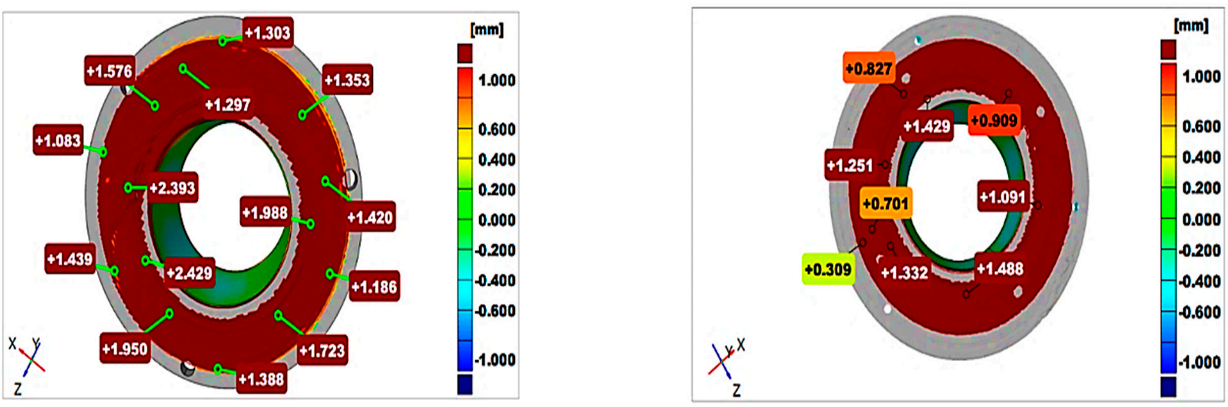

Figure 8. *Cont.*

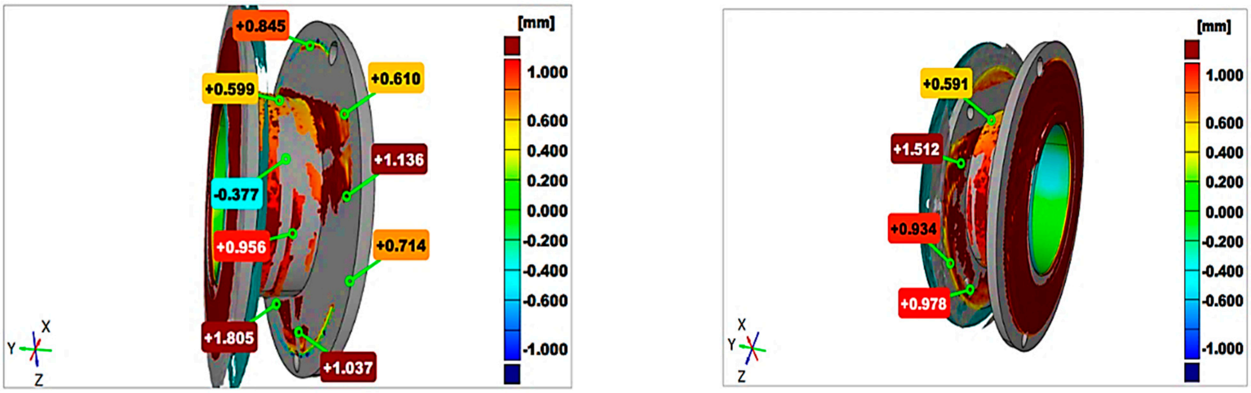

Figure 8. Three-dimensional Part Scan. Red areas represent the scanned part that are bigger than the 3D part, Green areas represent the scanned part is equal with 3D part, Blue areas are showing that the scanned part is smaller than the 3D part.

The 3D scanning revealed that the component built on the substrate material was not perpendicular to the axis of the part, but this deviation still allowed a functional finished product to be obtained.

2.2.4. Shaping the Piece

A conventional manual lathe was used for shaping. As mentioned above, it was necessary to build elements for centering and fixing the part in the lathe to minimize the eccentricity caused by the deformation inside the pipe and the slight lack of coaxiality between the axis of rotation of the tubular blank and the axis of rotation of the positioning device in the welding phase. This led to the effect of deposition in the walls of the component with a slight deviation in perpendicularity, as visible in Figure 9.

Figure 9. Shaping the piece.

It can be seen from the images below that the piece was dimensionally compliant.

2.2.5. Correction of the Part

The proper functioning of the produced component depends on the parallelism of the tooth planes of lying. To guarantee this, it was considered necessary to carry out its flat rectification operation. The rectification was performed on a specialized machine for flat surfaces. The procedure can be seen in Figure 10.

Figure 10. Grinding machine.

After rectification, the parallelism of the 2 settlement planes was checked, resulting in a deviation of less than 0.005 mm. Execution of holes for the piece fastening are presented in Figure 11.

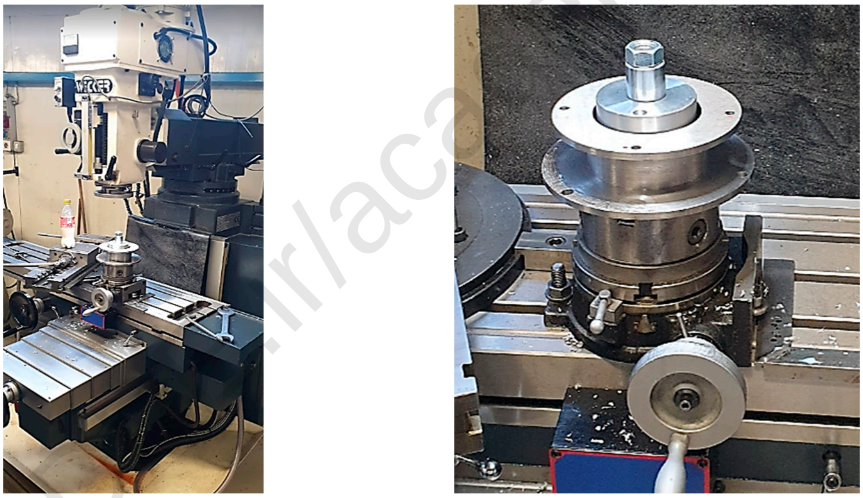

Figure 11. Fixing the part on the milling machine table.

3. Results and Examination

3.1. Visual Control

During the deposition of the piece/component, the quality of the deposition was controlled visually, layer by layer. No unconformity was noticed during the construction of the work piece by welding/deposition. All weld/deposition seams had a homogeneous, regular appearance, without unevenness, pores, cracks, or other defects.

After milling, the presence of pores was observed to be located at the root level, on a length of 9 mm. Observed pores had a diameter of less than 1 mm, as can be seen in Figure 12.

Possible causes of pores in the layers:

The surface of the substrate material could be contaminated with oily residues—although the substrate material was mechanically cleaned to remove the oxides, it is possible that oily residues remained on the surface of the part because the degreasing operation was not performed before the start of the welding/deposition.

Problems with the feed of the shielding gas—possible accumulation of moisture/condensation in the gas circuit. Considering the occurrence of imperfections, it is possible that the shielding gas line was self-cleaned as the welding/deposition process proceeded.

Too low welding/deposition speed—the porosities were discovered only in the area of the first seam deposited at both ends of the piece, i.e., at the base of the 170 mm disc, as well as at the base of the 195 mm disc.

High gas flow—as the welding/deposition was robotized and the fact that more layer-by-layer deposition was carried out, an increased gas flow was chosen (15 L/min) close to the maximum limit, to obtain a better protection and stability of the arc. However, this hypothesis does not explain the fact that imperfections were located only in the first weld seam. The study needs to be more in-depth with the next components that will be obtained by this process.

Figure 12. Presence of pores at the root layer, area inside of the red circle.

3.2. Dimensional Checks

The piece was measured using the sliding caliper. The parallelism between the two settlement planes was measured using a micrometric colon placed on a granite plate.

As can be seen from the images below (Figure 13), the piece was dimensionally compliant. The measured values were within the tolerance limits set in the execution drawing.

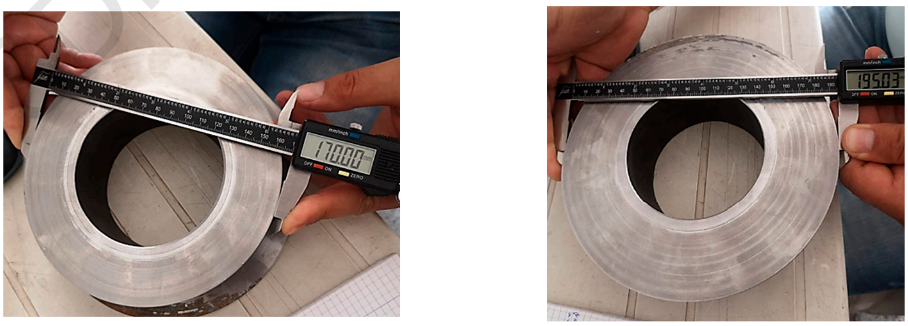

Figure 13. Dimensional control of the external diameters obtained after machining.

For the piece to serve the purpose for which it was built (fixing the universal to the positioner table), it is mandatory to have a perfect parallelism between the two settlement planes. For this purpose, an processing addition was left after turning, which was later removed in the phase of flat grinding [29–31].

3.3. Hardness Control

After flat grinding, the hardness of the part was checked using a portable instrument. The results of the tests are presented in Table 2 with details in Figure 14.

Table 2. Hardness tests.

Nr.crt.	Test 1 (HB)	Test 2 (HB)	Test 3 (HB)	Test 4 (HB)	Test 5 (HB)	Average (HB)
Zone 1	155	152	155	154	152	153
Zone 2	126	127	129	130	132	128

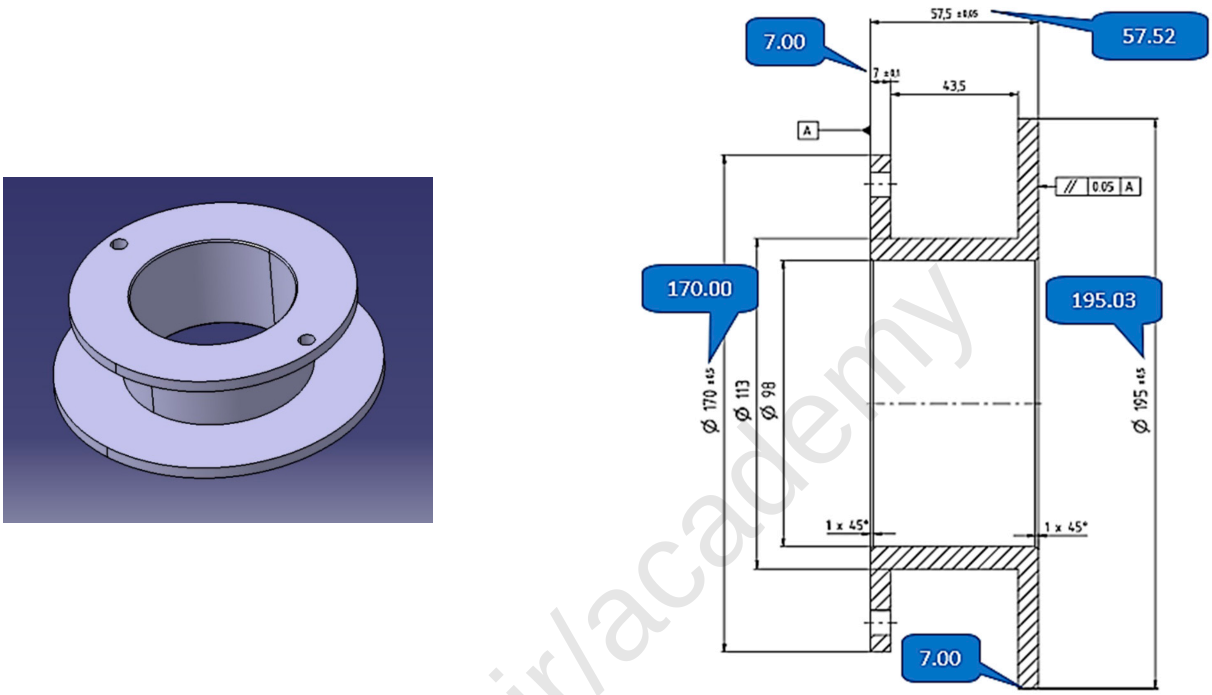

Figure 14. Measured part hardness values in different zones.

The hardness test was carried out in two distinct areas; namely, as can be seen in Figure 15, the two areas were very well explained (graphical and with text explanation).

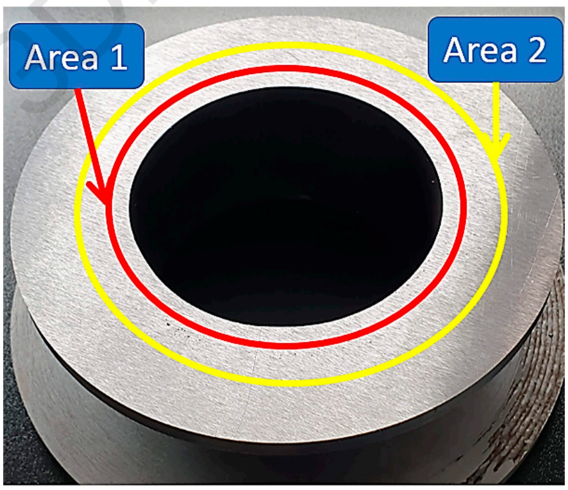

Figure 15. Highlighting the areas where hardness has been checked. Red circle: first deposition layer, Yellow circle: in the center of the successive deposited layers.

Zone 1 is in the closeness of the first deposition layer. In this area, the hardness was checked because that zone was the dilution zone between the substrate material and the first deposition layers.

It can be observed from Table 3 that the average hardness measured in zone 1 was 153 HB. This hardness corresponds to the hardness values indicated by the manufacturer of the substrate material (S 355J0).

Table 3. Mechanical characteristics and average of hardness tests.

Mechanical Properties	Value
Charge	S355J0
Rm (N/mm^2) (SR EN 10025-2)	510–680
R_{eH} (N/mm^2) (SR EN 10025-2)	355
HB (manufacturer)	154–208
HB (zone 1)	153
HB (zone 2)	128
R_{eH} of solid wire (N/mm^2)—from manufacturer	380
Rm of solid wire (N/mm^2)—from manufacturer	490

Zone 2 is the middle zone of the piece. As expected, the hardness of the part in the area achieved by deposition, 128 HB, was lower than in the dilution area due to the lower concentration of carbon in the addition material (0.08% vs. 0.20% for the S335J0) as well as due to the low cooling speed of the weld seams.

The chemical composition was also checked and compared with the results of the chemical composition declared by the manufacturer for the filler wire. The procedure can be observed in Figure 16.

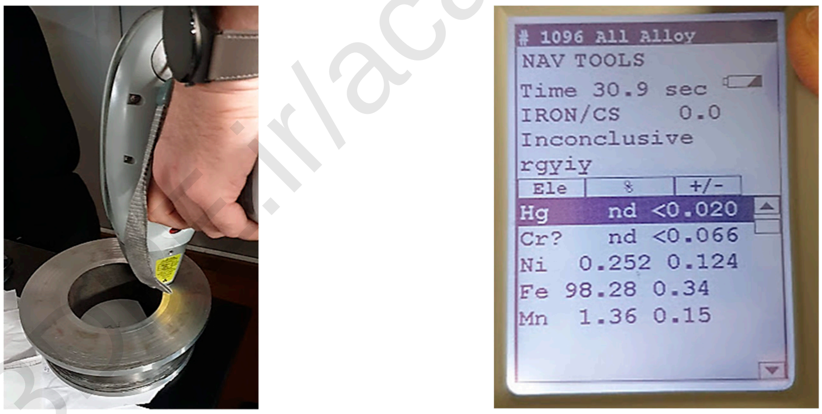

Figure 16. Comparison of results for filler wire. Chemical composition of the deposited material.

To verify the chemical composition of the material deposited layer by layer, a portable device branded Niton™ XL3t XRF was used. No values were recorded outside the tolerances specified by the wire manufacturer.

The section of examination was subject to microscopic analysis to observe the microstructure of the deposition material. The first step was to make the test-piece, namely the sample of the champion piece presented in Figure 17.

Another step was milling of the test tube presented in Figure 18, a step that was needed to prepare the sample for microscopic tests. The following step was to cut and adjust the sample for embedding in resin (step presented in Figure 19).

Preparation for resin embedding (Figure 18).

Embedding in resin and grinding/polishing (Figure 20).

Figure 17. Sample sampler from the champion piece.

Figure 18. Milling the test tube.

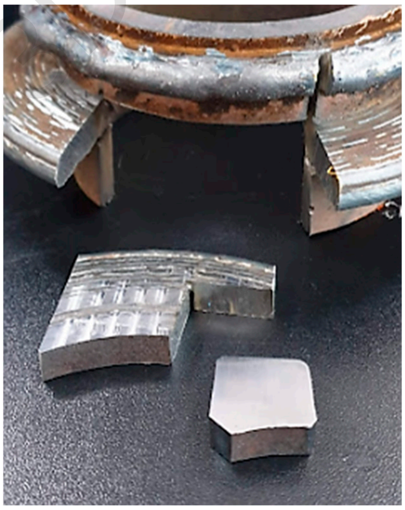

Figure 19. Preparation for resin incorporation.

Figure 20. Embedding in resin and grinding/polishing.

The test sample was progressively sanded, using abrasive paper of different grain sizes: 180, 600, 1200, 2500, and 4000, and after, it was polished using 1 µm diamond paste [32,33].

3.4. Metallographic Attack

The attack operation aimed to highlight the microscopic structure. The polished surface was attacked with the appropriate reactivity that selectively dissolves or stains the various constituents present, making it possible for them to be distinguished from each other.

The attack was carried out either by immersion or by swabbing the surface of the sample with a cotton wool piece.

Metallographic reagents differ depending on the nature of the material and the purpose of the attack (STAS 4203- 74). For this sample, for the reagent consisting of HNO_3, HCl, and CH_3COOH in the figure below (Figure 21) [34–36], all components of the reagent can be seen.

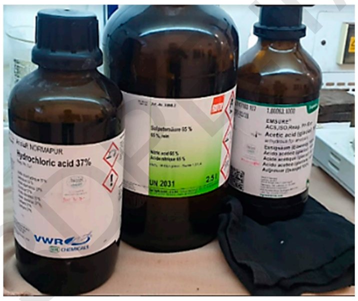

Figure 21. Reagent used to perform metallographic attack.

The sample was attacked when the prepared surface lost its brilliancy and became slightly matte (Figure 22). Too intense an attack distorts the structure. After the metallographic attack, the sample was washed with water then with alcohol and dried by pressing against a filter paper or under a stream of warm air after that was examined with metallographic microscope.

3.5. Microscopic Examination—Interpretation

The test tube was analyzed using a microscope connected to the PC. The test sample was extracted from the champion piece in such a way that on its surface, there were three distinct zones (Figure 22), namely:

Area 1—substrate material area.

Area 2—transition zone (dilution).

Area 3—the area deposited layer by layer, highlighting the deposited layers.

Figure 22 presents very well all areas of the sample, and each zone is very distinctive. The deposited layers can be seen very well even in a simple picture without microscopic analysis (yellow outlined arrows shown in Figure 22).

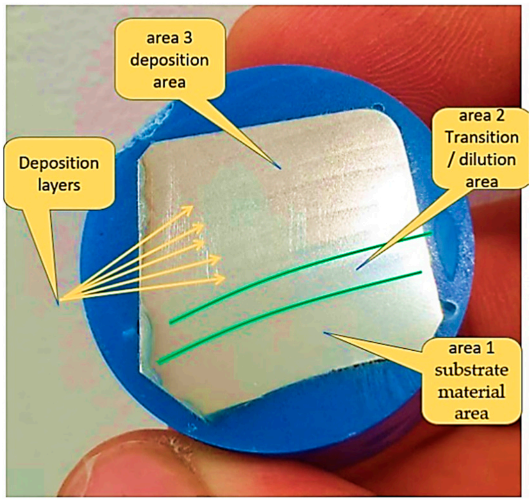

Figure 22. Highlighting microscopically analyzed areas.

Before the metallographic attack, a microscopic examination of the three areas mentioned above was carried out. No unconformities were identified in zone 1 and zone 2. In zone 3, in the deposited material layer by layer, the presence of very small pores was observed. The diameter of the porosities found in the additional material was less than 3 µm (Figure 23) (these are not serious defects but are defects within the limits recommended by the standards, and above in the article, possible cases of occurrence are explained) [37].

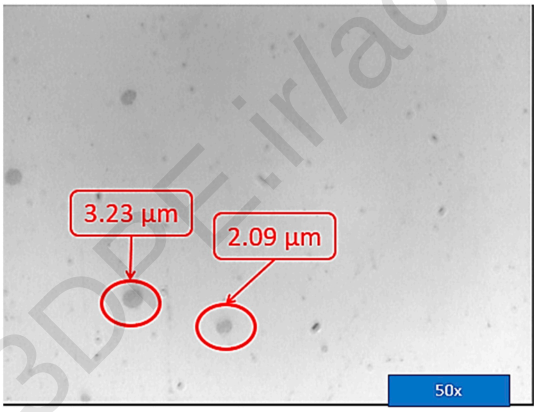

Figure 23. Microscopic porosities. Dimensional control of the porosities.

3.6. Substrate/Basic Material Area 1

The substrate material chosen was a tubular steel blank S355J0 with the mechanical characteristics shown in Table 3. The filler material used was Bohler G 42 4 M21 3Si1 electrode wire with a diameter of 1 mm, which has the characteristics shown in Table 4 [38,39].

Table 4. Detailing the material costs for the WAAM process and the percentage of material use.

Basic Material	Before Processing	After Processing
Length (mm)	60.0	57.5
External diameter (mm)	113.0	113
Internal diameter (mm)	98	98
Density (gr/cm^3)	7.8	7.8
Surface (mm^2)	2485.8	2485.8

Table 4. *Cont.*

Volume (cm^3)	1491.47	1429.33
Layer weight (gr)	1163.35	1114.97
Piece weight	4185	2861
Material weight of filler	3021.65	1746.13
Quantity of material removed after grinding (gr)	1276	
Percentage of material use (%)	57.79%	
Percentage of material loss after processing (%)	42.21%	
Electrode wire price G 42 M 21 3Sil (Euro/kg)	3.52	
Cost wire electrode/piece (Euro)	10.64	6.15
Loss of filler material/piece	−4.49	
material price S355J0 (Euro/kg)	1.45	
Cost of material/piece (Euro)	1.69	1.62
Loss of material/piece	−0.07	
Total material losses (Euro)	−4.56	

The wire electrode was an uncoated wire designed for low spatter and arc welding with high stability for a wide range of welding parameters.

ECOspark series uncoated wires feature high feed rates, high arc stability, and a low formation of oxides and silicates on the weld surface. This filler material is recommended for fully mechanized welding.

The substrate has a ferritic–pearlitic rolling structure, typical of cold-rolled materials, to which the parallax blades (dark in color) alternate with the ferritic grains (light in color) presented in Figure 24.

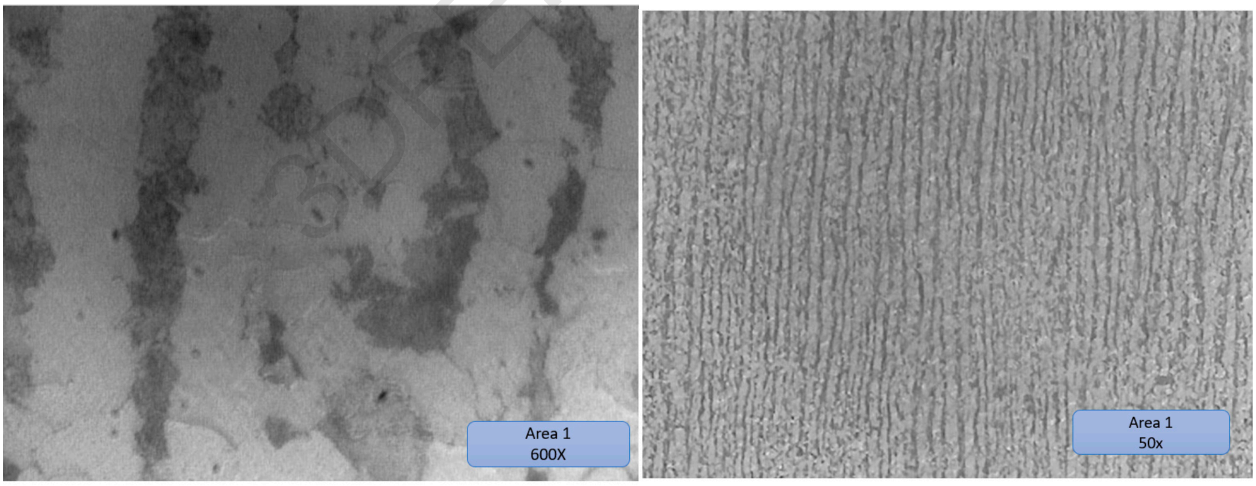

Figure 24. Substrate material area 1.

Substrate material areas 2 and 3 are presented in Figures 25 and 26, respectively.

The structure of zone 2 was a solidification structure, presenting a mixture of ferritic grains with a low volume of pearlitic elements with a random orientation. The higher share of ferrite is most likely due to the high speed when cooling the metal deposited in the first layer on the cold substrate, which partially suppressed the formation of perlite.

The subsequent thermal cycles in the analyzed area were not sufficient to restore the ferrite/pearlite ratio in the probable layer from the low peak temperatures or the short heating time in the analyzed area [40,41].

Zone 3 is a typical normalization zone, resulting from the thermal effect of successive layers on previously deposited layers with small equiaxial grains.

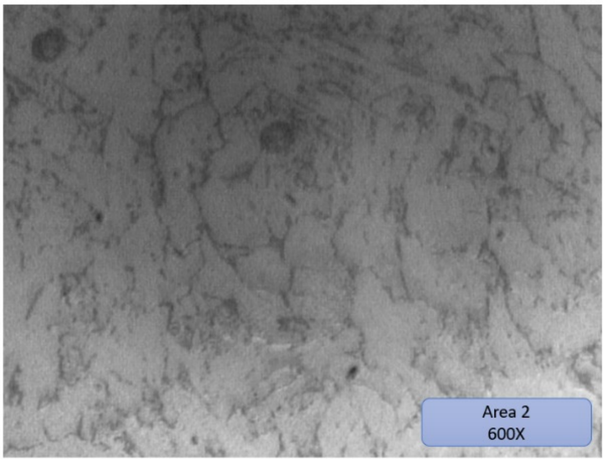

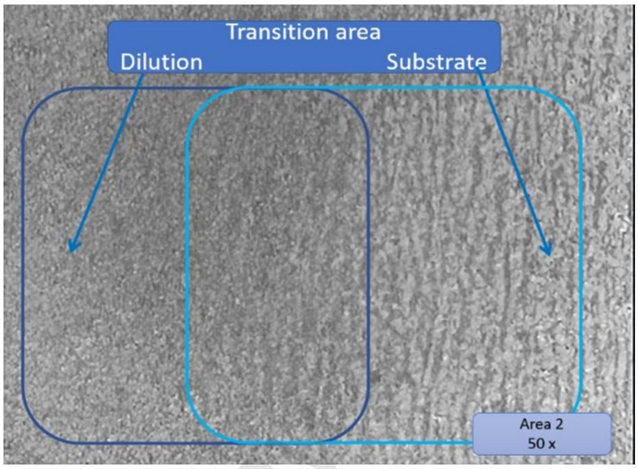

Figure 25. Substrate material area 2, with dilution, substrate, and their overlapped transition area marked in rectangles.

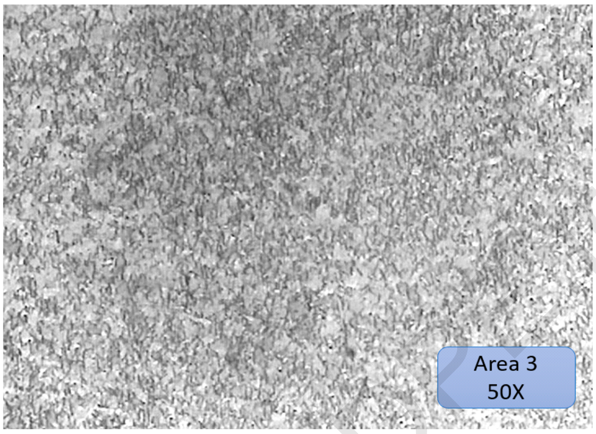

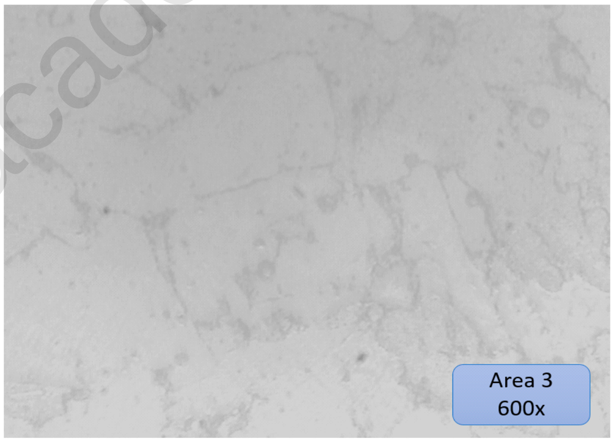

Figure 26. Substrate material area 3.

3.7. Economic Calculation

Ludwig von Mises addresses the problem of economic calculation—necessarily monetary—in his work Human Action: "Our civilization is inseparably linked to the methods of economic calculation. It would perish if we abandoned this so precious tool of action" [42]. Each step in the sphere of entrepreneurial activities shall be subject to verification by means of monetary calculation.

As shown in Figure 27, the total weight of the component produced was 2861 g, a weight very close to the weight calculated by the Solid Works design software; in SolidWorks, 2860.67 g was obtained.

4. Manufacturing Costs Using WAAM Materials

Table 4 shows the detailing of the costs of the raw material used to produce the component as well the calculation of the rate of use of the material. As can be seen, the total weight of the raw part was 4185 g, and after being needed to machine the workpiece, the weight dropped to 2861 g. Thus, for the flange produced using the WAAM process, the loss rate of the material was 42.21%, the equivalent of 4.56 Euro losses/piece produced.

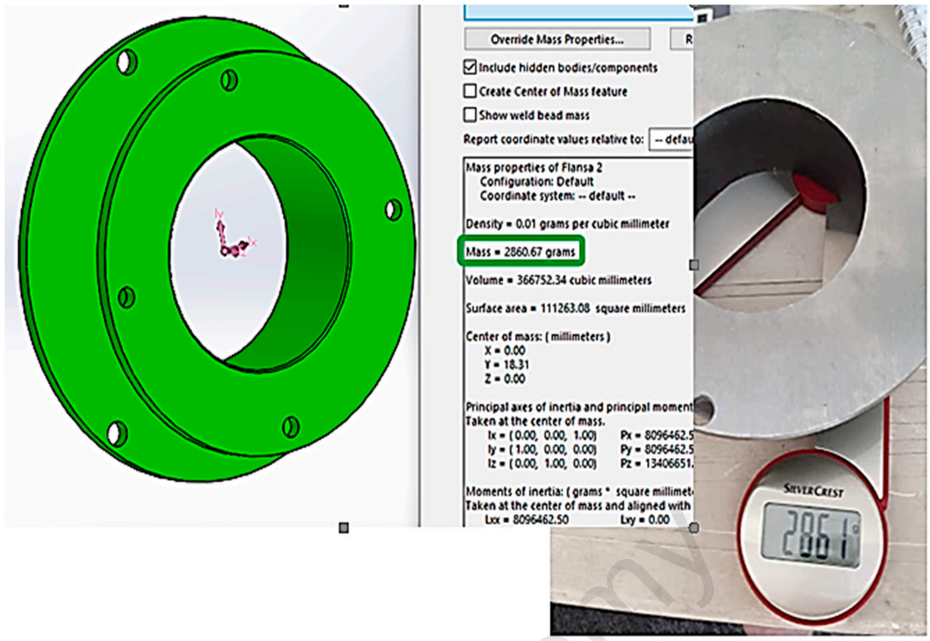

Figure 27. Comparison between the calculated part weight and the weight obtained.

4.1. Raw Material Costs Using the Classic CNC Cutting Process

As shown in Table 5, the weight of the raw material required was 17.153 g for the realization of the component that will have the final weight of 2.861 g. The result was a loss of 83.32% of the semi-finished product, i.e., the equivalent of 20.72 Euro losses/piece produced.

Table 5. Raw material cost and percentage material use for component construction using conventional CNC process.

Characteristics	Semi-Manufactured Article	Finished Article
Length (mm)	70.0	57.5
External diameter (mm)	200.0	113
Interior diameter (mm)	0	98
Density (gr/cm^3)	7.8	7.8
Surface (mm^2)	31,415.9	2485.8
Volume (cm^3)	21,991.15	1429.33
Weight (gr)	17.153	1114.97
Amount of material removed after milling (gr)	14,292	
Percentage of material use (%)	16.68%	
Percentage of material loss after processing (%)	83.32%	
Prefabricated price (Euro/kg)	1.45	
Semi manufactured cost/piece (Euro)	24.87	4.15
Loss of filler material (Euro/piece)	−20.72	

Comparison of the costs of workmanship WAAM–CNC cutting:

WAAM workmanship—The time required to achieve the component by the WAAM process was 202 min (it also includes the time needed to cool between two consecutive deposits). The time needed to obtain the finished piece, using a classic lathe, was 60 min. Thus, the total time to obtain the finished product was 262 min. It is, however, important to mention that the production process through the WAAM was not optimized in the sense to an unproductive time generated by the fact that the component had to cool down enough to be able to deposit the layer successively. The WAAM process can be reduced by half because the geometry and welding times for the developed workpiece are sufficient to produce two workpieces simultaneously. Thus, an optimized WAAM process would take about 160 min to produce a finished component.

CNC workmanship—For the comparison of manufacturing times using a CNC lathe, the GWizzard software Version number: 5.41, creator: CNCCookbook, location: Aptos, CA 95003 USA. (CNC Cookbook®) was used to simulate the time required to obtain the finished product (Figure 28).

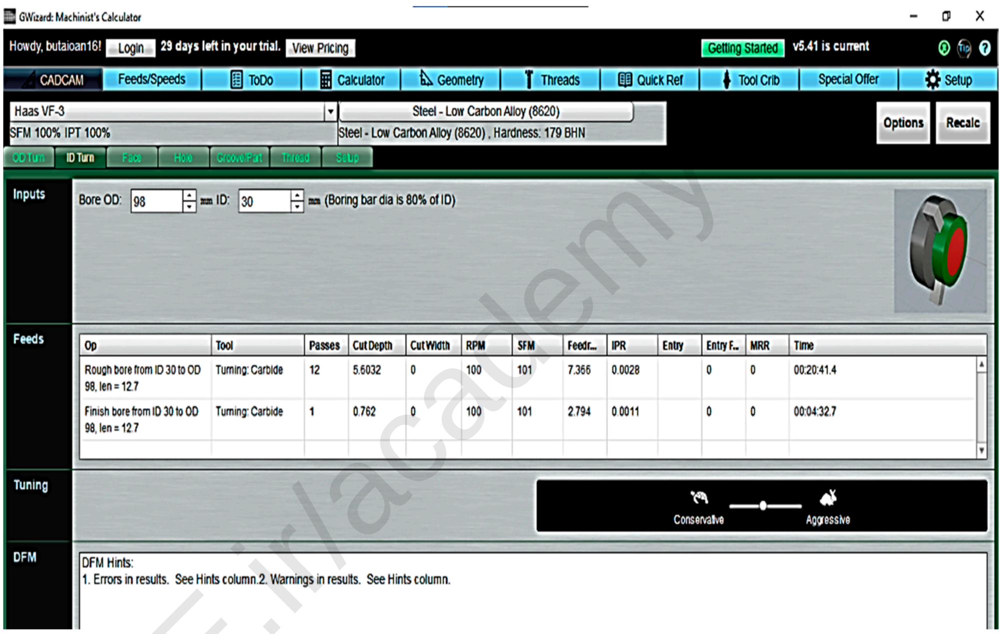

Figure 28. Software for CNC simulation turning the component.

Table 6 shows a detailing of the time required to perform the machining phases by cutting to obtain the finished part. Thus, the resulting total time was 151 min.

Table 6. Simulation of CNC lathe cutting times.

	Phase	Operation	Ø (mm)	Length (mm)	Times (hh:mm:ss)
Clamping 1	Face turning	Rough turn	200	3.23	0:12:45
		Turn finish	200	0.76	0:15:45
	outer diameter cutting	Rough turn	195.762	7	0:00:33
		Turn finish	195	7	0:00:54
		Rough turn	170.762	7	0:01:39
		Turn finish	170	7	0:00:47
		Rough turn	113.762	43.5	0:24:28
		Turn finish	113	43.5	0:03:13
	Inside diameter machining	Drilling	30	80	0:07:10
		Reaming	98.76	80	0:20:41
		Finish ream	98	80	0:04:32

Table 6. *Cont.*

Clamping 2	Face turning	Rough turn Turn finish	200 200	3.23 0.76	0:12:45 0:15:45
Clamping 3	Hole execution	Front drilling 1 Ø 10.5 × 3	10.5	7	0:15:00
Clamping 4	Hole execution	Front drilling 1 Ø 8.5 × 4	8.5	7	0:15:00
		Effective time to complete the piece:			**2:30:57**

4.2. WAAM Total Cost Comparison—CNC Cutting

Table 7 synthesizes the comparative costs between the optimized WAAM process, the optimized WAAM process, and the conventional CNC turning process for component execution. As can be seen, the optimized WAAM process is slightly more expensive than the classic CNC process due to the waiting times for cooling the part, but if the part is produced with optimized WAAM, the production costs decrease significantly, i.e., −33%.

Table 7. Comparison of WAAM-CNC component manufacturing costs.

Comparative Evaluation of Manufacturing Costs WAAM vs. CNC			
Cost	**Process WAAM Non-Optimized**	**Process WAAM Optimized**	**Classic Process (CNC)**
Cost of raw material/material (Euro)	12.32	12.32	24.87
Total production time (min) with WAAM * non-optimized	202	100	151
Total machining time after WAAM	60	60	0
Hourly rate (Euro)	30	30	45
Manpower cost (Euro/hour)	131	80	113
Total production cost (Euro)	**143**	**92**	**138**

* **WAAM optimized** = refers to the fabrication of 2 parts in parallel to eliminate/reduce the waiting time for cooling of the part before starting the welding of the successive layer.

However, a very important aspect remains to be mentioned: when producing the component and when making economic calculations, the price of the raw material was 1.45 Euro/kg for massive S355J0 and 3.52 Euro/kg for the filler material, so the impact of the waste of raw materials at the CNC milling is not very important.

If, hypothetically, the component were made of a titanium alloy, for example, Ti-6Al-V used in the aeronautical industry, where the cost of the material is about 90 Euros/kg, the workpiece manufactured by the WAAM process would have a cost of around 497 Euro/piece compared to 1657 Euro/piece in conventional CNC manufacturing, resulting in a reduction of 72% WAAM manufacturing costs (Table 8).

Table 8. Comparison of costs for piece/component of Ti-6Al-V.

Comparative Evaluation of Manufacturing Costs WAAM vs. CNC			
Cost	**Process WAAM Non-Optimized**	**Process WAAM Optimized**	**Classic Process (CNC)**
Cost of raw material/material (Euro)	376.65	376.65	1543.78
Total production time (min) with WAAM * non-optimized	202	100	151

Table 8. *Cont.*

Total machining time after WAAM	60	60	0
Hourly rate (Euro)	30	30	45
Manpower cost (Euro/hour)	131	80	113
Total production cost (Euro)	**508**	**457**	**1657**

* **WAAM optimized** = refers to the fabrication of 2 parts in parallel to eliminate/reduce the waiting time for cooling of the part before starting the welding of the successive layer.

5. Conclusions

The novelty of this study refers to the options a manufacturer can consider in order to produce a component, including small series, and gives them an idea of a more advantageous option using an innovative manufacturing process (WAAM) that is cost- and time-effective, compared to the other classic manufacturing processes. For example, to obtain a product for a small series of products if a CNC component is needed, and this piece usually is obtained by casting, this study demonstrates that it can be obtained in a justified time and with mechanical characteristics equivalent or even better than a cast component.

Depending on the specific situation, the following conclusions can be drawn:

- Regarding the economic aspect—the WAAM process is not recommended for the construction of parts with a simple geometry, because the classical manufacturing processes are much better optimized and adapted in this respect.
- Regarding the efficiency of the WAAM process in the case of the product presented in this paper, for a single workpiece, it was only 45%, and from a production point of view, the difference was represented as losses. The inefficiency of the process can be significantly diminished if two parts were produced in parallel or by implementing an efficient cooling system.
- In the case of deposition rate for the product developed in this study case: it was necessary to perform four layers instead of two. If two parts had been produced in parallel, the welding current could have been higher because there would have been enough cooling time between the deposits
- In terms of stresses and deformations, the situation resulted from parameters, and the maximum underpass temperature of the deposited layer, i.e., 300 °C, proved to be correct because following the controls carried out, the deformation of the substrate material was less than 0.5 mm—measured at the inner diameter of the tubular substrate blank.
- Regarding the resolution for the product developed in this study case, the quality of the surfaces of the parts obtained by WAAM was not very high, as further processing was required, but the quantity of material deposited in excess was good compared to the other advantages that this process brings.
- In terms of slicing, there are several pieces of software on the market that provides the interface between the CAD model and the robot's operating program, but due to the geometric complexity of the parts, the diversity of materials, and the numerous final uses of the finished products, there are real difficulties in correctly programming welding cycles that may differ from layer to layer within the same part.

In the deposited material layer by layer, the presence of very small pores was observed but the diameter of the porosities found in the addition material was less than 3 µm. The quality of the part was higher, the part obtained by layer-by-layer deposition using the WAAM process, and there was a negligible porosity induced in the manufacturing process, which was distinguished by homogeneity of the deposited material.

In terms of hardness of the part in the area achieved by deposition(128 HB), the hardness was lower than in the dilu-tion area due to the lower concentration of carbon in the filler material (0.08% vs. 0.20% for the S335J0), as well as due to the low cooling speed of the weld seams.

Another conclusion of this study is the importance of correct programming of the robot when moving on height. The robot arm, or welding gun, must have an axis of vertical movement perpendicular to the axis of rotation of the workpiece for perpendicular deposition of the walls-component on the substrate surface. A lack of this perpendicularity may, as with coaxially, leads to flatness defects.

The time required to achieve the component by the WAAM process was 202 min. The time needed to obtain the finished product, using a classic lathe, was 60 min. Thus, the total time to obtain the finished product was 262 min. The WAAM process can be optimized in terms of times by producing two parts simultaneously. An optimized WAAM process would take about 160 min to obtain a finished CNC component [43].

A significant point in the production of the part and in the economic calculations is that the price of the raw material was 1.45 Euro/kg for S355J0 steel and 3.52 Euro/kg for the filler material, so the impact of raw material waste in CNC milling is not very important, but if the part were made of a titanium alloy, e.g., Ti-6Al-V used in the aircraft industry where the material cost is about 90 Euro/kg, the part obtained by the WAAM process would cost about 497 Euro/piece compared to 1657 Euro/piece in conventional CNC manufacturing, resulting in a −72% reduction in manufacturing costs by the WAAM process.

This study can be continued and divided in several directions as follows:

- Studying the possibility of producing the flange by executing only two weld seams per layer instead of the four current seams as well.
- Studying the impact on the mechanical properties of the part.
- Using a forced cooling system with cooled air at low temperatures (−20 °C, −30 °C) and studying the effects of forced cooling on the mechanical properties of the part.

Author Contributions: The authors contributed to this research work as follows: conceptualization, A.F. and L.B.; methodology, I.B. and C.F.; modeling, A.F. and I.B.; experiments and validation, A.F.; resources, A.F.; data curation, all equally; writing—original draft preparation, C.F.; writing—review and editing, A.F. and L.B.; supervision, A.F.; project administration, I.B. and A.F.; funding acquisition, A.F. All authors have read and agreed to the published version of the manuscript.

Funding: This research received no external funding.

Institutional Review Board Statement: Not applicable.

Informed Consent Statement: Not applicable.

Data Availability Statement: The data presented in this study are available on request from the corresponding author.

Acknowledgments: The collective would like to thank the technical colleagues who helped to produce the specimens for testing and to the companies that provided the infrastructure and materials for the welding labs (SAM Robotics, SC VOESTALPINE BOHLER WELDING ROMANIA SRL and Linde Romania).

Conflicts of Interest: The authors declare no conflict of interest. The funders had no role in the design of the study; in the collection, analyses, or interpretation of data; in the writing of the manuscript; or in the decision to publish the results.

References

1. Gibson, I.; Rosen, D.; Stucker, B. *Additive Manufacturing Technologies. 3D Printing, Rapid Prototyping, and Direct Digital Manufacturing*, 2nd ed.; Springer: Berlin/Heidelberg, Germany, 2015; ISBN 978-1-4939-2113-3.
2. *ISO/ASTM 52900*; Standard Terminology for Additive Manufacturing–General Principles–Terminology. International Organization for Standardization (ISO): Geneva, Switzerland, 2015.
3. Spalek, N.; Brunow, J.; Braun, M.; Rutner, M. WAAM-Fabricated Laminated Metal Composites. *Metals* **2021**, *11*, 1948. [CrossRef]
4. Available online: https://ultimaker.com/learn/how-to-design-for-fff-3d-printing (accessed on 5 September 2022).
5. Gafe, C.A.; Gangula, B.; Illinda, P. A Deloitte Series on Additive Manufacturing. 2014. Available online: https://www2.deloitte.com/xe/en/insights/focus/3d-opportunity/additive-manufacturing-3d-opportunity-in-automotive.html (accessed on 5 September 2022).
6. Vafadar, A.; Guzzomi, F.; Rassau, A.; Hayward, K. Advances in Metal Additive Manufacturing: A Review of Common Processes, Industrial Applications, and Current Challenges. *Appl. Sci.* **2021**, *11*, 1213. [CrossRef]

7. Safia, A.; Rima, D.; Nouredine, F. Effect of the Laser Scan Rate on the Microstructure, Magnetic Properties, and Microhardness of Selective Laser-Melted FeSiB. *J. Supercond. Nov. Magn.* **2018**, *31*, 3565–3567.
8. Available online: https://mx3d.com/ (accessed on 7 September 2022).
9. BASF. *Ultrafuse 316L: User Guidelines for 3D Printing Metal Parts*; BASF: Limburgerhof, Germany, 2021.
10. Available online: https://ro.disoncasting.com/precision-investment-casting/auto-part-casting/auto-flange.html (accessed on 5 September 2022).
11. Shen, Y.; Li, Y.; Chen, C.; Tsai, H.L. 3D printing of large, complex metallic glass structures. *Mater. Des.* **2017**, *117*, 213–222. [CrossRef]
12. Available online: https://www.dezeen.com/2021/07/19/mx3d-3d-printed-bridge-stainless-steel-amsterdam/ (accessed on 5 September 2022).
13. Suzuki, K.; Hujimori, H.; Hashimoto, K. *Amorphous Metals*; Masumoto, T., Ed.; Metallurgy: Moscow, Russia, 1987; p. 328. (In Japanese)
14. Liang, S.; Wang, X.; Zhang, W.; Liu, Y.; Wang, W.; Zhang, L. Selective laser melting manufactured porous Fe-based metallic glass matrix composite with remarkable catalytic activity and reusability. *Appl. Mater. Today* **2020**, *19*, 100543. [CrossRef]
15. Available online: https://www.twi-global.com/technical-knowledge/job-knowledge/arc-based-additive-manufacturing-137 (accessed on 15 September 2022).
16. Polley, C.; Distler, T.; Detsch, R.; Lund, H.; Springer, A.; Boccaccini, A.R.; Seitz, H. 3D Printing of Piezoelectric Barium Titanate-Hydroxyapatite Scaffolds with Interconnected Porosity for Bone Tissue Engineering. *Materials* **2020**, *13*, 1773. [CrossRef]
17. Jafari, D.; Vaneker, T.H.J.; Gibson, I. Wire and arc additive manufacturing: Opportunities and challenges to control the quality and accuracy of manufactured parts. *Mater. Des.* **2021**, *202*, 109471. [CrossRef]
18. Nam, Y.G.; Koo, B.; Chang, M.S.; Yan, S.; Yu, J.; Park, Y.H.; Jeong, J.W. Selective laser melting vitrification of amorphous soft magnetic alloys with help of double-scanning-induced compositional homogeneity. *Mater. Lett.* **2020**, *261*, 127068. [CrossRef]
19. Treutler, K.; Wesling, V. The Current State of Research of Wire Arc Additive Manufacturing (WAAM): A Review. *Appl. Sci.* **2021**, *11*, 8619. [CrossRef]
20. Lindroos, T.; Riipinen, T.; Metsä-Kortelainen, S.; Pippuri-Mäkeläinen, J.; Lagerbom, J.; Revuelta, A.; Metsäjoki, J. Soft magnetic alloys for selective laser melting. In Proceedings of the EuroPM 2017 Congress and Exhibition, Milan, Italy, 1–5 October 2017.
21. Ouyang, D.; Zhang, P.; Zhang, C.; Liu, L. Understanding of crystallization behaviors in laser 3D printing of bulk metallic glasses. *Appl. Mater. Today* **2021**, *23*, 100988. [CrossRef]
22. Zrodowski, Ł.; Wysocki, B.; Wróblewski, R.; Kurzydłowski, K.J.; Świeszkowski, W. The novel scanning strategy for fabrication metallic glasses by selective laser melting. In Proceedings of the Fraunhofer Direct Digital Manufacturing Conference 2016, Berlin, Germany, 16–17 March 2016.
23. Zou, Y.; Wu, Y.; Li, K.; Tan, C.; Qiu, Z.; Zeng, D. Selective laser melting of crack-free Fe-based bulk metallic glass via chessboard scanning strategy. *Mater. Lett.* **2020**, *272*, 127824. [CrossRef]
24. Available online: https://thermalprocessing.com/advantages-of-wire-arc-additive-manufacturing/ (accessed on 5 September 2022).
25. Kabir, S.F.; Mathur, K.; Seyam, A.F.M. *Seyam: A Critical Review on 3D Printed Continuous Fiber-Reinforced Composites: History, Mechanism, Materials, and Properties, Composite Structures*; Elsevier: Amsterdam, The Netherlands, 2019.
26. Ouyang, D.; Wei, X.; Li, N.; Li, Y.; Liu, L. Structural evolutions in 3D-printed Fe-based metallic glass fabricated by selective laser melting. *Addit. Manuf.* **2018**, *23*, 246–252. [CrossRef]
27. Ozden, M.; Morley, N. Laser Additive Manufacturing of Fe-Based Magnetic Amorphous Alloys. *Magnetochemistry* **2021**, *7*, 20. [CrossRef]
28. Maciąg, F.; Moskalewicz, T.; Kowalski, K.; Łukaszczyk, A.; Hadzhieva, Z.; Boccaccini, A.R. The Effect of Electrophoretic Deposition Parameters on the Microstructure and Adhesion of Zein Coatings to Titanium Substrates. *Materials* **2021**, *14*, 312. [CrossRef]
29. Jiang, Q.; Zhang, P.; Tan, J.; Yu, Z.; Tian, Y.; Ma, S.; Wu, D. Influence of the microstructure on mechanical properties of SLM additive manufacturing Fe-based bulk metallic glasses. *J. Alloys Compd.* **2021**, *894*, 162525. [CrossRef]
30. Bordeenithikasem, P.; Hofmann, D.; Firdosy, S.; Ury, N.; Vogli, E.; East, D. Controlling microstructure of FeCrMoBC amorphous metal matrix composites via laser directed energy deposition. *J. Alloys Compd.* **2020**, *857*, 157537. [CrossRef]
31. *TS 14-123-149-2009*; Rapidly Hardened Tape of Soft–Magnetic Amorphous Alloys and Soft–Magnetic Composite Material (Nanocrystalline Alloy). Asha, Russia. 2011.
32. Li, Y.; Su, C.; Zhu, J. Comprehensive review of wire arc additive manufacturing: Hardware system, physical process, monitoring, property characterization, applicationd and future prospects. *Results Eng.* **2022**, *13*, 100330. [CrossRef]
33. Jung, H.Y.; Choi, S.J.; Konda, G.P.; Mihai, S.; Sergio, S.; Seonghoon, Y.; Uta, K.; Kim, D.H.; Kim, K.B.; Eckertaf, J. Fabrication of Fe-based bulk metallic glass by selective laser melting: A parameter study. *Mater. Des.* **2015**, *86*, 703–708. [CrossRef]
34. Zrodowski, Ł.; Wysocki, B.; Wróblewski, R.; Krawczynska, A.; Adamczyk-Cieslak, B.; Zdunek, J.; Błyskun, P.; Ferenc, J.; Leonowicz, M.; Świeszkowski, W. New approach to amorphization of alloys with low glass forming ability via selective laser melting. *J. Alloys Compd.* **2019**, *771*, 769–776. [CrossRef]
35. Golod, V.M.; Sufiiarov, V.S. The evolution of structural and chemical heterogeneity during rapid solidification at gas atomization. *IOP Conf. Ser. Mater. Sci. Eng.* **2017**, *192*, 012009. [CrossRef]

36. Gao, S.; Yan, X.; Chang, C.; Aubry, E.; He, P.; Liu, M.; Liao, H.; Fenineche, N. Microstructure and magnetic properties of FeSiBCrC soft magnetic alloy manufactured by selective laser melting. *Mater. Lett.* **2021**, *290*, 129469. [CrossRef]
37. Salunkhe, S.; Amancio-Filho, S.T.; Davim, J.P.J. *Advances in Metal Additive Manufacturing*; Elsevier: Amsterdam, The Netherlands, 2022.
38. Available online: https://www.esab.co.uk/gb/en/products/filler-metals/mig-mag-wires-gmaw/mild-steel-wires/weld-g3si1.cfm (accessed on 12 September 2022).
39. Chandrasekaran, S.; Hari, S.; Amirthalingam, M. Wire arc additive manufacturing of functionally graded material for marinerisers. *Mater. Sci. Eng. A* **2020**, *792*, 139530. [CrossRef]
40. Załuska, A.; Matyja, H. Crystallization characteristics of amorphous Fe-Si-B alloys. *J. Mater. Sci.* **1983**, *18*, 2163–2172. [CrossRef]
41. Li, Y.; Shen, Y.; Chen, C.; Leu, M.; Tsai, H.L. Building metallic glass structures on crystalline metal substrates by laser-foil-printing additive manufacturing. *J. Mater. Process. Technol.* **2017**, *248*, 249–261. [CrossRef]
42. Von Mises, L. *Human Action*; Ludwig von Mises Institute: Auburn, AL, USA, 2010; pp. 200–230.
43. Buta, I.; Pavăl, C. Realizarea unei Flanșe de Legătură între un Universal de Strung și o Masă Rotativă Folosind Procedeul WAAM (Wire Arc Aditive Manufacturing). Master's Thesis, Department of Materials and Manufacturing Engineering, Mechanical Faculty, Polytechnic University Timisoara, Timișoara, Romania, 2022.

böhler welding
by voestalpine
3Dprint

Lasting Connections

THE FUTURE OF PRODUCTIVITY: WIRE ARC ADDITIVE MANUFACTURING

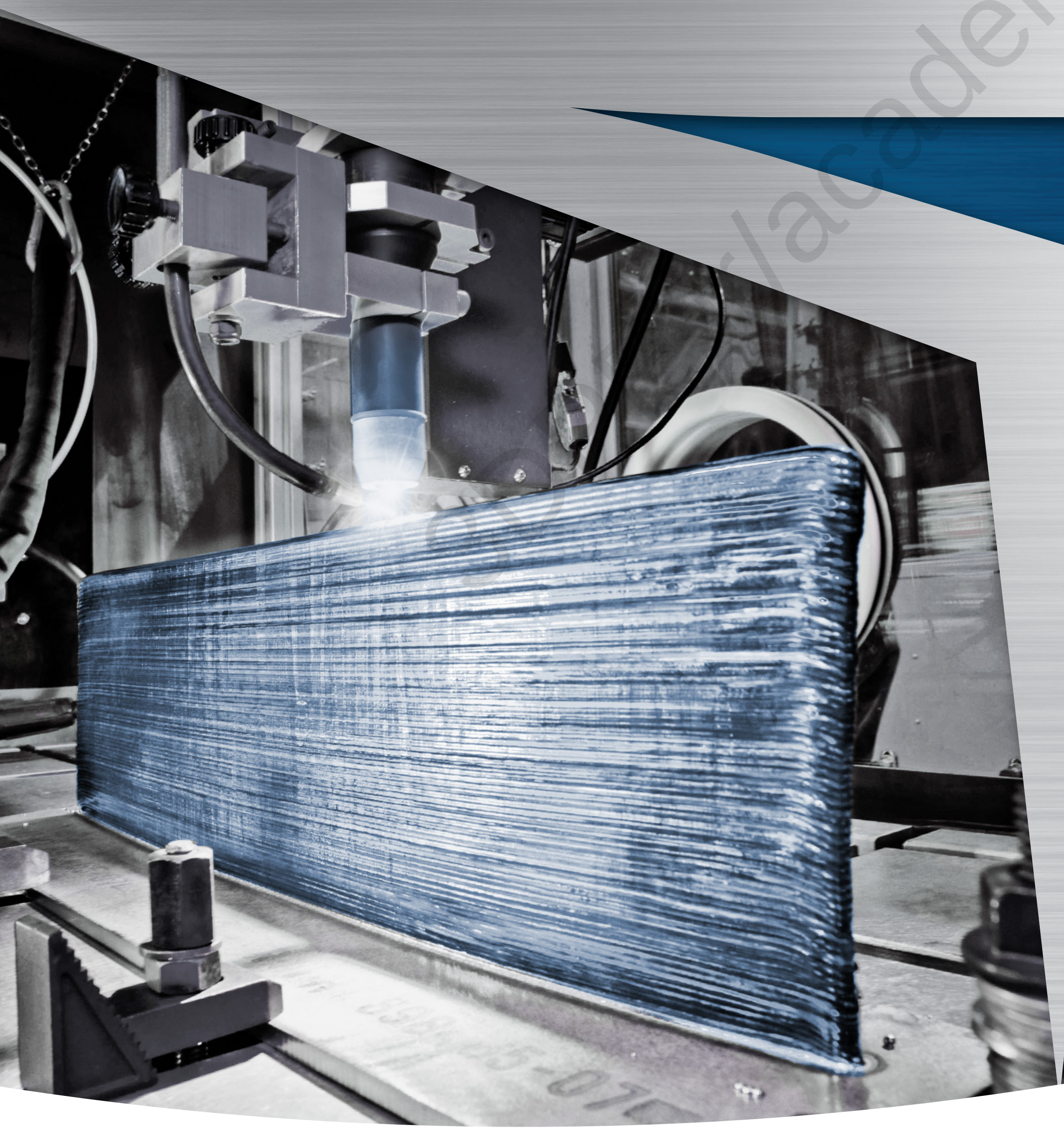

voestalpine Böhler Welding
www.voestalpine.com/welding

voestalpine
ONE STEP AHEAD.

THE FUTURE OF PRODUCTIVITY: WIRE ARC ADDITIVE MANUFACTURING

3D PRINTING WITH THE BEST-IN-CLASS WIRE ALLOYS

Additive manufacturing – popularly known as 3D printing – is one of the most revolutionary new manufacturing methods of our time.

Wire Arc Additive Manufacturing is a new disruptive technology that is being enthusiastically adopted at voestalpine Böhler Welding for its leading brand Böhler Welding.

It not only allows almost lossless processing of high-value material but also results in high-strength components with a flexibility that would not be conceivable using conventional methods. Up to now, manufacturing methods such as casting/milling and forging have been used for production of large components.

Material is removed from a casting or blank and creates scrap. The specialists at Böhler Welding are researching special materials for the optimized production of highest quality solid and seamless cored wires with excellent surface finishing and properties required for a stable 3D printing processes.

Contact us personally and experience a new dimension in manufacturing.

Dr. Martin Peruzzi
CTO, voestalpine Böhler Welding

PIONEERING EXPERTISE

As a pioneer in innovative welding consumables, Böhler Welding offers a unique product portfolio for joint welding worldwide. More than 2000 products are adapted continuously to the current industry specifications and customer requirements, certified by well-respected institutes and thus approved for the most demanding welding applications. As a reliable partner for customers, “lasting connections” are the brand’s philosophy in terms of both welding and people.

As long ago as 1927 Böhler Welding developed the “Seelendraht” (“soul wire”) the predecessor of the modern-day flux cored wire. The company has been leading ever since, as current innovations, like the laser-sealed flux cored wires or the leadership in Wire Arc Additive Manufacturing, proves. Customers can rely on a outstanding product portfolio for all demanding welding tasks.

A revolutionary technology shapes the future of our life

Wire Arc Additive Manufacturing enables fast and highly efficient production processes replacing conventional technologies as casting and forging. The machining effort like milling and drilling is reduced to a minimum due to a near-net-shape using Wire Arc Additive Manufacturing. Lead times can be reduced dramatically by high utilization of the wire consumables and by simplification of the production process in general.

Especially as the Wire Arc Additive Manufacturing is based on the well-known technology of joining and cladding materials with a wide range of commercialy available wire consumables from unalloyed, mid- and high alloyed steels. But also nickel- and cobalt base alloys can be used and combined, if metallurgical reasonable, to gradient structured parts.

Given the typical layer thickness applied, Wire Arc Additive Manufacturing is – compared to powder-based Additive Manufacturing – more suitable to generate low to medium complexity and up to large scale preform components.

Due to a wide range of parameter settings it is possible to reach high deposition rates with rates up to 5 kg/h, so that the production of large scale parts is feasible within reasonable time frames. Depending on the material alloy group, heat treatments and post-machining is usually required to give the components the final properties.

Key Benefits for Wire Arc Additive Manufacturing

- Wide range of deposition rates (low to high)
- Near-Net shape and therefore reduced material loss
- Conventional machining time reduced to minimum
- Reduced lead times
- Good structural integrity
- Low to medium complexity components

For Demanding Industries, e.g.

- Mechanical Engineering & Machinery
- Oil & Gas Upstream and Offshore
- Chemical Industry
- Power generation
- Aerospace

BEST QUALITY WIRE ALLOYS FOR A REVOLUTIONARY TECHNOLOGY

With the manufacturing of wires which are tailor-made to its specific purpose, voestalpine Böhler Welding is creating the basis for innovative Wire Arc Additive Manufacturing. The metallurgical and application know-how of its materials specialists makes the company a central element in this technological revolution.

Wire alloys are the material basis for the revolutionary game-changing process. They may be made from low- and medium alloyed steel, aluminum, nickel, or titanium alloys. The wire alloys used determine the properties of the final printed component. Their production is therefore the focus of increasing attention – especially that of the materials and process specialists at voestalpine Böhler Welding. For example, application of wire alloys in Wire Arc Additive Manufacturing requires constant chemical composition within well-defined tolerances and excellent surfaces enabling good feeding properties.

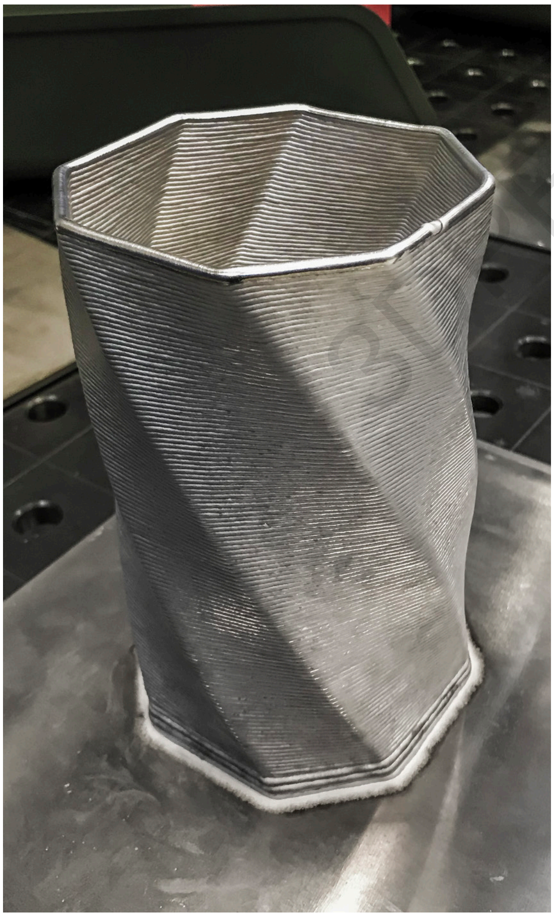

Quality manufactured in Europe

With its production facilities for solid wire in Hamm, Germany, and for seamless cored wires in Kapfenberg, Austria, and Cittadella, Italy the company is equipped with the latest state-of-the-art and future manufacturing technologies for the production of wire alloys for additive manufacturing. Well-equipped laboratories allow in-house analysis and characterization of new developed products and ensure the best in class quality.

Cooperation for material and technology research

Together with its industrial and scientific partners, voestalpine Böhler Welding has initiated R&D programs to explore the application behavior of wire consumables in Wire Arc Additive Manufacturing. Results will allow to further optimize the wire consumables and to develop alloy compositions for the next generation 3D printing applications.

PRODUCT PORTFOLIO

Product Name	C	Si	Mn	Cr	Mo	Ni	$R_{p0.2}$	R_m	A_5	
3Dprint AM 35	0.1	0.3	1.05	–	–	–	> 355 MPa	470-630 MPa	> 22 %	Low alloyed steel
3Dprint AM 46	0.1	1	1.7	–	–	–	> 460 MPa	560-720 MPa	> 22 %	Low alloyed steel
3Dprint AM 50	0.1	0.65	1.4	–	–	1.35	> 500 MPa	560-720 MPa	> 18 %	Low alloyed steel
3Dprint AM 62	0.1	0.65	1.6	–	0.4	1.1	> 620 MPa	700-890 MPa	> 18 %	Medium alloyed steel
3Dprint AM 70	0.08	0.6	1.7	0.2	0.5	1.5	> 690 MPa	770-940 MPa	> 17 %	Medium alloyed steel
3Dprint AM 80 HD	0.09	0.4	1.7	0.35	0.6	2	820 MPa	920 MPa	20 %	Medium alloyed steel (typical mech. Properties after post heat treatment)
3Dprint AM P22	0.08	0.5	1	2.5	1	–	> 310 MPa	515-690 MPa	> 18 %	Medium alloyed steel (mech. Properties after post heat treatment)

Chemical composition in wt.-%

Product Name	C	Si	Mn	Cr	Mo	Ni	N	
3Dprint AM 2209	0.025	0.5	1.6	23	3	9	0.14	Duplex steel (no heat treatment)
3Dprint AM 2205	0.025	0.5	1.5	22	3	5	0.15	Duplex steel (with solution annealing heat treatment)

Chemical composition in wt.-%

Product Name	C	Si	Mn	Cr	Mo	Ni	Cu	Nb	
3Dprint AM 304L	0.02	0.5	1.7	20	–	10	–	–	Standard low carbon austenitic stainless steel
3Dprint AM 316L	0.02	0.5	1.7	18.5	2.6	12.3	–	–	Standard low carbon austenitic stainless steel with Molybdenum
3Dprint AM 17-4 PH	0.02	0.4	0.5	16.5	–	4.5	3.3	0.25	Martensitic precipitation-hardening stainless steel
3Dprint AM 15-5 PH	0.02	0.5	0.5	14.8	–	4.5	3.3	0.28	Martensitic precipitation-hardening stainless steel – free of ferrite (aerospace grade)
3Dprint AM 410 NiMo	0.01	0.65	0.7	13	0.5	4.7	–	–	Martensitic stainless steel
3Dprint AM 430	0.07	0.8	0.7	18	–	–	–	–	Ferritic stainless steel

Chemical composition in wt.-%

Product Name	C	Si	Cr	Mo	Nb	Fe	Ni	W	Al	Ti	
3Dprint AM 625	< 0.03	< 0.25	22	9	3.6	0.5	bal.	–	–	–	Nickel base alloy with chromium, molybdenum and niobium
3Dprint AM 718	0.03	< 0.1	17.5	3	5	bal.	53	–	0.5	1	Precipitation hardening nickel base alloy

Chemical composition in wt.-%

Product Name	Mg	Ni	Fe	C	N	O	H	V	Zr	Mn	Al	Cu	Ti	
3Dprint AM Al 2219	< 0.02	–	–	–	–	–	–	–	0.18	0.35	bal.	6.3	0.14	Aluminium alloy
3Dprint AM Cu 6328	–	4.5	3.5	–	–	–	–	–	–	1	9	bal.	–	Copper-Aluminium alloy
3Dprint AM Ti-5	–	–	< 0.15	< 0.05	< 0.03	0.18	< 0.01	4	–	–	6	–	bal.	High strenght titanium alloy

Chemical composition in wt.-%

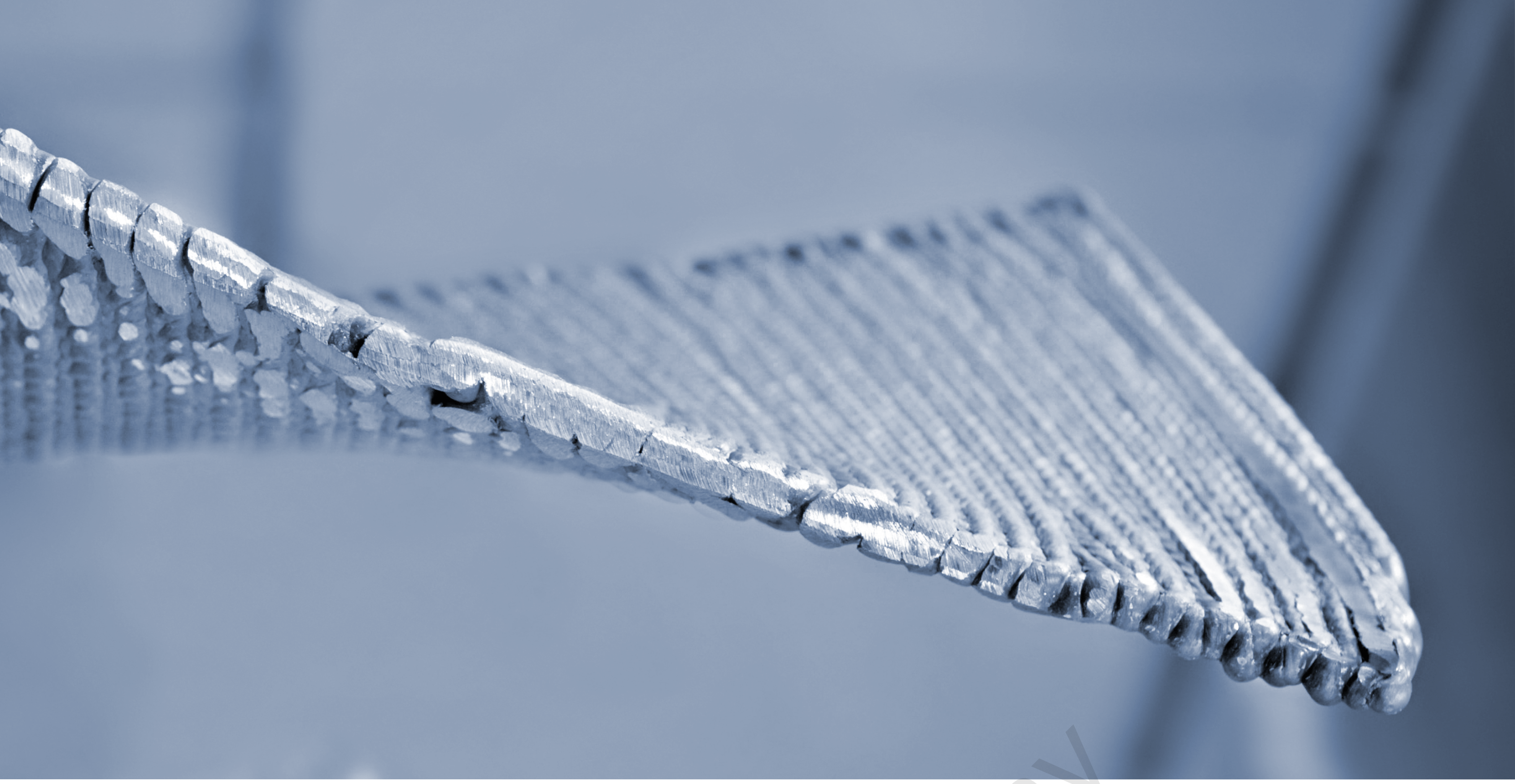

WHAT MAKES BÖHLER WELDING 3DPRINT WIRES DIFFERENT?

Wires are specifically designed and manufactured for wire arc additive manufacturing, meaning that every production step is fine tuned to bring wire feedability and arc stability at its best:

» Drawing process is more accurate providing the best surface finishing.

» Feedability is enhanced also thanks to specific coating.

» Wires wounding of spools and drums is controlled within restricted tolerances.

» Endurance testing protocols with the related acceptance criteria have been settled in order to prove a high level of arc stability and feedability measuring in real-time all the electrical parameters involved and the wire resistance at the wire feeder.

3Dprint wires chemical analysis is fine-tuned for Wire Arc Additive Manufacturing

About metallurgical aspects, productivity leads to the use of high heat input and low cooling rate due to the subsequent layers deposition technique, hence physical and mechanical properties of the deposit has to be soundness also in such conditions; additionally it has to be tolerant to take multiple hardening/tempering cycles by multiple layers and afford heat treatment when and if necessary.

Wire chemistry is also influencing the arc stability, the molten material fluidity as well as the silicate islands formation over the bead, which might be detrimental for the deposition of the subsequent layer. Level of impurities and Silicon is of course very important to keep this issue under control.

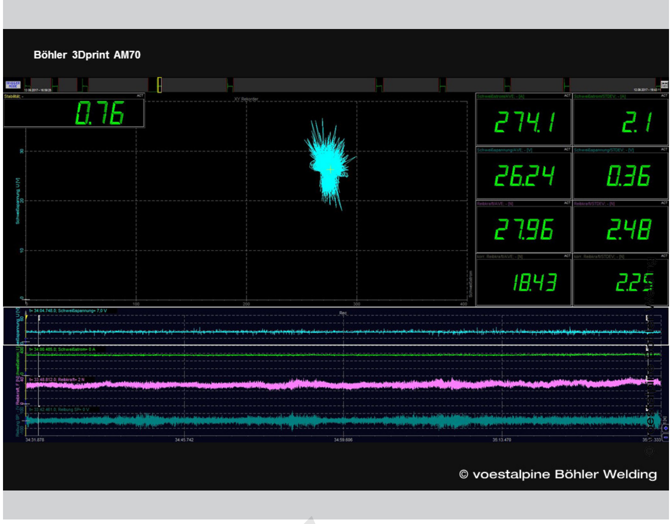

U[V]/I[A] integral plot over time (blue star in the middle) of stable process which shows only minor deviations

Summarized benefits of Böhler Welding 3Dprint wires

Metallurgical benefits	Process benefits	
» Made for low cooling rates and high heat input	» High process stability for Robotic MIG or other mechanised processes	
» Accepts multiple hardening/tempering cycles by multiple layers	» Drum and spool weights can widely be adopted to the weight of parts	
» Optimised for post print heat treatment	» Extended quality control to ensure consistent arc and feeding behavior	
» Tailor-made metallurgy for complex materials	» Optimised surface technology for long arc cycles, Liners stay clean, contact tips last longer	

EXCELLENT PROPERTIES OF THE PRINTED METAL

A fine-tuned printing process together with the described benefits lead structures made with Böhler Welding 3Dprint wires to meet demanding industries requirements.

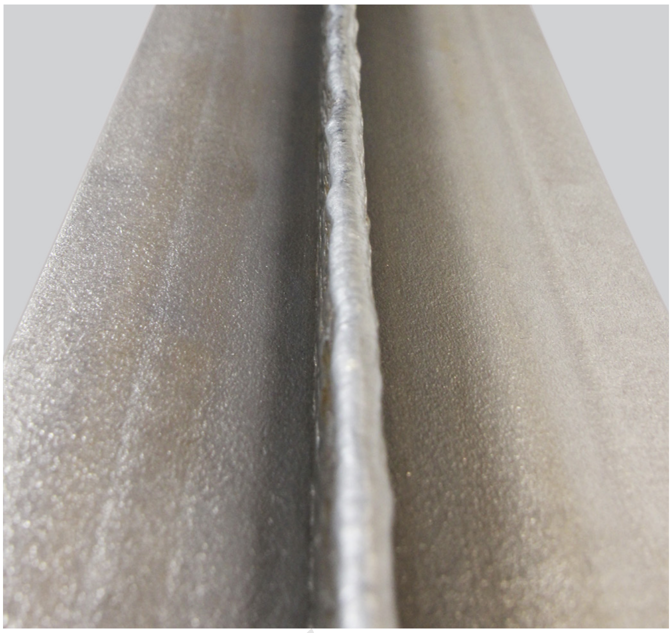

Wall made with wire 3Dprint AM 80HD for properties characterization

PRINTED METAL CHARACTERIZATION

As far as materials properties are concerned, voestalpine Böhler Welding is deeply involved in testing wires in wire arc additive manufacturing conditions, remarking analogies and differences with the conventional technologies as well as the welding conditions.

Material Integrity

In this regard, microporosity assessment demonstrates that wire arc additive manufacturing using 3Dprint wires can provide an integrity level often comparable to forging and better than casting.

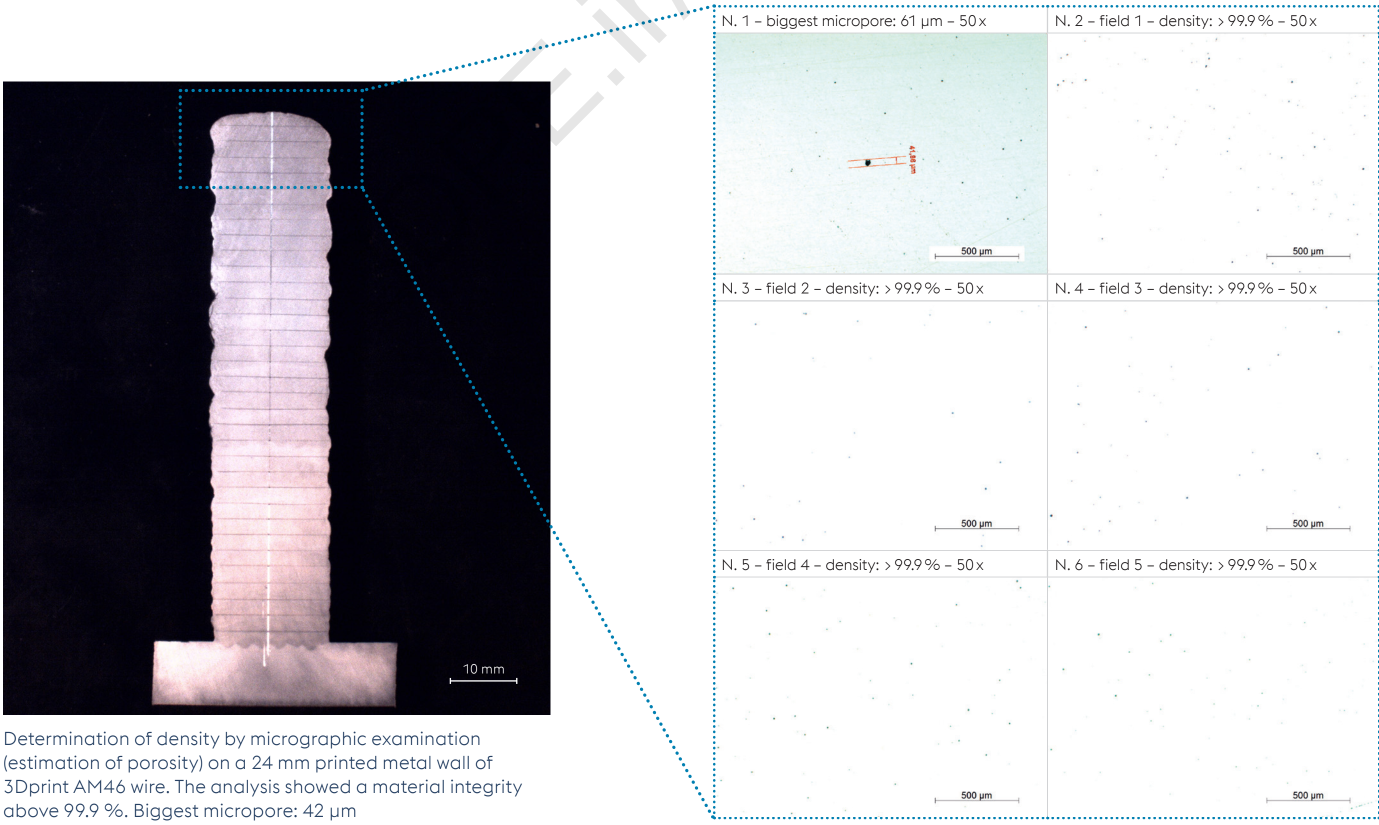

Determination of density by micrographic examination (estimation of porosity) on a 24 mm printed metal wall of 3Dprint AM46 wire. The analysis showed a material integrity above 99.9 %. Biggest micropore: 42 µm

Testing of printed metal in Wire Arc Additive Manufacturing Conditions

voestalpine Böhler Welding is investigating specific geometry walls and blocks to reproduce the typical cooling rates of Wire Arc Additive Manufacturing, extracting specimen for tensile, impact energy, bending and any other relevant test depending upon the specific alloy.

Printed coupon and destructive tests on precipitation hardening martensitic stainless steel 3Dprint AM 17-4 PH deposit

PRINTING OF CHALLENGING MATERIALS

Böhler 3Dprint product portfolio includes a wide range of high technology sofisticated alloys. An adequate knowledge of these materials behavior when printing is a precondition to achieve high level results.

voestalpine Böhler Welding makes available wire arc additive manufacturing esperts and application engineers to support customers whenever it is needed.

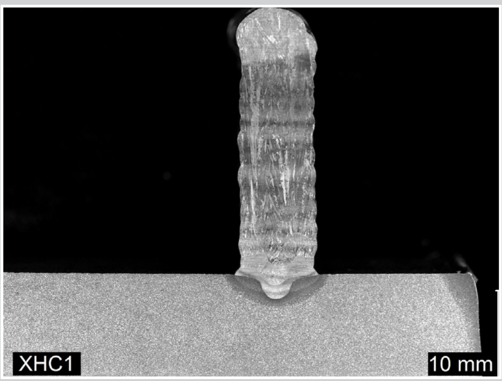

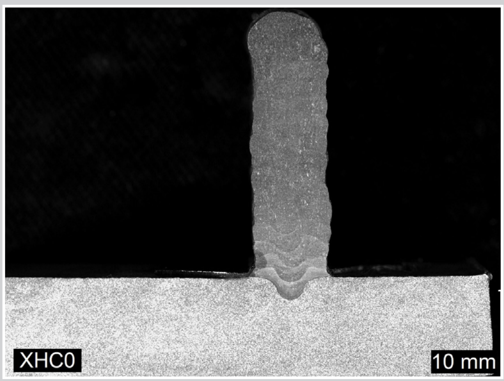

Macro of precipitation hardening martensitic stainless steel 3Dprint AM 17-4 PH deposit as printed and after heat treatment

JOIN! voestalpine Böhler Welding

With over 100 years of experience, voestalpine Böhler Welding is the global top address for the daily challenges in the areas of joint welding, repair, hardfacing and cladding as well as brazing. Customer proximity is guaranteed by more than 40 subsidiaries in 25 countries, with the support of 2,200 employees, and through more than 1,000 distribution partners worldwide. With individual consultation by our application technicians and welding engineers, we make sure that our customers master the most demanding welding challenges. voestalpine Böhler Welding offers three specialized and dedicated brands to cater our customers' and partners' requirements.

böhler welding by voestalpine

Lasting Connections – As a pioneer in innovative welding consumables, Böhler Welding offers a unique product portfolio for joint welding worldwide. More than 2000 products are adapted continuously to the current industry specifications and customer requirements, certified by well-respected institutes and thus approved for the most demanding welding applications. As a reliable partner for customers, "lasting connections" are the brand's philosophy in terms of both welding and people.

utp maintenance by voestalpine

Tailor-Made Protectivity™ – UTP Maintenance ensures an optimum combination of protection and productivity with innovative and tailor-made solutions. Everything revolves around the customer and their individual requirements. That is expressed in the central performance promise: Tailor-Made Protectivity™.

fontargen brazing by voestalpine

In-Depth Know-How – As a leading brand of soldering and brazing consumables, Fontargen Brazing offers proven solutions based on 50 years of industrial experience, tried and tested processes and methods. This In-Depth Know-How has made Fontargen Brazing an internationally preferred partner for every soldering and brazing task.

The Management System of voestalpine Böhler Welding Group GmbH, Peter-Mueller-Strasse 14-14a, 40469 Duesseldorf, Germany has been approved by Lloyd's Register Quality Assurance to: ISO 9001:2015, ISO 14001:2015, OHSAS 18001:2007, applicable to: Development, Manufacturing and Supply of Welding and Brazing Consumables.
More information: www.voestalpine.com/welding

LLOYD'S REGISTER · LRQA
ISO 9001 · ISO 14001
OHSAS 18001
UKAS MANAGEMENT SYSTEMS
001

087/2019/EN/GL

Coalesce Research Group

International Journal of 3D Printing and Additive Manufacturing

Research Article

2022: Volume 1, Issue 1

Metallurgical Characteristics of Low Carbon Steel Cylindrical Components Made by Wire Arc Additive Manufacturing (WAAM) Technique

Bellamkonda Prasanna Nagasai*, Sudersanan Malarvizhi and Visvalingam Balasubramanian

Department of Manufacturing Engineering, Annamalai University, India.

Received Date: 16-07-2022 **Published Date:** 20-08-2022

Abstract

Fabrication of metal parts by wire and Arc Additive Manufacturing (WAAM) has received an increased interest in recent years, as it allows high design flexibility and reduction of material wastage compared to other traditional manufacturing routes. This article compares the effect of heat input on metallurgical characteristics of wire arc additive manufactured low carbon steel cylindrical components fabricated by Gas Metal Arc Welding (GMAW) and Cold Metal Transferred Arc Welding (CMTAW) processes. Firstly, the influence of heat input on the grain size was analyzed. Subsequently, the effect of heat input on the metallurgical characteristics of the cylindrical components was studied along the building direction. The microstructure of the built cylindrical-walled component varies from the top to the bottom regions and can be distinguished into two regions: lamellar structures (widmanstatten ferrite and grain boundary ferrite) in the top regions; and equated grains of fully ferrite in the bottom region in GMAW. In the CMT-WAAM cylindrical component samples have been noted two different regions: the bottom region characterized by a ferritic structure with thin strips of pearlite and the top region characterized by a lamellar structure typically bainite with acicular ferrite.

Keywords: Wire arc additive manufacturing, gas metal arc welding, cold metal transfer arc welding, low carbon steel and microstructural characteristics.

Introduction

Additive Manufacturing (AM) is relatively a new manufacturing technique that has created a lot of attention in the past decade. The ability to create structurally complicated components with unparalleled design flexibility has undergone a change. Every AM technique has a unique combination of heat source, feedstock, and movement mechanism, making it suitable for a wide range of applications [1]. AM methods for metal components have been categorized into four categories by ASTM (ASTM F2792), one of which is Directed Energy Deposition (DED). By definition, DED is "an additive manufacturing process in which concentrated heat energy is utilized to melt materials as they are deposited"[2].

Wire-feed and powder-feed techniques are variations of DED technology. When compared to powder, the ability to use wire as a feedstock results in a lower cost per kg and a higher material utilization rate. As a result, the manufacturing of large components is excellent for wire-feedstock technologies, which are the most effective additive processes for this purpose [3]. Wire arc additive manufacturing (WAAM) is a low-cost and efficient technology for fabricating large and medium-scale components and structures. WAAM uses a common arc-based welding equipment to manufacture large structures and components for multilayer deposition

Corresponding author: Bellamkonda Prasanna Nagasai, Department of Manufacturing Engineering, Annamalai University, India.
E-mail: *nagasaibellamkonda143@gmail.com*

Citation: Bellamkonda PS, Sudersanan M, Visvalingam B. Metallurgical Characteristics of Low Carbon Steel Cylindrical Components Made by Wire Arc Additive Manufacturing (WAAM) Technique. J 3D Print Addit Manuf. 2022;1:1-7.

in a layered technique. Gas metal arc welding (GMAW), gas tungsten arc welding (GTAW), and Plasma arc welding (PAW) techniques can all be used in the WAAM process [4]. Various materials, ranging from titanium, aluminum, steel, and nickel alloys, have proved the feasibility of the WAAM method. The author [5] documented that the Cold Metal Transfer (CMT) process is suitable for large-scale stainless steel components with medium-high mechanical properties; Gas tungsten arc welding (GTAW) process is recommended for small-medium size titanium and stainless steel components with medium-high mechanical requirements; Plasma arc welding (PAW) process is appropriate for medium-large size steel and titanium components with medium-high mechanical characteristics.

CMTAW is a variant of GMAW process. The fundamental CMT method is based on wire movement, which aids in molten droplet detachment. This enables the arc to be extinguished at regular intervals, reducing the process's heat input [6]. The filler wire is pushed into the welding pool formed by the arc in the first phase or arcing period. The arc becomes extinguished and the welding current is reduced when the filler metal reaches the weld pool. The droplet detachment is followed during the short circuit by the rearward motion of the wire. The current is kept low in the short-circuit phase. After that, the cycle starts again when the arc is ignited and the wire is pushed into the weld pool. The current waveforms of GMAW and CMTAW processes. During the deposition, the current is constant in GMAW and the actual value fluctuates between the peak (in peak phase) and the base (in base phase), resulting zero current (in short circuit phase) in CMTAW [7]. In conventional spray transfer and pulsed spray transfers, the cooling rate is very slow compared to the CMTAW short circuit process [8]. Therefore, a low heat input process such as CMTAW can improve significantly the mechanical properties of WAAM carbon-steel components. The possibilities of this CMTAW process have not been studied till now for the WAAM of metal cylindrical components.

In the WAAM, heat input is the key factor affecting the morphology of the components, the microstructure and the mechanical properties. Another difficulty with WAAM in steels is the possible mixture of multiple microstructures (e.g., ferrite, Grain boundary ferrite (GBF), Widmanstätten ferrites (α_w), bainite (B), martensite, and acicular ferrite (α_a)) depending on % carbon, alloy elements, and cooling time [9]. Tiago The author [10] investigated the mechanical properties and microstructural characteristics of high strength low alloy steel manufactured by WAAM. The different microstructural features of ferrite, marten site, bainite and reverted austenite were found at different heat inputs. In reference [11] the author studied the microstructure and mechanical properties of multi directional pipe joints using WAAM and revealed that the microstructure comprised 28.2% pearlite and 71.8% ferrite, while the average size of grain did not surpass 15µm. Similarly, in recent research [12] the author observed anisotropy in mechanical properties and microstructural changes in Al-7Si-0.6 Mg alloy parts. This microstructural changes affectively impacts the mechanical properties of manufactured components. As a result, researchers have focused even more on microstructure evolution, mechanical properties, and fracture behavior in the WAAM process. However, heat input variations arise when different modes of metal transfers are used even if the feed rate for wire is maintained constantly.

In recent studies [13,14] it is reported that the high heat input and thermal histories experienced by the parts during AM technologies affects the direction and shape of grains results anisotropy in mechanical properties as well as changes in microstructures features. But low heat input WAAM-based techniques can lead to uniform microstructure and good mechanical properties [15]. In recent article [16] the authors scientifically investigated the effect on the porosity characteristics of additively manufactured Al-6.3% Cu alloys of different metal transfer modes during a CMT process, and their findings showed that heat input is one of the critical factors for the advanced CMT pulse process (CMT-PADV) to control porosity rates. In recent work [17], the authors observed a uniform microstructure with less heat input, resulting in greater tensile strength than those made in the component by higher heat input. The authors stated that, as compared to the bottom of the part, the top of the part resulted in a coarse-grained microstructure with a decreased tensile strength because of the higher temperature gradient at the top of the wall.

Based on the current literature survey, no systematic studies have been reported on comparing GMAW and CMTAW processes for the manufacturing of low carbon steel cylindrical components have been conducted. The correlation between the heat input used in GMAW and CMTAW and the process impacting the microstructural and mechanical properties of low carbon steel have yet to be documented. Low carbon steel (ER70S-6) is a steel with a low carbon content of from 0.05 to 0.25% and, depending on the weight percentage of its alloying elements and used processes, its microstructure is defined. Carbon steel is widely used in the construction of automobile parts and structures, pipes and food cane industries.

This study provides a deeper understanding of the manufacturing of ER70S-6 low carbon steel cylindrical components by WAAM techniques using GMAW and CMTAW processes. The influence of heat input on microstructures was examined at various regions of the cylindrical components. There has also been an analysis of changes in microstructural characteristics and phases at different regions of the cylindrical components

Experimental Work

Materials and Manufacturing

The cylindrical components were manufactured on a substrate plate of mild steel with dimensions of 250×250×10 mm. As filler material, the solid wire ER70S-6 (AWS A5.18 standard) with 1.2 mm diameter was used. The chemical composition of the filler wire used in this investigation is presented in [**Table 1**]. The welding machine CMT Advanced 4000 R [**Figure 1**] was used as a welding power source during the deposition process and the filler wire was supplied to the welding torch, which was kept stationary using a rotating table for each layer. The welding torch was kept constant perpendicular to the substrate. Meanwhile, the substrate will rotate with the arrangement of a rotating table system. The carbon steel cylindrical parts were built with GMAW and CMTAW using optimized process parameters presented in [**Table 2**]. A pause of 120 sec was imposed between each layer deposition, in order to enable a partial cooling of the deposited material. The cylindrical components were separated into two regions from base plate to 75mm bottom region in [**Figure 2**] and the middle of the component from 75mm to 150 mm top region in [**Figure 2 and 3**] shows the photographs of cylindrical components built via GMAW and CMTAW processes, and their dimensions are presented in [**Table 3**]. The heat input (kJ/mm) was calculated using Eq.

$$HI = \eta \times V \times I \times 60 \,/\, S \times 1000$$

Where S is the travel speed in millimeters per minute, I am the average arc current in amperes, V is the arc voltage in volts and η is the process efficiency in % which is assumed as 0.8.

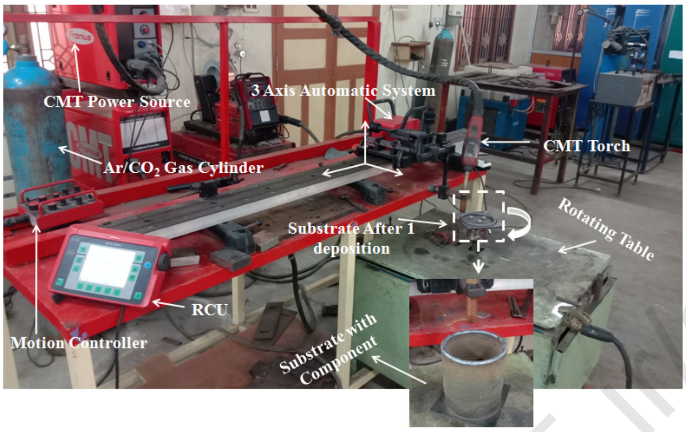

Figure 1: CMTAW-WAAM setup used to manufacture cylindrical components.

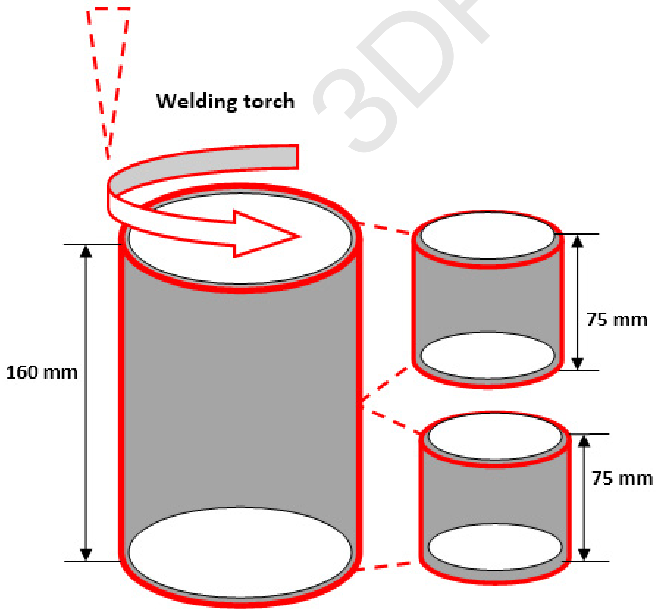

Figure 2: Schematic illustration of the WAAM carbon steel cylinder indicating direction of deposition and showing separation of component in two regions.

Figure 3: Photographs of the low carbon steel straight cylindrical components, a) GMAW process and b) CMTAW process.

Specification	C	Si	Mn	Cr	Mo	Ni	P	S	Fe
ER70S-6	0.12	1.15	1.8	0.15	0.15	0.15	0.025	0.025	Bal

Table 1: Chemical composition (wt. %) of filler metal (all weld metal).

Parameters	GMAW	CMTAW
Wire feed speed (mm/min)	6700	7000
Current (A)	229	200
Voltage (v)	18.3	16
Travel speed (mm/min)	400	400
Arc length correction (%)	----	0
85%Ar+15%CO2 (lit/min)	15	15
Heat Input (kJ/mm)	0.502	0.384

Table 2: Optimized WAAM process parameters used to fabricate the components

Geometry	GMAW	CMTAW
Average wall thickness (mm)	7.8±2	7.3±2
Average single layer height (mm)	2.2	2.55
Diameter of the cylinder (mm)	122±5	120±7
Total cylindrical component height (mm)	160	160

Table 3: Dimensions of manufactured cylindrical components.

Macrostructure and Microstructure Analysis

The surface of metallographic samples was polished with different grades of emery papers and applied diamond paste for mirror finishing. For revealing bright microstructure from the center portions of bottom and top regions of components, 2% Nital reagent was used as an etchant. The macrostructures of the bottom and top regions of the GMAW and CMTAW cylindrical components were examined with a stereo zoom microscope. The microstructure of the bottom and top regions of the cylindrical components was examined with a light optical microscope. Image software was used to measure the grain size of cylindrical components and chemical elements were confirmed by Optical Emission Spectrometer. The obtained microstructural features and grain size were correlated to the heat input and subsequently to the mechanical properties of WAAM cylindrical components.

Results and Discussion

Macrostructure

[**Figure 4a-4d**] shows the macrostructures of the bottom and top regions of the GMAW component in **Figure 4a, b** and the CMTAW component in **Figure 4c, d.** The weld layers are clearly visible in the macrostructures, and the deposited beads are properly fused. The weld is free from flaws or other noticeable defects, as evidenced by the macrostructure.

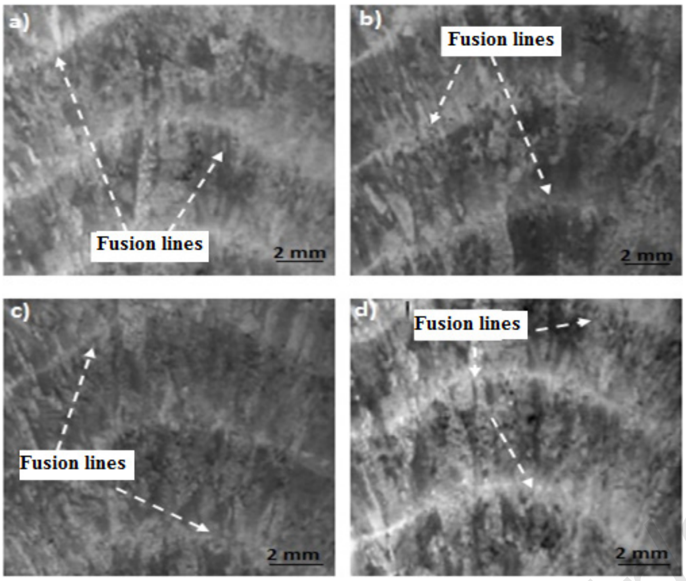

Figure 4: Macrostructures of bottom and top regions of the cylindrical components, a) and b) GMAW and c) and d) CMTAW.

Microstructure Analysis

[**Figure 5a**] shows the low magnification micrograph of the ER70S-6 carbon steel revealing ferrite and pearlite at grain boundaries. The manufactured WAAM based GMAW and CMTAW carbon steel components almost revealed similar microstructure [**Figure 5b and c**]. However, the welding processes have an effect on the grain size of the manufactured components, particularly in the bottom region. The component manufactured by the GMAW process revealed larger grains (16.23 ± 0.71µm). In fact, high current and voltage used in the GMAW process led to an increase in the heat input. The solidification time and the cooling time increase with higher heat input. This increases the size of the grains. The fine grains (12.04 ± 0.43 µm) were formed in the cylindrical wall component manufactured by the CMTAW process shown in [**Figure 5c**]. The solidification time and cooling time decrease with low heat input. This decreases the size of the grains. In recent article [18] the authors also observed similar behavior in the middle and bottom regions of the ER70S-6 low carbon steel thin wall parts. The authors reported that the thin wall part of sample 4 revealed coarse grains due to high input at high current value and sample 1 revealed fine grain due to low heat input at low current value.

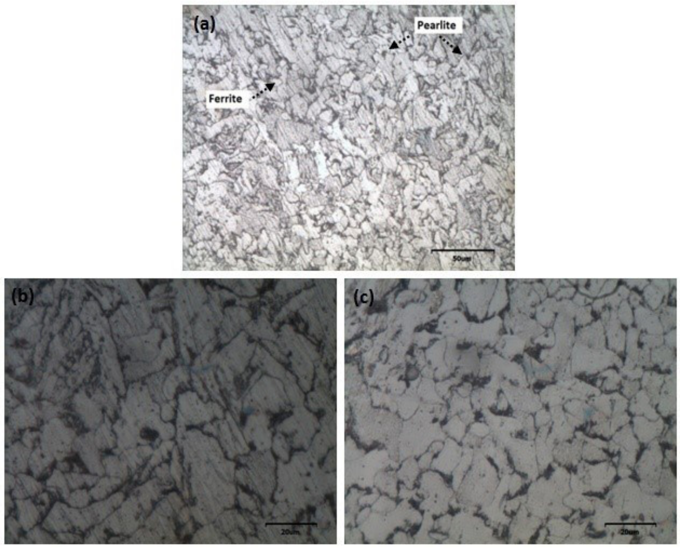

Figure 5: Optical photographs, a) primary microstructure of ER70S-6, b) average grain size of GMAW component= 16.23±0.71µm and c) average grain size of CMTAW component = 12.04±0.43 µm.

The microstructure of the GMAW component varied from the bottom to the top region shown in [**Figure 6**]. **Figure 6b** shows the bottom region of the GMAW component microstructure composed of a fully ferritin structure, indicated by the green color. The top region of the microstructure was composed of PF, GBF, α_w and α_a as shown in [**Figure 6c and d**]. In another investigation [19] the authors also documented similar results in low carbon steel walls. The author observed that the widmanstatten ferrite, acicular ferrite and allotriomorphic ferrite in upper region and equated ferrite in the bottom region. The differences in microstructure from lower to upper zone due to the effect of air cooling and heat transfer from the upper to lower zone of the wall.

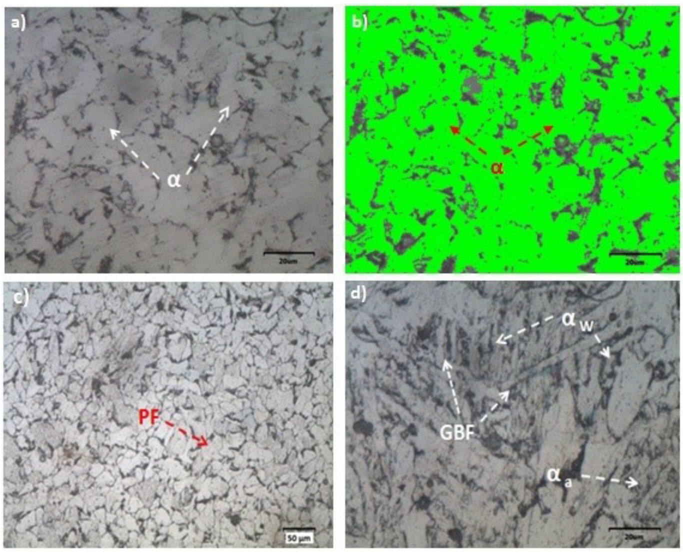

Figure 6: Optical photographs of GMAW cylindrical component a) and b) bottom region, c) top region at lower magnification and d) top region at higher magnification.

[**Figure 7b**] shows the microstructure of the bottom region of the CMTAW cylindrical component composed of a ferrite and small strips of pearlite (indicated by the red color). The top region mainly consists of α_a and B as shown in [**Figure 7c**] at low magnification. [**Figure 7d**] at higher magnification, revealing the formation of B (laths formed in the grain) and α_a due to the fast cooling of the CMTAW process. The aforementioned heterogeneous in the microstructure during WAAM of low carbon AH36 steel filler wire is also documented in reference [20]. The author observed α_a and B near the fusion line. The presence of α_a and B in the microstructure of steel can improve the mechanical characteristics of the component [21,22]. This is mainly due to the finer structure of the two phases and a more even distribution of carbide and greater dislocation density, as well as the internal stresses during the B phase, which help to increase hardness/strength and alloy ductility [23,24].

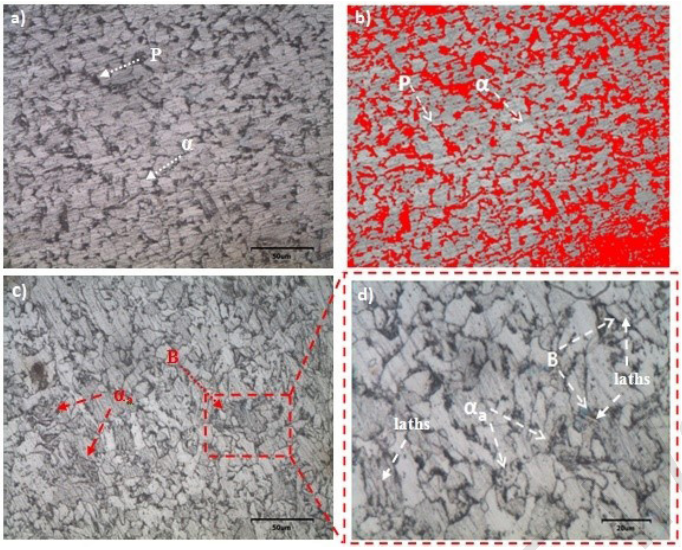

Figure 7: Optical photographs of CMTAW cylindrical component, a) and b) bottom region, b) top region at lower magnification and c) top region at higher magnification.

[**Figure 8**] shows the SEM micrograph of the bottom region of the GMAW cylindrical component composed of fully ferritic structure and top regions consists of GBF and α_w confirmed at higher magnification in SEM analysis. [**Figure 9**] shows the SEM micrograph of the bottom region of the CMTAW cylindrical component composed of a ferrite and small strips of pearlite (confirmed high %C in EDS). [**Figure 9**] shows the top region of the SEM micrograph, revealing the formation of B (laths formed in the grain) and α_a due to the fast cooling of the CMTAW process.

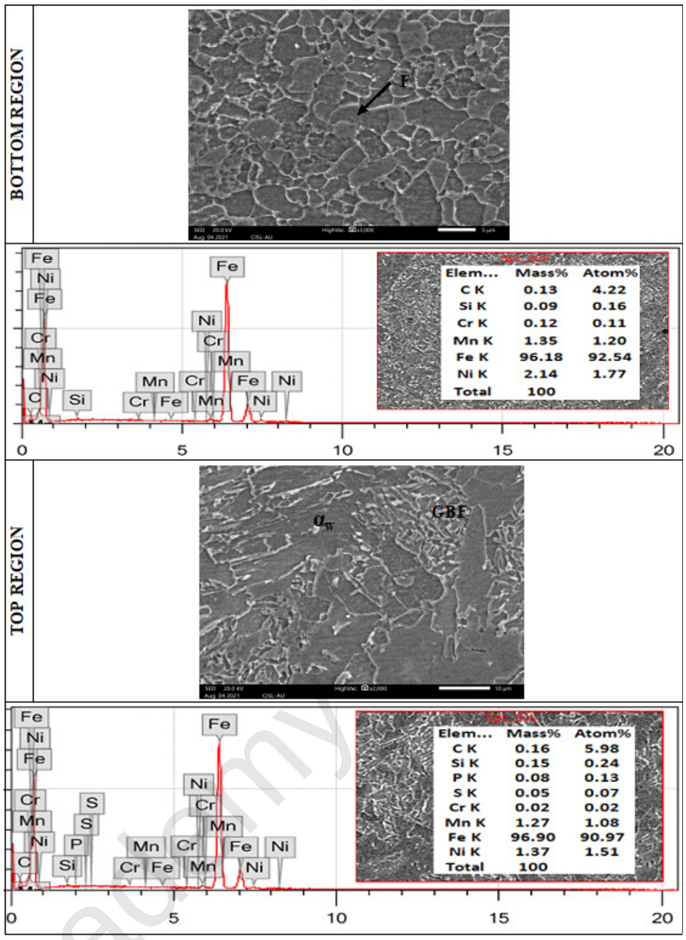

Figure 8: Micrographs of GMAW cylindrical component

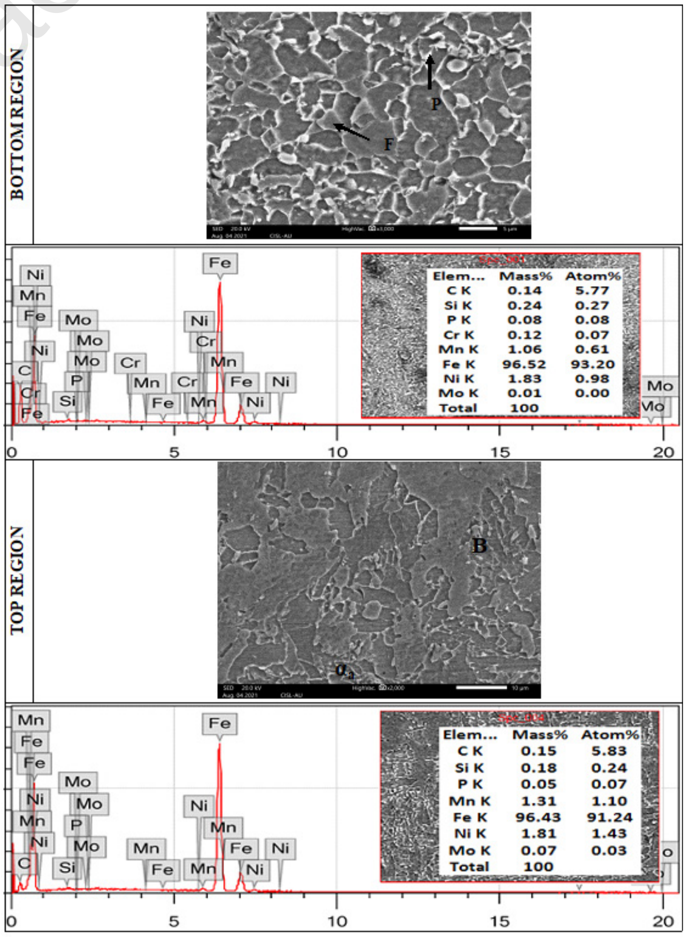

Figure 9: Micrographs of CMTAW cylindrical component.

Component	C	Si	Mn	Cr	Mo	Ni	P	S	Fe
GMAW	$ 0.13	$ 1.10	$ 1.69	$ 0.10	$ 0.14	$ 0.14	$ 0.02	$ 0.02	Bal
CMT	$ 0.12	$ 0.96	$ 1.70	$ 0.98	$ 0.13	$ 0.13	$ 0.02	$ 0.02	Bal

Table 4: Chemical composition (wt.%) of as built components.

The chemical analysis of the built carbon steel cylindrical components was confirmed by Optical Emission Spectroscopy (OES). The wt% of chemical elements of the manufactured components is presented in [**Table 4**]. The chemical composition of the WAAM cylindrical components was fairly similar to that of the ER70S-6 filler wire. The mixture of α_w and GBF (at medium cooling rates) formed in the GMAW cylindrical component due to high heat input (0.502 kJ/mm). The low heat input (0.384 kJ/mm) of the CMTAW cylindrical component resulted B and α_a (at fast cooling rates). However, the different types of microstructures like PF, α_w, GBF, α_a and B were formed due to different thermal histories. The transition of austenite to ferrite takes place between 500 and 800°C, and the microstructure generated following this transformation is controlled by time and cooling time.

XRD Analysis

The XRD pattern of the WAAM carbon steel components was carried out for phase identification from the bottom and top regions along the building direction of GMAW and CMTAW cylindrical components, and recorded spectra's were presented in [**Figure 10**]. As clearly revealed, the WAAM cylindrical components primarily consist of α-Iron located at 2θ of approximately 46.22°, 66.34° and 82.14° in the GMAW component and 46.16°, 66.10° and 82.16° in the CMTAW component according to the JCPDS patterns of 98-000-9982. They have a strong preferred orientation along the (110) plane at 2θ = 46.16° and 46.22° in GMAW and CMTAW components. Other diffraction peaks, (200) and (211), with less intensity were also found. Further, the α-Iron (110) peaks have the same position in bottom and top regions of both the components. However, when comparing with the GMAW and CMTAW components, the relative intensity of α-Iron (110) and (211) peaks vary with the heat input increasing (in GMAW component) or the heat input decreasing (in CMTAW component). It indicates that while the decrease of heat input in CMTAW component promotes the (110) orientation, the increase of heat input in GMAW component has the opposite effect on (211) orientation. The XRD measures have also indicated that the austenite (Iron-FCC) phase is not present, and confirm that either the retained austenite is not produced or its volume is too low below the XRD detection limit. Also, because of the significantly reduced volume fraction of the XRD spectrum relative to the ferrite phase, the precipitated cement phase was not identified. The similar XRD patterns confirmed from bottom and top regions along the building direction is strong evidence for the uniform and homogeneous microstructure along the building direction of the cylindrical components.

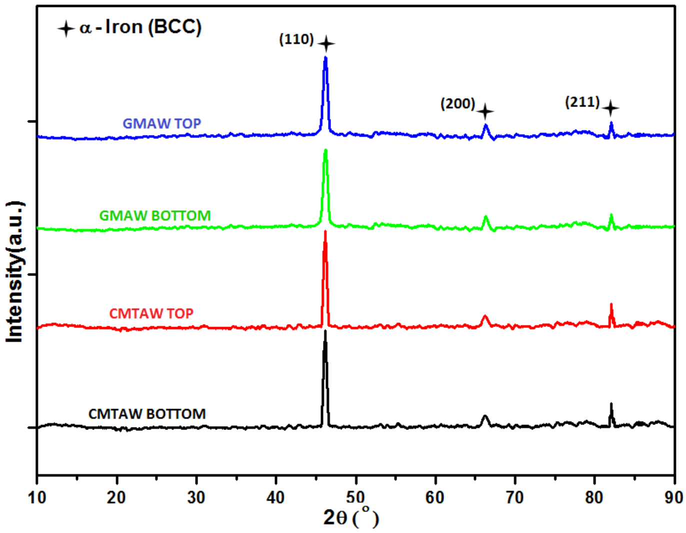

Figure 10: XRD pattern of the GMAW and CMTAW cylindrical components at bottom and top regions.

Conclusion

In this study, ER70S-6 low-carbon steel cylindrical wall components were wire-arc additively manufactured utilizing GMAW and CMTAW-WAAM processes. The microstructural characteristics of the manufactured components were characterized in different regions along the building direction. The following important findings are drawn from this study:

- The variation in heat input levels has significant effects on the grain size, but does not significantly influence the microstructure evolution and the microstructure type of the built cylindrical components.
- The grain size is finer in the CMT-WAAM cylindrical component than in the GMAW-WAAM cylindrical component because it experienced a higher value of thermal shock than the CMT-WAAM cylindrical component that has a coarse grain size.
- The microstructure of the built cylindrical-walled component varies from the top to the bottom regions and can be distinguished into two regions: lamellar structures (α_w and GBF) in the top regions; and equated grains of fully ferrite in the bottom region in GMAW.
- In the CMT-WAAM cylindrical component samples have been noted two different regions: the bottom region characterized by a ferritic structure with thin strips of pearlite and the top region characterized by a lamellar structure typically B with α_a.

Acknowledgement

The first author is grateful to the Department of Science and Technology (DST), Ministry of Science and Technology, Government of India, New Delhi for the financial support rendered through Fellowship under PURSE-Phase-2 scheme. The authors wish to record sincere thanks to M/s. Fronius India Pvt. Limited, Chennai for technical support.

References

1. Thornton A. Additive Manufacturing (AM): Emerging Technologies, Applications and Economic Implications, Nova Science Publishers: New York, United States. 2015.
2. Ding D, Pan Z, Cuiuri D. Adaptive Path Planning for Wire-Feed Additive Manufacturing Using Medial Axis Transformation. J Cleaner. Prod. 2016;133:942-952.
3. Jin W, Zhang C, Jin S, et al. Wire Arc Additive Manufacturing of Stainless Steels: A Review. Appl Sci. 2020;10:1563.
4. Gu J, Cong B, Ding J, et al. Wire+Arc Additive Manufacturing of Aluminium. SFF Symp. 2014;451-458.
5. Tabernero I, Paskual A, Pedro A. et al. Study on Arc Welding Processes for High Deposition Rate Additive Manufacturing. Procedia. CIRP. 2018;68:358-362.
6. Fronius. Document: Cold Metal Transfer. 2014;16.
7. Selvi S, Vishvaksenan A, Rajasekar E. Cold Metal Transfer (CMT) Technology - An Overview. Defence Techn. 2018;14:28-44.
8. Deruntz, BD. Assessing the Benefits of Surface Tension Transfer Welding To Industry. J Indu Tech. 2003;19:55-62.
9. Sridharan N, Noakes MW. On The Toughness Scatter in Low Alloy C-Mn Steel Samples Fabricated using Wire Arc Additive Manufacturing. Mater.- Sci.- Eng: A. 2018;713:1827.
10. Rodrigues T.A, Duarte V, Avila J.A, et al. Wire and Arc Additive Manufacturing of HSLA Steel: Effect of Thermal Cycles on Microstructure and Mechanical Properties. Addit. Manuf. 2019;27:440450.
11. Dai YL, Yu SF, Shi YS, et al. Wire and Arc Additive Manufacture Of High-Building Multi-Directional Pipe Joint. Int J Adv Manuf Tech. 2018;96: 2389-2396.
12. Li C, Gu H, Wang W, et al. Effect of Heat Input on Formability, Microstructure, and Properties of Al–7Si–0.6 Mg Alloys Deposited by CMT-WAAM Process. Appl Sci. 2020;10:1-8.
13. Scotti A, Ponomarev V, Lucas W. Interchangeable Metal Transfer Phenomenon in GMA Welding: Features, Mechanisms, Classification. J Mater Process Tech. 2014;214:2488-2496.
14. Scotti A, Ponomarev V, Lucas W. A Scientific Application Oriented Classification for Metal Transfer Modes In GMA Welding. J Mater Proc Tech. 2012;212:1406-1413.
15. Yadollahi A, Shamsaei N, Thompson S.M, et al. Effects of Process Time Interval and Heat Treatment on the Mechanical and Microstructural Properties of Direct Laser Deposited 316L Stainless Steel. Mater Sci Eng A. 2015;644:171-183.
16. Cong B, Ding J, Williams S. Effect of Arc Mode in Cold Metal Transfer Process on Porosity of Additively Manufactured Al-6.3%Cu Alloy. Int J Adv Manuf Tech. 2015;76:1593-1606.
17. Wang Z, Palmer TA, Beese AM. Effect Of Processing Parameters on Microstructure and Tensile Properties of Austenitic Stainless Steel 304L Made by Directed Energy Deposition Additive Manufacturing. Acta Materialia. 2016;110:226-235.
18. Le V, Banh T, Nguyen D, et al. Wire Arc Additive Manufacturing of Thin-Wall Low-Carbon Steel Parts: Microstructure and Mechanical Properties. Int J Mod Phy B. 2020;34:1-10.
19. Le V, Hoang Q, Tran V, et al. Effects of Welding Current on the Shape and Microstructure Formation of Thin-Walled Low-Carbon Parts Built by Wire Arc Additive Manufacturing. Viet J Sci Tech. 2020;58:461-472.
20. Lee HK, Kim KS, Kim CM. Fracture Resistance of a Steel Weld Joint Under Fatigue Loading. Eng Fract Mech. 2000;66:403-419.
21. Prasanna Nagasai B, Malarvizhi S, Balasubramanian V. Mechanical Properties Of Wire Arc Additive Manufactured Cylindrical Component Made By Cold Metal Transfer Arc Welding Process. Mater Test. 2022;64:260-271.
22. Prasanna Nagasai B, Malarvizhi S, Balasubramanian V. Mechanical Properties and Microstructural Characteristics of Wire Arc Additive Manufactured 308 L Stainless Steel Cylindrical Components made by Gas Metal Arc and Cold Metal Transfer Arc Welding Processes. J Mate Pro Tech. 2022;307:1-20.
23. Kim YM, Lee H, Kim NJ. Transformation Behavior and Microstructural Characteristics of Acicular Ferrite in Line Pipe Steels. Mater Sci Eng A. 2008;478:361-370.
24. Hwang B, Kim YM, Lee S, et al. Correlation of Microstructure and Fracture Properties of API X70 Pipeline Steels. Matell Mater Trans A. 2005;36:725-739.

Citation: Bellamkonda PS, Sudersanan M, Visvalingam B. Metallurgical Characteristics of Low Carbon Steel Cylindrical Components Made by Wire Arc Additive Manufacturing (WAAM) Technique. J 3D Print Addit Manuf. 2022;1:1-7.

2018

Residual Stresses Analysis of 3D Printed Plate By using Wire Arc Additive Manufacturing -WAAM-

Abdulrahman Amer Alrumayh
Lehigh University, aaa216@lehigh.edu

Residual Stresses Analysis of 3D Printed Plate By using Wire Arc Additive Manufacturing -WAAM-

by

Abdulrahman Alrumayh

A Thesis

Presented to the Graduate & Research Committee

of Lehigh University

in Candidacy for the Degree of

Master of Science

in

Mechanical Engineering

Lehigh University

August 2018

This thesis is accepted and approved in partial fulfillment of the requirements for the Master of Science.

Date

Thesis Advisor

Herman F. Nied

Chairperson of Department

D. Gary Harlow

Acknowledgment

My thanks go firstly to my parents and my family for their support through my life.

After them, the thanks must be for my teachers and professors through my learning path even who taught me a letter.

My successes and achievements are their efforts outcomes, so thanks for them from bottom of my heart.

I would like to thank especially my supervisor Professor Herman F. Nied for his support, guidance, and understanding through my master program.

Table of Contents

List of tables

List of figures

Abstract

Additive manufacturing represents a relatively newly developed technology with many rapidly changing innovations . One of the most important processes in additive manufacturing is 3D printing. For a couple of decades, polymers have dominated the materials used in 3D printing. In the last few years, 3D printing of metals has had a high impact on interest in this technology. One 3D printing process that uses metals is Wire Arc Additive Manufacturing (WAAM). This technique has some technical obstacles that may detract from its use in commercial applications. One of the crucial issues concerns the control of residual stresses and related distortions. The evolution of residual stresses can theoretically be simulated by using computational software for the WAAM process, in a manner similar to welding process modeling, using nonlinear finite element codes such as ABAQUS, ANSYS, SYSWELD, etc. This study focuses on using SYSWELD to model the WAAM process.

In this thesis, the key reference problem is the simulation of the WAAM process for a vertical 3D printed plate. This “reference” problem was chosen because =WAAM printed plates have been fabricated at Lehigh University and thus, comparisons can easily be made between simulations and experimental measurements. The simulated WAAM parts examined in the study compare two types of steel alloys: 1) austenitic stainless-steel grade 316L and, 2) Low carbon steel S355J2G3. The residual stress components of particular interest were determined to be: 1) Longitudinal stresses across the width of the plate and, 2) the maximum principle stress. The distortion of the WAAM plate after the metal deposition processes are complete illustrate the difficulty in maintaining dimensional tolerances. The simulation process predicts higher residual stresses and lower distortion for the low carbon steel alloy, when compared with the austenitic stainless steel.

Chapter 1 introduction

Additive Manufacturing

3D-printing is a trending method of manufacturing that presents researchers with a myriad of promising outcomes as well as challenges. 3D-printing has gained enormous attention recently and is perhaps the break-through technology of this manufacturing era – just as the steam engine and combustion engine once were. 3D-printing is also known as additive processes, or additive manufacturing [1]. The Principle of Additive manufacturing starts many years ago when mankind started to build houses, for example building walls uses additive manufacturing in large scale using stacked blocks. The wide difference in the materials used in additive manufacturing, or building, and the variety of designs and properties of the materials, made it hard to precisely define 3-D printing, at least until 3D CAD was developed. Powerful 3D CAD software now makes it easy to build a shape for virtually any desired shape and specified material properties [2].

History

The history of additive manufacturing is not new; in fact, the concept of additive manufacturing started by using photo sculpture back in the 1860s, which was further developed later [3]. It started with the concept of building layer by layer in the early of 1900's , "back to Peacock for his patented laminated horse shoes in 1902" [4]. About a quarter a century later, Baker patented "The use of an electric arc as a heat source to generate 3D objects depositing molten metal in superimposed layers" in 1926 Figure 1.1[5]. He used a new technique to build a 3D object , which had not yet been employed, by using welding processes [6]. So, this attempt could be considered as the oldest attempt to use welding technology in additive manufacturing, which is known later as Wire Arc Additive Manufacturing WAAM.

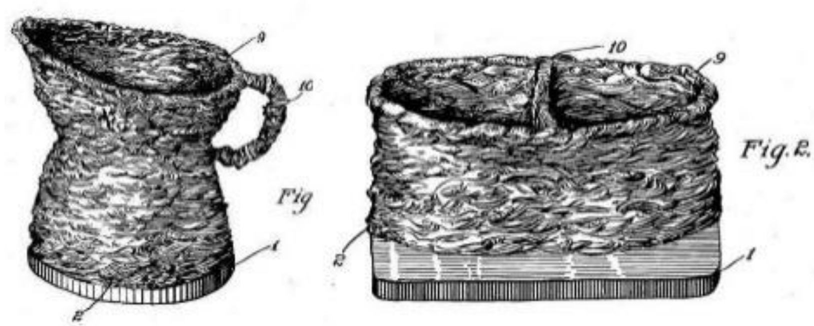

Figure 1.1 : Baker's models in 1926 using molten metal [5].

After 25 years in 1951, a new technique was patented ''Photo-glyph recording'' technique[3]. In 1952, Kojima indicated the importance of layer-by-layer processes, and in the next 30 years, many patents were filed related to 3D printing processes by using layer-by-layer techniques. The more modern patents and new research were based on the 1950s' principle[4] of 3D-printing. In the 1960s, and after, many attempts were made to use a laser to solidify specific points on a polymer sheet, these attempts were not used until they were developed with other techniques. Later in 1987, Stereolithography (SL) for 3D was established, which used a laser to solidify thin layers of light-sensitive ultraviolet liquid polymer[7].

Definition

ASTM defines additive manufacturing as the "process of joining materials to make parts from 3D model data, usually layer upon layer, in contrast to subtractive manufacturing and formative manufacturing methodologies" [8]. This definition makes the concept of additive manufacturing very broad, so as to include many processes, not just 3D printing. Also ASTM "specifies other commonly used synonyms for AM (additive manufacturing) including additive fabrication, additive processes, additive techniques, additive layer manufacturing, layer manufacturing, and freeform fabrication" [9].

Importance and Promise able Future

In recent years, AM has received considerable attention from many institutions and research centers around the world. One of the best aspects of AM is the potential for zero waste during the manufacturing process, which will likely reduce costs [10]. Traditional manufacturing processes for complex parts can often be quite expensive and may not offer efficient solutions for the manufacturing of complex shapes. AM potentially offers an inexpensive solution for complex manufacturing problems [11]. Another crucial point is AM has the ability to repair and fix broken parts. Furthermore, it has the ability to collaborate with conventional manufacturing processes[12]. AM has another advantage that distinguishes it from other manufacturing processes, which is the ability to deal with most kinds of materials: polymeric materials, composites, ceramics, and metals. Of course, traditional manufacturing processes will never be completely displaced by AM, but for a large class of applications AM may provide the most effective manufacturing solution [13].

Cost and mass production are very important in nearly all industries. AM offers a sort of balance between cost and mass production. On the other hand, traditional manufacturing has an inverse relationship between cost and volume, which makes traditional methods much cheaper than AM Figure 1.2 when a large number of identical components are being produced. In contrast, complexity of the product often makes traditional manufacturing more expensive than AM Figure 1.3 [12].

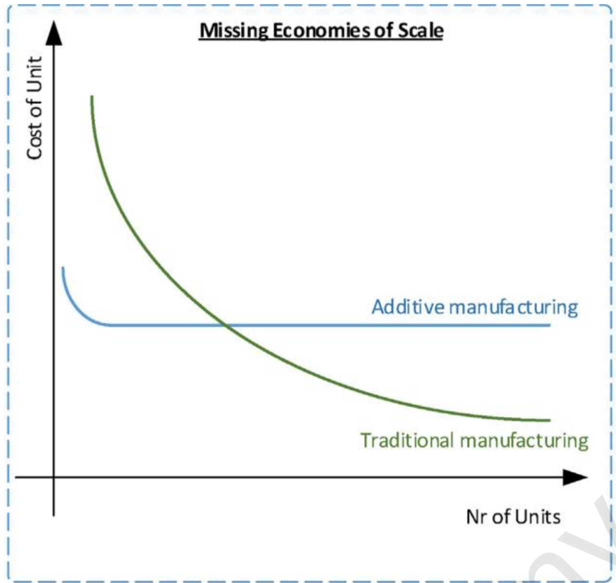

Figure 1.2 : Relationship between the cost and Number of products for AM and traditional ways[12].

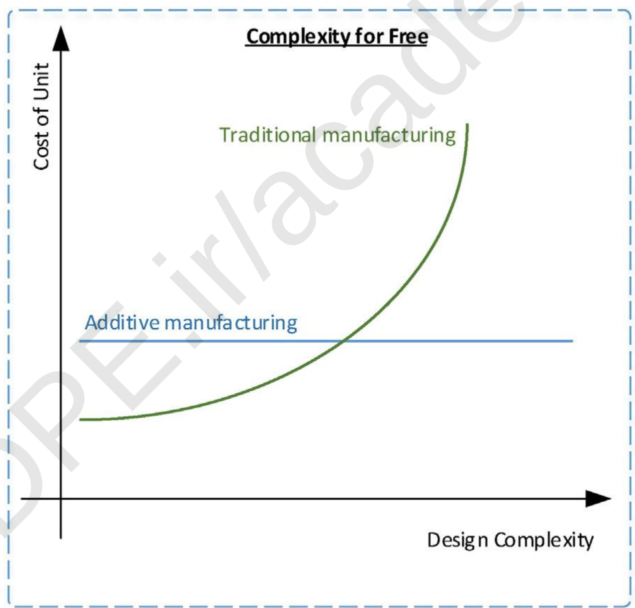

Figure 1.3 :Relationship between the cost and design complexity for AM and traditional ways[12].

Throughout the last thirty years, AM research has grown exponentially. Nowadays, AM is the subject of, or included in a variety of, research topics [4]. AM has huge economic impacts as well; Wholers report [14] mentioned that the AM market could reach $7 billion by 2019. In the past, AM has had a high growth rate of approximately 26% [9], also AM is expected to grow continuously through the years. AM is sometimes called the “third industrial revolution”, because industries and factories are starting to use AM in the manufacturing of their products on a large scale. Some AM techniques are available commercially, such as 3D by laser or electron beam deposition. But some additive processes are still not commercially available, e.g., WAAM (Wire Arc Additive Manufacturing), which still has some technical challenges such as residual stresses, deformation, microstructure grain, and low quality of surface finishing. These challenges directly related to the enormous heat input [15] associated with an electrical arc. One may also consider the protection of the existing patents and trademarks as obstacles for some of the additive technologies to be commercially available [16].

Overview 3-D Printing

3D printing, or AM, provides the user more freedom to fulfil the desire of the consumers in many aspects of the manufacturing process, such as volume, cost, weight, design, and properties[17]. 3D printing in a simple definition is a way of joining many elements by using heat source to melt and join. 3D printing has different techniques, which depend on the heat source, feeding technique, and feed material. Most feeding systems use blown powder, powder bed, and the wire feed techniques, and the heat source is typically a laser, electron beam, or electric arc [10]. However, other techniques also exist, such as selective laser sintering, direct metal deposition, electron beam freeform fabrication, shape deposition manufacturing, wire and arc additive manufacturing (WAAM), etc.[18].ASME includes many types in their classification for AM technologies. ASME has created seven categories for the types of AM using metal and other materials : (1) material extrusion, (2) powder bed fusion, (3) vat photopolymerization, (4) material jetting, (5) binder jetting, (6) sheet lamination, and (7) directed energy deposition[3]. Concerning metal applications, directed energy deposition can be divided into two subcategories of feeding, powder and wire. The wire feeding system could be used with a different heat source, but the simplest system uses an electric arc heat source and is designated WAAM. WAAM is efficient for large size components. Also, it is considered the lowest cost and safest method with a high metal deposition rate. As a comparison, WAAM can attain deposition rates of 50-130 gram/minute, whereas powder-based systems can only offer 2-10 gram/minute. WAAM is essentially a multi-pass welding process, utilizing one of the most common welding techniques, i.e., GMAW (Gas Metal Arc Welding) [15]. For metal applications, titanium and its alloys, steel, aluminum, and nickel alloys are typically used in WAAM processes. Despite the benefits of AM, some of the techniques have defects and issues, such as the residual stress and the surface finishing. This leads to poor quality of the mechanical properties of the desired product[14]. Overall, AM is a manufacturing process that uses continuous heat input localized to a specific feeding material to change its matter from solid to liquid for a specific size in the melted pool. In order to be solidified in a certain shape that makes the final design of the deposited layers[19].

Polymers are the most dominant materials used in AM, because of their low melting point and high viscosity, which assists with the layer-by-layer deposition process. However, the metal AM developed techniques increase the portion of metal AM application in the market.[17].

Metal 3-D Printing

This thesis focuses on metal AM, especially on WAAM. As mentioned previously, metal AM can be divided into two categories and each category has three main sections. The two categories are the feeding system and the second is the heat source. The sections of the feeding systems are powder bed, powder blown, and wire. And the heat sources are laser, electron beam, and electric arc. Electric arc AM is the main subject in this research. The performance of metal printers is based on the final products' residual stresses, distortion, microstructure, and mechanical properties [20]. Also, the feeding systems have been divided into two main types, direct and indirect deposition systems. The direct deposition system melts all the particles to obtain the final design, while indirect systems use a binder to join particles [21].

The deposition efficiency of wire-based AM is higher than other types, for example wire based AM deposition efficiency can approach 90%, while in powder-laser is around 40%[22]. That gives some credit for wire feed systems. deposition efficiency is calculated by the amount of metal is used vs the amount of metal is remain after the processes.

Powder Bed

Powder bed uses a container full of powder that allows the heat source to melt layer by layer. Between two layers, the container moves down to allow for an out slide to feed more powder [23]. This yields a new powder layer above the old melted one as shown in Figure 1.4.

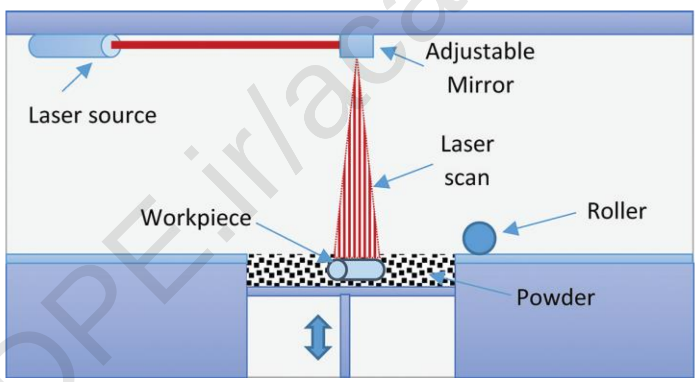

Figure 1.4 :diagram shows powder bed with laser[24]

Powder bed uses either a laser or electron beam as a heat source, because of their accuracy and precision. However, powder bed is best suited for small-sized products, since the size depends on the container itself [10] and because the deposition rate is low for this technique. The larger commercial size powder bed-based AM is around 0.16 m^3 with deposition rate of 0.2 kilogram/hour[22]. Powder bed processes utilize several deposition techniques, which include ALM (Additive Layer Manufacturing) , SLM (Selective laser melting) , DMLS (direct metal laser sintering) , DMLM (Direct metal laser melting) [25]. Some of these processes, e.g., LM (Selective laser melting), have issues with the fast cooling rate, which cause distortion in the final product [26].

Powder blown

Powder blown was used as a welding manufacturing process even before its application in AM. This process uses a nozzle to blow powder to a certain area where the heat source focuses on this area, so that the heat melts the powder as shown in Figure 1.5.

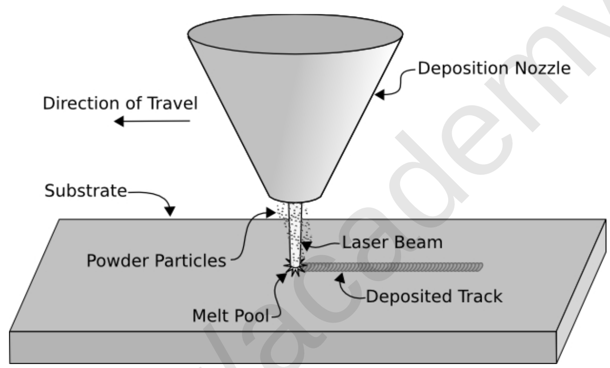

Figure 1.5 :diagram for powder blown system with laser heat input [27]

As in powder bed, blown powder has different techniques such as DLMD (Direct Laser Metal Deposition), LMD (Laser Metal Deposition), LENS (Laser Engineered Net Shaping) [25].

Wire Feed

The third AM metal feeding system is wire feed, which is considered the most efficient system in terms of materials usage. Moreover, it is considered the cleaner and safer for the environment in addition to the low cost [28]. Of course, the wire feeding system is not a hazard to the atmosphere, in contrast to powder processes [29]. The wire feed system as shown in Figure 1.6 uses the same principle as the powder blown system, i.e., the feeding materials are blown or deposited by the feeder in the interest area where is the heat is applied [30].

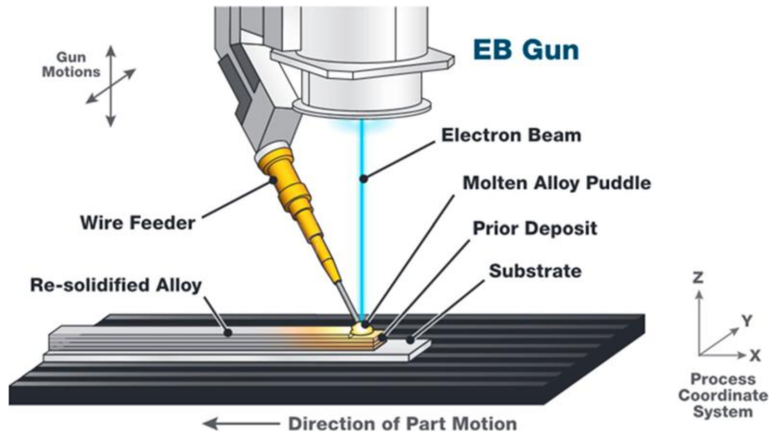

Figure 1.6 : diagram of wire feed system with electron beam heat source[31]

There is plenty of research that has studied wire feeding systems in welding processes. But AM uses this process repetitively many times in one product, and this is the primary difference between welding processes and AM. The AM deposition process is simply a multi-pass welding process. In contrast to the previously discussed AM processes, wire feeding systems have the lowest accuracy because the diameter of the wires are larger than the size of the powder in other processes, so it is hard to build a very intricate product using a wire feeding system[19].Heat source power types

AM uses a variety of heat sources and joining processes to build a product. However, metal-based AM typically uses a laser for the heat source, as well as an electron beam or electric arc. Each one of these is used in certain applications, depending on the desired product.

Laser AM is most popular and can be used for the three aforementioned feeding types. In addition, laser processes have a high accuracy, around 20 µm, which gives it an advantage [32]. On the other hand, laser AM has a fast cooling rate, which can introduce defects in the final product [33]. Furthermore, laser AM has poor energy efficiency compared to other processes, around 5% [34].

The fundamental principle behind electron beam AM is that an electron beam ,i.e., a stream of electron, passes through the feeding materials. Electron beam AM is more efficient in energy term than laser AM, around 20%. On the other hand, it has disadvantages that make the process cost more, e.g., electron beam AM requires a vacuum environment. Although, some consider this to be an suitable for aerospace applications since the vacuum environment is already exist [34].

Electric arc systems also use the same principle as electron beam AM, but there is a slight difference between the electric arc and the electron beam AM regarding the lower energy density heat source. This difference makes the melting rate lower than electron beam and laser systems [35]. The energy efficiency of the electric arc in certain circumstances can be as much as 90%, as in gas metal arc welding (GMAW) or gas tungsten arc welding (GTAW) processes. Further, electric arc AM is capable of handling large-sized products[28]. Electric arc and wire feeder AM can be combined, which is called WAAM. WAAM has a high deposition rate, lower system and material costs, and a lower probability of oxide contamination [34] [36].

WAAM

WAAM (Wire Arc Additive Manufacturing) offers a promising area for research and has many advantages. WAAM is often favored over electron beam and laser systems. The main reasons for this are the cost, the vacuum environment, easier operation, and non-reflectivity problems [37]. The most frequently employed techniques used in WAAM are Gas Metal-Arc Welding (GMAW) and Gas Tungsten-Arc Welding (GTAW). These methods have a high deposition rate and the ability to build large and small products, up to few meters[38]. Further, compared to traditional manufacturing processes, these methods efficiently use raw materials[11]. Unfortunately, it is generally conceded that WAAM processes can introduce enormous residual thermal stresses; which is usually not the case in powder bed systems [39]. WAAM is based on the welding process.

However, automation of the WAAM process is what has significantly increased printed product quality. Figure 1.7 illustrates two diagrams of GTAW and GMAW. Both processes use electric arcs that are created by applying an electric potential between the base metal and the welding electrode; in GTAW the electrode is non-consumable, while in GMAW the electrode is the feeding material. The melting pool is protected by an inert shielding gas. The processes are operated by a robot, so the feeding rate and heat input are systematically controlled and there is a high deposition rate – up to 10 kg/h [40].

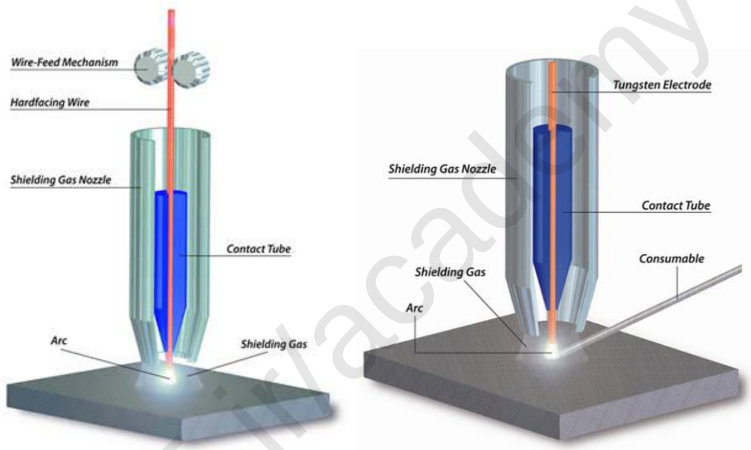

Figure 1.7 :diagrams describe GMAW (left) and GTAW(right) welding processes[41]

WAAM has not received the same attention as other AM technologies, because of the unresolved technical problems described in this chapter. Further, it is important to mention that WAAM has poor accuracy around ±0.2 mm vs ±0.04 mm for powder based, one of the reason is the size of the melting pool , and high distortion effects that render WAAM unacceptable for many manufacturers [30].

WAAM is a type of welding process, so the parameters relevant to the welding process are equivalent.

The most important parameters are the arc voltage, arc current, shielding gas, nozzle-base distance, travel speed, feeding speed, and wire diameter. These parameters effect the weld bead geometry, resultant distortion, and resultant residual stress[42]. For example, variation in the distance between the nozzle and the base leads to poor shielding quality and introduces deposition defects, or creates a spatter areas on the product [43]. In addition, the high deposition rate leads to a thicker bead, which affects the microstructure grain patterns growth, since the thicker bead needs more time to solidification processes[44].

Advantages

WAAM impacts the environment by 70% less than traditional machining impacts on the environment such as raw material extraction issues, recycling ability[9]. WAAM has the potential to be a non-waste technique through development of the process toward ready-to-use products, especially for mechanical properties and surface finishing [37]. In addition, WAAM is an easy system to build and supply.. Considering costs, a WAAM system is still one of the cheapest AM technologies. Moreover, WAAM is suitable for building small or large sized products with medium complexity[42]. In certain situations, a thermal gradient causes a tendency towards anisotropic material properties [45].

Disadvantages

Despite its advantages, WAAM is considered to be an unsuitable technology for some applications. Since the diameter of the wire is large compared to powder systems, the accuracy of WAAM is lower than powder (±0.2 m-wire, ±0.04 mm-powder). For complex products, WAAM may not a great choice for manufacturing [42]. WAAM has a high heat input with thermal concentrations in certain areas, which leads to deformations and may cause cracks.   This is due to thermal gradient effects [46]. WAAM works using the same principles as EB, where electrons are transferred to the work area. However, WAAM has a lower energy density than EB or laser AM with a slower rate of transferring. This causes larger melting pools than in other AM processes and techniques. The melting pool for WAAM is affected by fluid flow effects, which controls the shape of the melt pool and initiates its penetration. These considerations must be accounted for in order to obtain good surface finish and uneven ends of the final geometry [35].

Applications

WAAM machines are currently not commercially available because of the shortcomings described above[18]. Nevertheless, WAAM is greatly developing in aerospace, biomedical, automotive, and energy applications [32] [21]. Also for printed parts, there some companies has successfully printed a verified and tested parts by using WAAM , such as Damen Shipyards who announce a 3D printed boat propeller as appear in Figure 1.8 [47].

Figure 1.8 Ship propeller has been made by Damen Shipyards[47]

Metal 3-D Printing Issues and Challenges

In order for AM to be widely implemented in society, it must meet the expectations of the consumer and stand up against economic barriers. Unfortunately, there are obstacles preventing AM from replacing traditional manufacturing processes. Many of these problems are related to a lack of fusion, porosity, vaporization, mechanical properties, grain structure, surface finish, deformation, residual stress, cracking, and uneven geometry.[10] Some of these issues are the result of thermal effects, which could be solved by a heat treatment [9].

Porosity is a common defect in welding processes, including WAAM. Porosity refers to any unwanted cavity inside the work piece. Typically, these unwanted porous defects are caused by gas trapped inside the work piece during the welding process that is unable to escape prior to solidification. Poor control of the shielding gas often results in unwanted porous defects. Other reasons for such defects are raw material impurities and insufficient flow rates. Regularly, cavities occur near the edges of the molten tracks. As porosity increases, material properties such as ductility, strength, and stiffness decrease[8] [48]. Figure 1.9 illustrates a porous area, whose defects formed during the welding process for an aluminum alloy involving only a single pass.

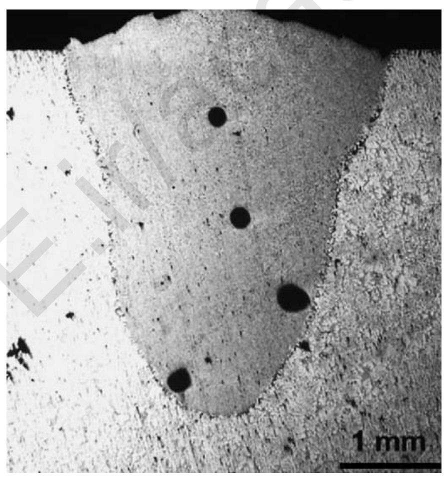

Figure 1.9 :Porosity defects for an aluminum alloy[49]

The quality of the weld bead profile is a common controllable issue, caused by three main factors: humping, undercutting, unsymmetrical beads. Humping refers to an uneven bead profile in the direction of the welder, which causes ups and downs on the layer. Undercutting and unsymmetrical beads refer to the bead located in an undesired position or having an undesired shape. Undercutting occurs between the two different layers, or the base, while unsymmetrical bead occurs for a single bead. These issues are usually caused by a high travel speed and with an uncontrolled deposition. As a result, any missed spot will affect subsequent layers, which results in defects in the final desired product[48] [50]. With GMAW, the profile assumed at both ends of a square plate, built by AM, assume a different shape than the middle of the plate. This is caused by the shape and depth of the weld penetration, which causes differences in the thermal distribution, which in turn leads to sloping at the end and humping at the start [15]. Figure 1.10 shows the unbalanced endings, which are created by thermal distribution and surface tension effects.

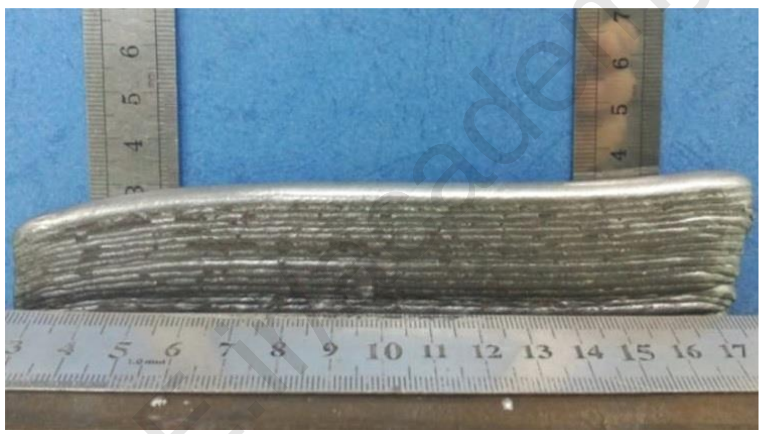

Figure 1.10 :a plate AM based, start(right) , end (left) [43]

Grain structures **contribute** in the cracking behavior in the work piece, which are dictated by the thermal distribution while cooling. Shrinking leads to crack formation at the grain level. Furthermore, shrinking occurs when high thermal gradients are present, which leads to a high cooling or heating rate. Generally, materials with low ductility are the first to exhibit cracking. Chemical degradation and oxidation are two more minor issues relevant to AM for metal applications because they are easily controllable, [8].

Deformations and distortions are very common issues in welding. Thermal gradients cause deformations that eventually may lead to cracking. We know from the basic principles of thermal expansion that most materials shrink upon cooling and expand upon heating. So, when these cases happen at a certain spot, then distortion occurs at this location due to differences in the local thermal stresses. Figure 1.11 shows a concaved work piece. Clamping temporarily stops deformations, but heat treatment is required for a more complete solution[8].

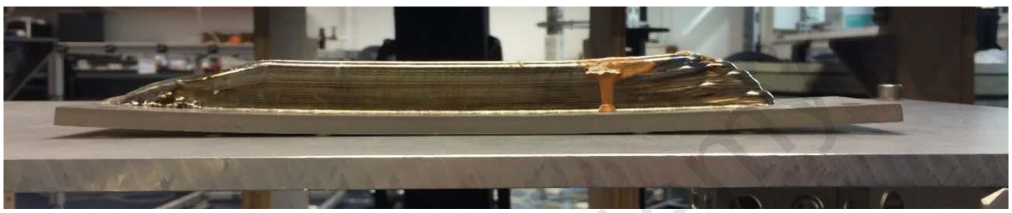

Figure 1.11 :3D printed work piece is concaved[41]

Poor surface finishing is a concern for most AM technologies. Usually powder feeding systems are concerned with the coarse surface; while in wire feed systems the surface is fine. Interestingly, the sides form a sort of sinusoidal surface, like what happened in the side of the shown piece in Figure 1.10. Moreover, coarse surface could happen in WAAM if the shielding gas is inadequate or welding parameters are inappropriate. Usually, the solution for a good quality surface finish requires traditional machining processes[8]. Figure 1.12 shows undesirable and uneven sides of an AM work piece, i.e., it needs further processing prior to its use.

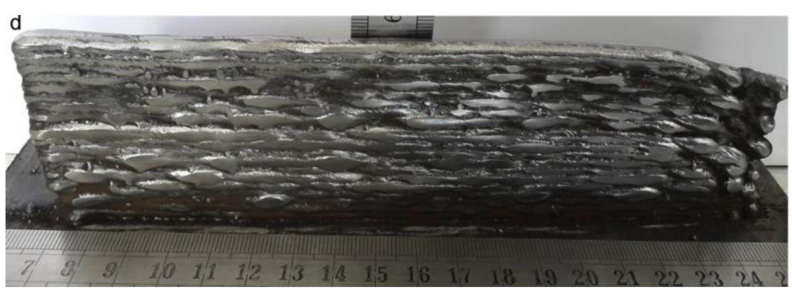

Figure 1.12 :Poor profile caused by uneven bead[13]

Of critical concern in WAAM are the welding residual stresses, which are associated with distortions in the finished work piece. Throughout AM, the first layers are reheated several times, due to the heat of subsequent bead layers. This induces a thermal cycle for each layer, which ends on the final layer or by steady cooling rate[51]. WAAM, as mentioned, is a high heat input process, which makes the affected zone large and may lead to shrinking in the affected areas. If the thermal gradients are large enough, and the workpiece is sufficiently constrained, the residual stresses will be high. In some cases, the internal stresses are relieved when the work piece is unclamped. Usually, the largest residual stresses arise in the direction of the deposition[50]. There are two residual stress states of particular interest. The first is the residual stress state immediately after the manufacturing process is finished, but before the part has completely cooled The second residual stress state is the final state after the work piece has been cleaned up and cooled [34].

Experimental Processes

CAD technologies have revolutionized manufacturing at large, and is responsible for the accuracy of AM. The first step is product design using CAD software. Then the design transforms to an acceptable file for the various slicing software such as STL files or G-code files to be rendered as 2D layers [52] [53]. After that, slicing software slices the design into special properties for the layers (layer dimensions, slice thickness, etc.) [39]. Then, using the new layer shapes, the software creates path trajectories (such as raster, zigzag, contours, etc.) to build each layer by using the digital information[18]. And the final step is a robot follows the paths and prints [37]. In WAAM systems, usually GTAW and GMAW are used so any system must contain (CAD software, slicing software, path software or tool, deposition controller (robot with multi-degree of freedom), heat source, materials supply) [37]. Typically, the controller regulates the power and heat input such that the process results in the deposited layers exhibit the desired material properties. The travel speed and the distance between the nozzle and the substrate can also be controlled to obtain the desired final product. In many applications of 3D printing of metal materials, there are two types of area characterizing the work piece: the total area and the effective area. The effective area is the desire area, while the rest of the total area must be removed to clean the effective one. For certain cases, 90% of total area is the effective area, while the remaining surface material must be removed. As shown in Figure 1.13 the substrate and the first few layers are removed intentionally to obtain the desired surface finish[12].

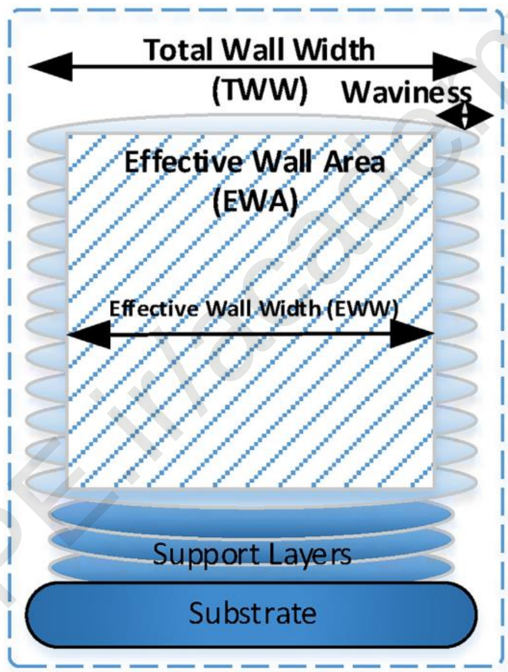

Figure 1.13 :A diagram shows the effective area as part of the total area[12].

Simulation Software

Recently, software has made it easier to simulate many AM processes by using numerical analyses based finite elements methods (FEM). Many approximations are made to model the real physical system, of course[54]. For welding manufacturing processes, common software packages are SYSWELD, ABAQUS, and ANSYS. SYSWELD is a specialty heat treatment and welding process software that uses numerical analyses such as FEM, to simulate the actual process at a relatively high level, up to three spatial dimensions[55]. "SYSWELD can obtain: temperature fields and thermal fluxes, phase proportions, hardness, distortions, residual stresses, and plastic strains distributions" [56]. Since AM is based on a well-known welding process, we can use these commercially available software packages to model and simulate AM processes in order to study mechanical properties. AM requires control of process parameters more than traditional processes[3]. Using such software in order to predict residual stresses and deformations saves time and money. The degree of accuracy predicted by the software is closely related to the computational time required, but generally speaking all of the aforementioned software packages yield reasonable results[6]. Figure 1.14 shows the actual and the predicated shape for a t-tube joint obtained from SYSWELD after a welding and loading process [57]. The accuracy of the SYSWELD software for estimating post-weld stresses and distortion is generally considered to be quite good.

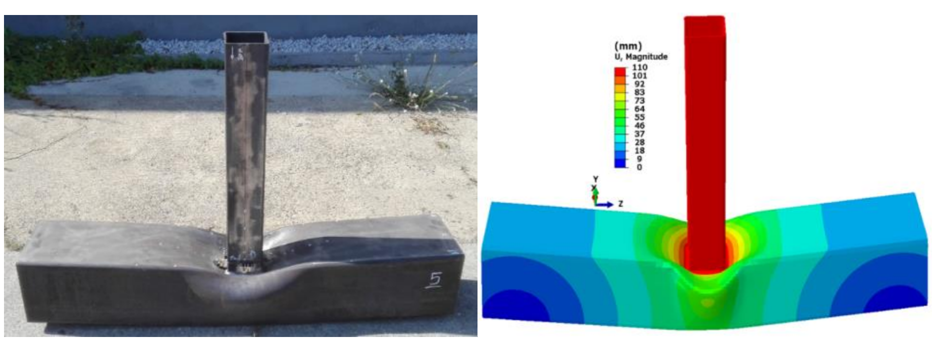

Figure 1.14 :A comparison between experimental (left), and computational (right) [57]

Residual Stresses Curing Researches

Lehigh University has WAAM capabilities and is being used for research studies in this AM technology. Haden and others said, "The 3D metal WAAM printer at Lehigh University is currently configured with a Millermatic 250 gas metal arc welder (Miller Electric Manufacturing Co.) and a roughly 0.53m Cartesian gantry positioning system (Macron Dynamics, Inc. and Parker Origa OSP-E25). The welding nozzle position is determined from CNC commands derived from a computer aided design (CAD) rendition of the desired part. The part is converted using open source software Slic3r engine (slic3r.org) to GCODE which dictates motion commands to the microcontroller." [58]. The two biggest challenges for Lehigh University and others in the field are the residual stresses and distortions obtained from WAAM processes. These two challenges are present due to the large thermal gradients present during the WAAM process.

In the past, thermal simulated models for arc welding did not consider convection heat transfer as a main part of the cooling rate for welding processes, despite its huge importance in arc welding processes, especially in the melting pool [59]. However, the available FEM software packages simulate the welding process with accurate results; so large heat input with high thermal gradients produce high residual stress and distortion [60] [61] [62]. Since deposition layers are cyclically reheated, some research aims at fixing the sequences of this process by using adjacent droplets numerical models and to simulate the real physics of welding, which is the metal contact to the base as drops[63] [64] [65]. Additionally, the substrate conducts heat, so the shape and condition of the substrate will have significant effects on the performance of the layers deposited and the resulting surfaces. Any defect in deposition will be magnified during deposition of the subsequent layer[15]. Many studies have focused on the thermally-driven residual stresses and distortions, although geometric simple differences between the simulated and real part does not considered [66].

One study revealed that the last few layers of any AM deposition process have high hardness because they experienced less cyclic reheating[67]. It was determined, the residual stresses effect of the final deposited layer does not exceed five layers. It is proposed that the thermal cycling results in softening and annealing for nearest layers [67] [58]. Thermal recycling is the reason for the high residual stress and deformation in AM [68].

In order to mitigate these undesired outcomes, there are three stages of processing: pre-processing, online processing, and post-processing. The best strategy for reducing the distortion is by using clamping and building strategies, while online strategy (rolling) has a high impact on residual stress.[69] [70] [71] [6] [48].

Some research examined pre-bending as a way to reduce residual stresses and distortions in welding processes[72] as well as to reduce thermal and mechanical tensioning [73] [74] [75] [76]. Optimized deposition sequences are also used to reduced distortion in welding [77] [78] [79] and AM [80] [81] [82] [11]. Others researched have reported achieving zero net distortion by preheating the weld area prior to deposition[83]. Other researchers have reported similarly – preheating the substrate alone reduces distortion in AM processes [84] [85]. Further, heating the substrate prior to deposition decreases residual stresses[11].

Since multi-pass welding is almost identical to WAAM, it is probably acceptable to use mitigation processes from welding in WAAM processes, and reducing the heat input is a significant factor in reducing deformation in multi-pass welding processes[86]. Also, mechanical constraints have the ability to change the final deformation[87] . Moreover, surface quality could be changed by reducing the heat power input or increasing the velocity of the deposition. [13]. Welding processes employ many techniques to control heat input through the introduction of a double heat source (electrode) [88] [89] [90] [91]. Cooling the layers to 50^{O}C after each depositing process significantly reduces residual stresses after the clamps are removed, the cooling process could be better controlled by introducing a waiting time between layer deposition [6].

One of the way to reduce residual stresses online is by using induction heating as a second heat source to follow the deposition process [92]. A high pressure rolling line is also a successful way to reduce residual stresses [10]. Since one of the reason for the residual stresses is the grain structure [12], the rolling enhances grain refinement. Rolling reduces enormously the peak of longitudinal residual stresses [69]. For different metals, path tracks have been studied and the effect of reduction in residual stress and deformation has been demonstrated[81] [93]. It has been reported that one way to reduce residual stresses is through layer deposition in reverse directions, which refers to the high heat diffusion[94] [95] [20]. In order to reduce residual stresses and deformations, one solution is to deposit continuously without any period of cooling time [96], [97]. However, this method leads to high heat input in some locations that induces poor surface quality [98]. It has been shown with different materials that incorporating time delays between layer deposition allows for better cooling of the layers, which reduces distortions and residual stresses[84] [99] [100]. Introducing time delays between layer depositions changes the microstructure significantly [101] [102]. A study showed the effect of controlling temperature through the use of an infrared thermometer on the mechanical properties and surface quality[103]. Other researchers used a passive vision sensor system to control deposition process parameters in order to obtain the desired surface qualities[104] [105]. Others tried to increase GMAW AM accuracy by controlling the deposition process factors in an automated weld-based rapid prototyping (RP) system [106] [107].

In order to improve surface finish, some researchers combine AM processes with traditional milling processes [108]. “Bai et al. (2013) [109]developed electromagnetically confined weld-based additive manufacturing to build overhanging structures or tilt structures at a large slant angle."

Thesis Statement

Residual stresses play a huge role in creating the defects and the distortions that have been observed during the 3-D printing process. It would be very useful if residual stress can be accurately predicted in order to prevent or reduce the effects of these stresses. Since WAAM uses arc welding for printing, it is obvious that simulation software for welding processes could accurately simulate WAAM. Lehigh has made many samples using an experimental WAAM machine, so in this research, one model will be studied and simulated using SYSWELD; the goal is to observe the residual stress and the distortion of 3D printed plates by using simulation software (SYSWELD). The materials used in this research are: 1) austenitic stainless steel 316L and, 2) low alloy carbon steel S355J2G3.

Chapter 2 Simulation setup

Experiment

Lehigh has made many 3D printing samples of WAAM using the machine which was previously described, one of them was done by Prof. Haden, Gordon and their group. Gordon has made and tested a 3D printed 304 stainless steel plates for Fatigue crack growth and Microstructural characterization. Also, he repeated the tests after heat treatment. For fatigue test, he took samples from horizontal and vertical orientation[110]. As shown in the picture below Figure 2.1, this is the 3D printed part of the sample using welding process as WAAM. Also, it is clear the distortion of the base metal is due to the stress of the printed part.

Figure 2.1 : The experiment sample after it cooled

Additionally, some milling and cutting are done on 3D printed part to get the fine area. Figure2.2 shows the length with both sides; from this figure, it is clear the distortion of the base plate released some of the residual stress after it was cut from the substrate. Figure 2.3 shows the two ends of the printed part, they are cut from the original part because they have higher rate of distortion as appear

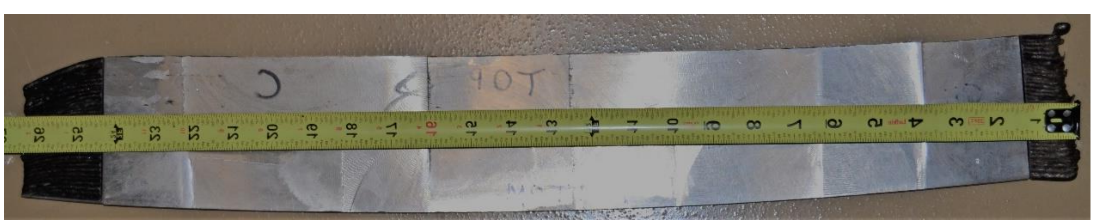

Figure 2.2 : The experiment sample after machining

Figure 2.3 : Two ends of the real sample (start welding, right) (end welding, left)

This sample was printed with the welding parameters, as shown below in Table 2.1

Table 2.1 welding parameters for AM in Lehigh Lab

Wire feed rate	voltage	Substrate Type	welding speed	Wire Type	Shielding Gas
9.3 mm/s	22V	Stainless Steel Grade 304	2.54 mm/s	ER308L	90% He, 7.5% Ar, 2.5% C02

Number of layers	Layer length	Layer Height	Layer Thickness	Substrate Dimension
38 Layers	670 mm	1.778 mm	6.35 mm	5 X 101 X 762 mm

Figure 2.4 shows the cross section of the beginning cut. It is clear **from the figure** the cutting process does not leave any impression of layers on the cross section of the sample. The height of the sample is around 95 mm. and the width around 0.39 inch = 9.9mm (which are the extreme parameters of the sample).

Figure 2.4 : Dimensions of the cross section (height on left and width on right)

Since the goal is to perform a welding simulation process, it is important to observe the shape of each layer by conducting electric etching process. Before drawing the shape of layers into the simulation software, the part of interest needs to be suitable for photographing by cutting the appropriate part, as seen in Figure 2.5 with red lines. After the cutting process and before the etching process, it needs to be mounted, grinded and polished.

*Figure 2.5 : Section of the intent cut for **displaying** the microstructure*

Figure2.6 shows the cut piece after conducting the electric etching process, electric etching process demands to put the piece inside an acid and contact the ends of the piece by an electric circuit, and the original one, which is done for make the microstructure features clearer. The left side of Figure 2.6 shows the mounted pieces cut in half to fit into the mold.

Figure 2.6 : The cut pieces with the left original piece

Checking the dimensions again for the etched parts Figure 2.7.

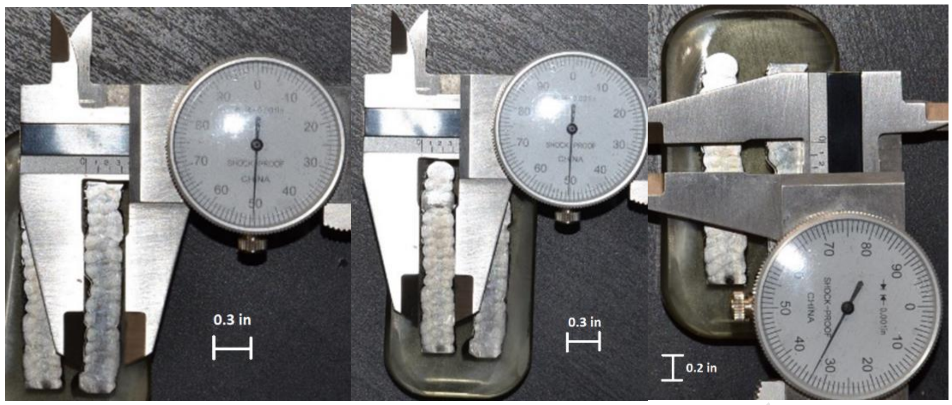

Figure 2.7 : Three pictures showing the dimensions of the printed layer.

Figure 2.8 shows the cut piece (cross section cut) under two different light degrees for showing some features for the layers. These pictures have been taken by using a canon camera 600d.

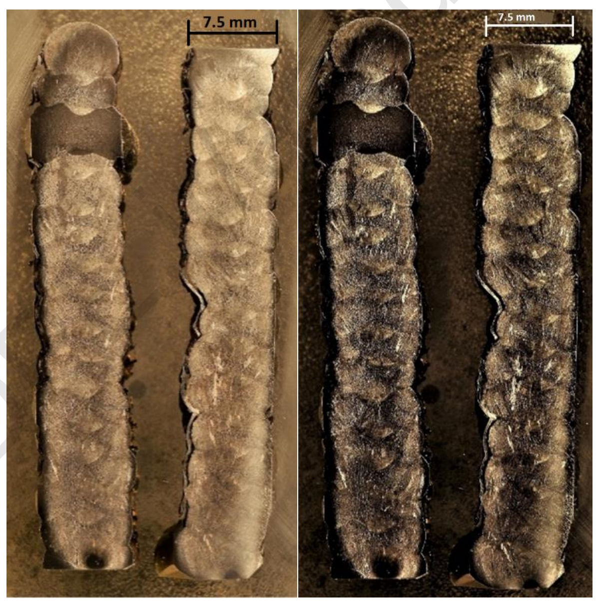

Figure 2.8 : Two different colored images for the microstructure printed part

Mathematical Molding

For heat input

$$Heat\ Input = \frac{V\ I}{S}\eta \qquad Watts * \frac{s}{mm} * \ Joule/s$$

$$V = Electric\ Voltage\ (Volt)$$

$$I = Electric\ Current\ \ (Amp)$$

$$S = Torch\ Velocity\ (mm/s)$$

$$\eta = efficiency$$

For this sample, the voltage used was 20V, and the current varied depending on the process of welding (average currents are around 77 Amp). The torch velocity was 2.54 mm/s. If we consider the efficiency of the welding heat input to be 0.8, the heat input required for the simulation processes was found to be around 480 Joule/s. By using Smart Weld, Smart Weld is a software was created based on a scientific data in order to help engineers to determine the welding parameters before starting the actual processes, we can get the shape and the dimension of the penetration area. Figure 2.9 shows the result for the given parameters (speed, depth and type of metal) then Smart Weld has been developed depending on experiment test. Smart Weld gives the input power as 1231 Watts (which is voltage multiplied by the current and efficiency of the processes). After dividing it by the speed, it gives 473 Joule/s, which is almost as the same as the calculated power.

Figure 2.9 : Smart Weld screenshot shows the parameters of the welding processes

Simulation

In order to know the mechanical properties for this sample or a portion of it, it is efficient to use some of the capable software: one of them is SYSWELD. In this case, the sample has been developed using approximate dimensions to make the processes easy. By using SYSWELD, the simulate design has been made According to the real design (as shown in Figure 2.10) and by using the following dimensions: length, width, and height. In Figure 2.10 the red rectangles represent rigid clamps, which prevent the sample from moving in the Z-axis direction.

X = 800 mm for substrate, 700 mm for the welding passes, and the longest distance is 800 mm

Y = 100 mm for substrate, 10 mm for the welding passes, and the longest distance is 100 mm

Z = 5 mm for substrate, 85 mm for the welding passes, and the longest distance is 90 mm

For a single bead, length is 700 mm, width is 10 mm, and height is 2mm

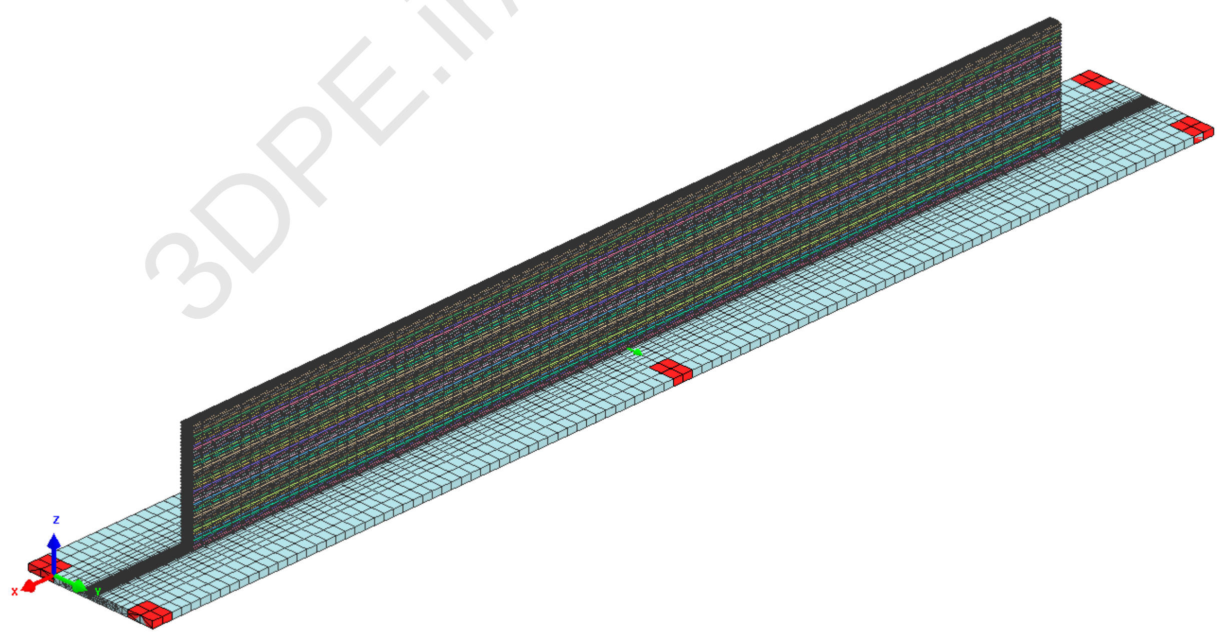

Figure 2.10 : The simulated sample constructed using SYSWELD

Figure 2.11 compares the actual measured cross-sectional area with the cross sectional area used in the finite element simulation.

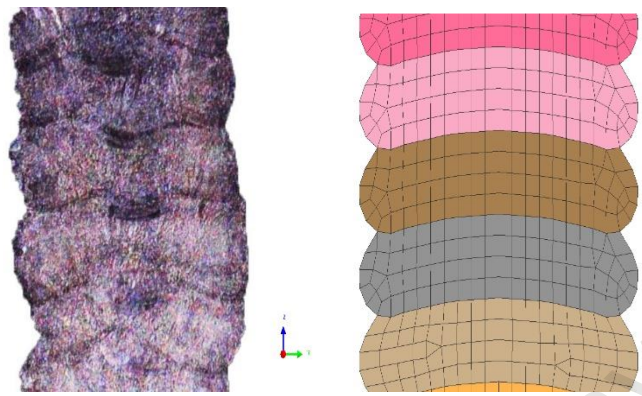

Figure 2.11 : Comparison between the shape of layers (real, left; simulated, right)

Before proceeding with the main model calculation, the simulation process needed some tests to validate the model setup – These tests are as follows: Heat test, Path test, Mesh test, Penetration test, and Clamping test – The purpose of the Heat test was to observe the behavior of temperature around the test model. As the full computational process took considerable time, it was effective to decrease the time by one half by taking advantage of symmetry. The heat behavior looked symmetric around the path of the power source. So, the test may have decreased the time to half of the original time. Furthermore, the Heat test could show the temperature behavior for each layer; so, nodes were chosen on top of layers for showing their behavior.. The Path test was used for showing the effect of the deposition direction during the process. The third test was the Mesh refinement test: the test displayed the effect of the number of elements (mesh) on the result. From the result, the number of elements were chosen in accordance with reasonable match on the result. The fourth test was the Penetration test: in this test, the melting pool dimensions were found to be different in three cases. This had been done because SYSWELD gives the choice to setup the dimensions of the penetration size; also, the arc welding processes have different arc shapes depending on the welding parameters, which effected the melt pool size and shape. So, the purpose was to look at the heat effects of the different penetration dimensions on the layers. Ideally, the shape of the melted layers had to be as close as possible to the final layer shapes observed in the actual welding process – as shown in Figure 2.11. The real sample had the fluid effect on the melting part. So, the purpose of the penetration test was to look at the shape of the melting pool during computational process and to try to simulate as same as possible of the actual shape. The Clamping test was the last test: this test was conducted to test the computational process on two models. One was half the other model, the half is on X-axis that makes positive Y-axis is symmetric of negative Y-axis. Since the mechanical properties were symmetric around the X-axis and Y-axis, they may be used in saving time to compute the half model instead of the whole model. So, several conditions were established to get the matched results between the two models. In summary, integrating these tests allowed the main model to give the most accurate results possible for the existing conditions.

Heat test

Before the simulated real sample was processed, simulation processes needed to be tested for validating its reality. In addition, for that, it was great to have a coherent picture about the running processes of SYSWELD. The first test was the heat distribution test between two samples (seen in Figure 2.13) that were made from the main sample on Figure 2.12. So, the test was conducted using a base metal with 3 layers in the middle. The first run was made for the whole sample and the second run was made by a half of the complete sample was created by a symmetric plane of the sample into the middle of Y-axis, which left one part of the positive Y-axis and decreased the power into half as shown on Figure 2.12.

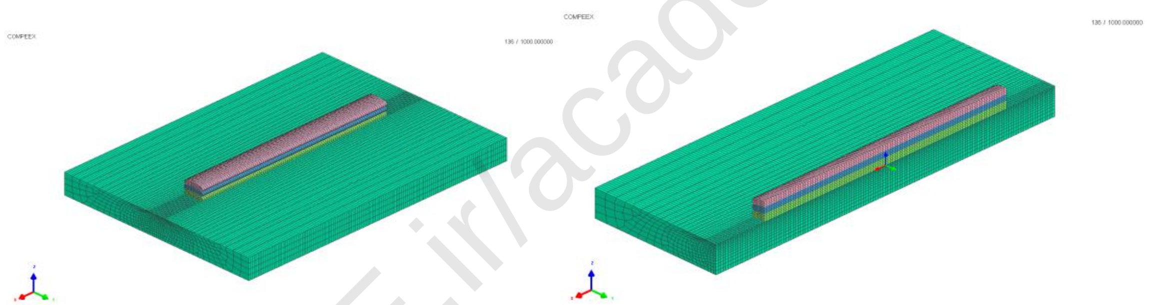

Figure 2.12 : The main (complete) sample on left, and the half sample on right

After running the two tests, cross section was made into the middle of X-axis to show the temperature distribution.

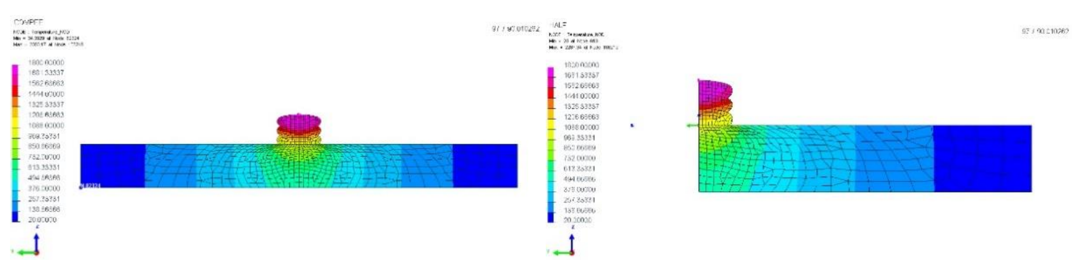

Figure 2.13 : Test result for the complete sample on the left and the half sample on the right

So, the main point was that heat was equally distributed and symmetric around the weld line, as shown in Figure 2.13 and Figure 2.14, and showed the cross-section on Y-axis for the whole sample and the half-running sample. It was clear from these two figures that the heat distributed was similar between the running tests, which gave the opportunity to run the samples faster because of the smaller sample size; besides, the result was found to be the same in both cases.

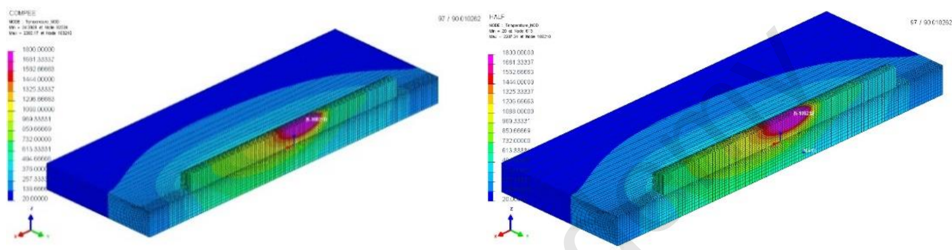

Figure 2.14 : Temperature distribution contours for two samples (complete, left; half, right)

The second Heat test was on the seven layers for half sample since the result was concluded and reasonable for the half sample. The sample geometry is shown on Figure 2.15; the cross section of the right side of the sample was insulated for the heat transfer in such a way that the boundaries looked like a complete sample.

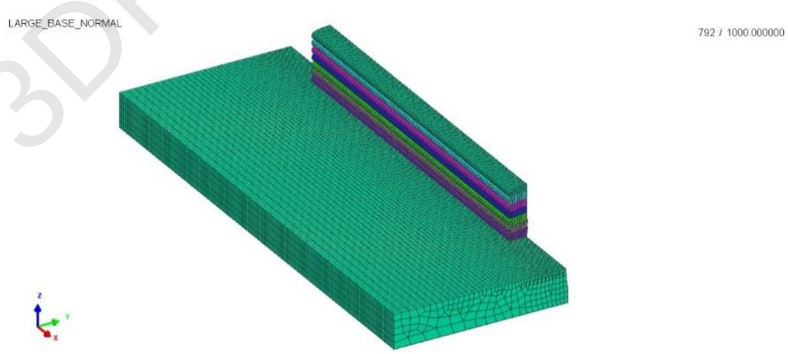

Figure 2.15 : The used half sample in the next tests

For understanding the temperature behavior, seven nodes were selected in the beginning – for each pass (layer) –on the meeting point between the heat source and melting metal. In the first attempt, the heat was found to be constant for each layer, which meant that it remained 240 Joules/s; the original power was found to be 480 Watts after the efficiency was calculated, and 240 Watts after it decreased to half, since the used geometry is half of the main geometry (with 480 Watts). Figure 2.16 shows temperature profiles for the seven passes. It is clear here that the peak temperature increased as the next layer started to build. The difference between the highest and the lowest temperature was around 600° Celsius, which was huge for a metal with a melting point of 1400 ° Celsius: This made the previous layer melt completely.

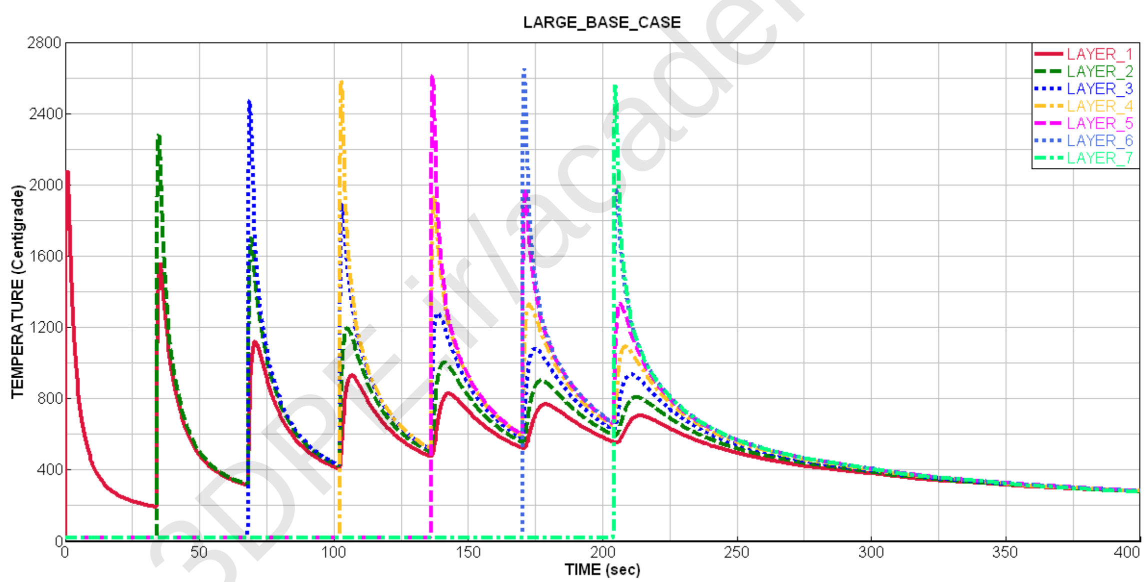

Figure 2.16 : Temperature profiles for heat constant and series deposition timing

So, in order to decrease that big difference, two different techniques had been used. The first trick was to cool down the sample with time gaps between the deposition of the layers, and the second one was decreasing the power for some simple relation rule. Figure 2.17 shows the temperature profiles for the time gaps case. From the curves, the difference between the highest and the lowest peak temperature was found to be around 200 ° Celsius. This was a great technique to reduce the peak temperature, but it needed long time to build the whole sample.

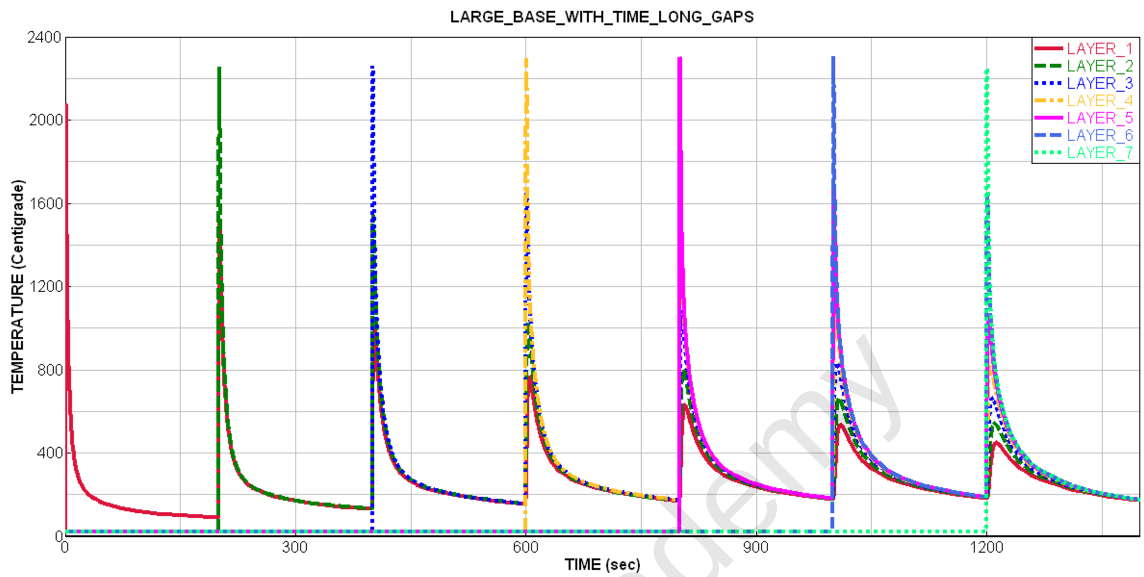

Figure 2.17 : Temperature behavior for the seven layers with time gaps between them

The second technique was to use the law

$$NP\ \ layer_{n+1} \approx OP\ layer_n \frac{OT\ \ layer_n}{OT\ \ layer_{n+1}}$$

$$NP = new\ power\ rate\ for\ the\ desired\ layer\ (n+1)$$

$$OP = old\ power\ of\ the\ last\ layer(n) before\ the\ deisred\ one(n+1)$$

$$OT = old\ peak\ Temp. for\ layer\ (n)\ or\ the\ melting\ temp. for\ the\ metal$$

By using this approximated relation, the new power rate was found as: 333, 304, 279, 268, 268, 263, 274 Joule/s, with η=0.8, from layers 1 to 7 respectively. So, the result was as expected (shown in Figure 2.18). The difference between the highest and the lowest peak temperatures had decreased, and the peak temperature also decreased for each pass after another, which made this way appropriate for saving time with suitable heat input.

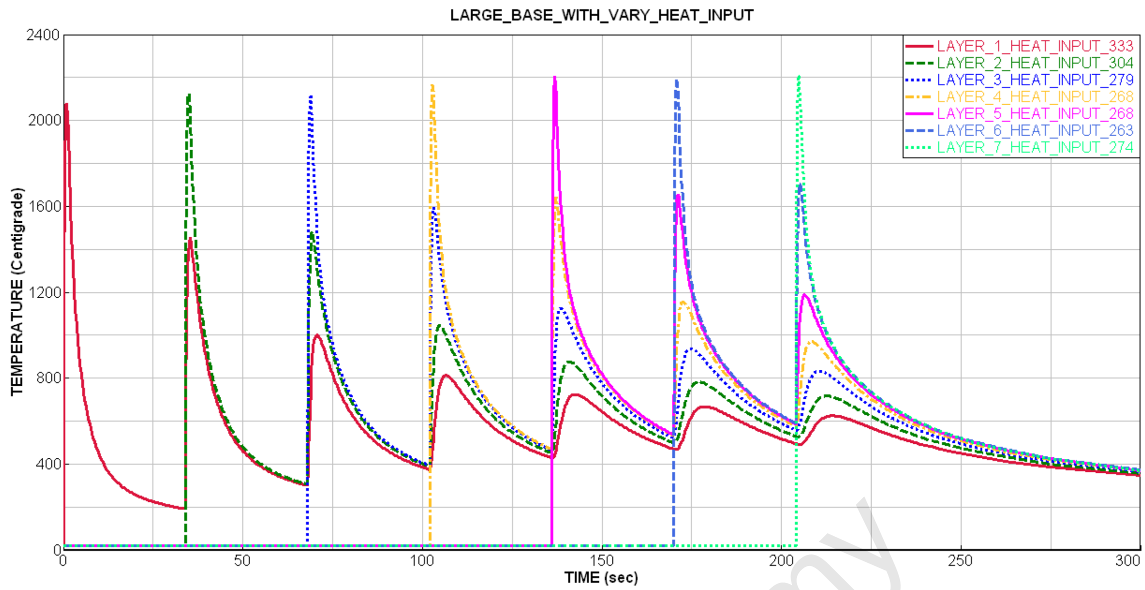

Figure 2.18 : Temperature behaviors for the seven layers with new proposed heat input

Another way of controlling the peak temperature was by decreasing the heat sink or the big consumption, which in our case was the substrate. So, the base metal had been designed to fit the width of layers and the longer length as shown in Figure 2.19. Temperature profiles (shown in Figure 2.20) showed quite a change in the difference between the highest and the lowest temperatures as 650° Celsius, but it was not that efficient for heat transfer.

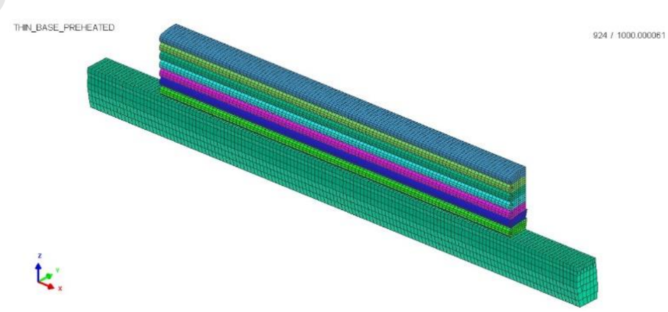

Figure 2.19 : The used half sample in the next test with a small base

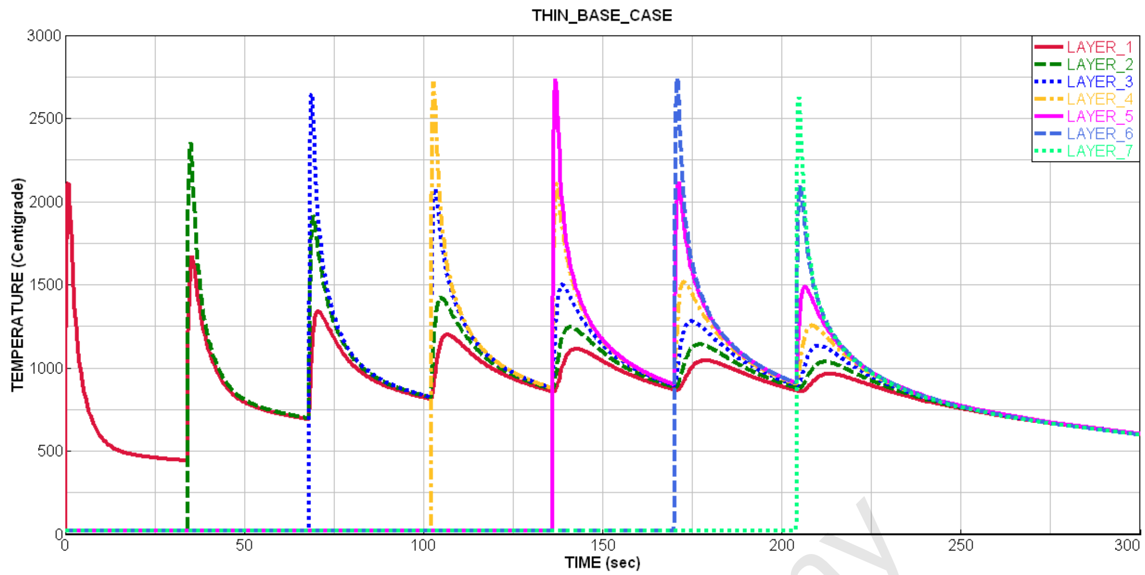

Figure 2.20 : Temperature behaviors for the seven layers with small bases

Another trick was preheating the substrate for a certain temperature to equalize the temperature between the base and the layers. It showed a lower difference than the last trick, but it had a disadvantage: it needed to modify the power to lower rates, since the base was already heated up. The result is shown in Figure 2.21

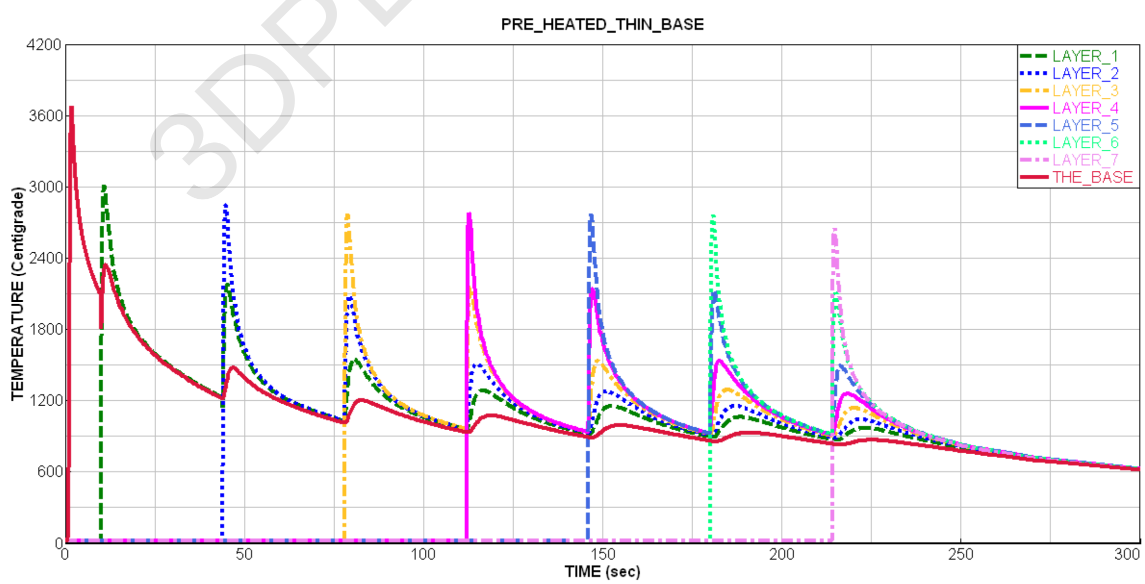

Figure 2.21 : Temperature behaviors for the seven layers after the base was heated up

Path test

One of the parameters for manufacturing by AM processes is the deposition path. As, common welding machines use a single torch, so for printing a plate requires two schemes paths. The first path was to start from one side and stop at the other, then return to the beginning to build the next layer. This is forward deposition. The second path was to start at the beginning and not stop at the second side; instead, continue to build the second layer from the other side, to the end, and back forward, as shown in the figure below Figure 2.22.

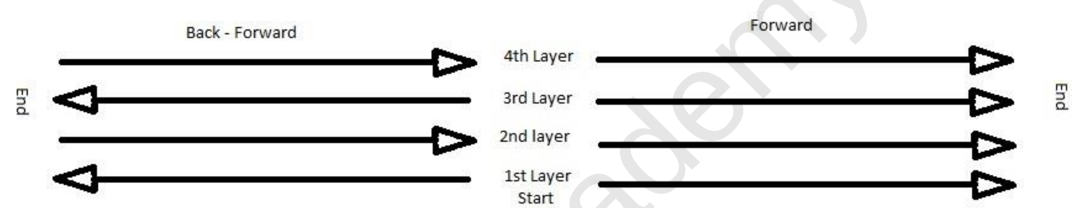

Figure 2.22 : The schemes description for forward path and back forward

So, for this case, the samples had five layers each and they underwent thermal and mechanical tests. For the heat distribution overall, both the ways had diffused the same amount of heat on the samples; cross section in the middle of the samples shows the identical temperature contours, as seen in Figure 2.23.

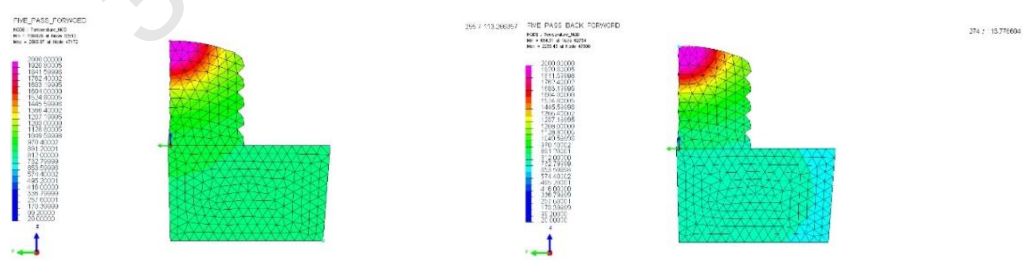

Figure 2.23 : Temperature contours for forward path (left) and back forward (right)

Also, the temperature profiles for certain nodes correlated to the heat input paths. These nodes have the same locations on both samples, the nodes located on the top of each start for each layer on forward path; so, they have the same Y and X coordinates, but changing Z coordinates. For the forward path, the result was same as that observed in the Heat test (see Figure 2.24). But, the more interesting is the back forward path, as seen in Figure 2.25 the layers had higher temperature than that's in the forward path. In both paths, the peak temperature was found to be around 2500 ° Celsius; but, forward path took five layers to reach it, while back forward path took two layers. So, that gave an idea about the heat around the ends, which was hotter on the end for forward and have the same for the both ends in back forward. For the timing condition, the deposition did not stop at any point between the start and end, which meant there was no time for cooling down the whole sample. The figure below for forward deposition path shows how the peak temperature increased by 500 ° Celsius between the first and the last layer, and by almost +100 ° Celsius for each layer.

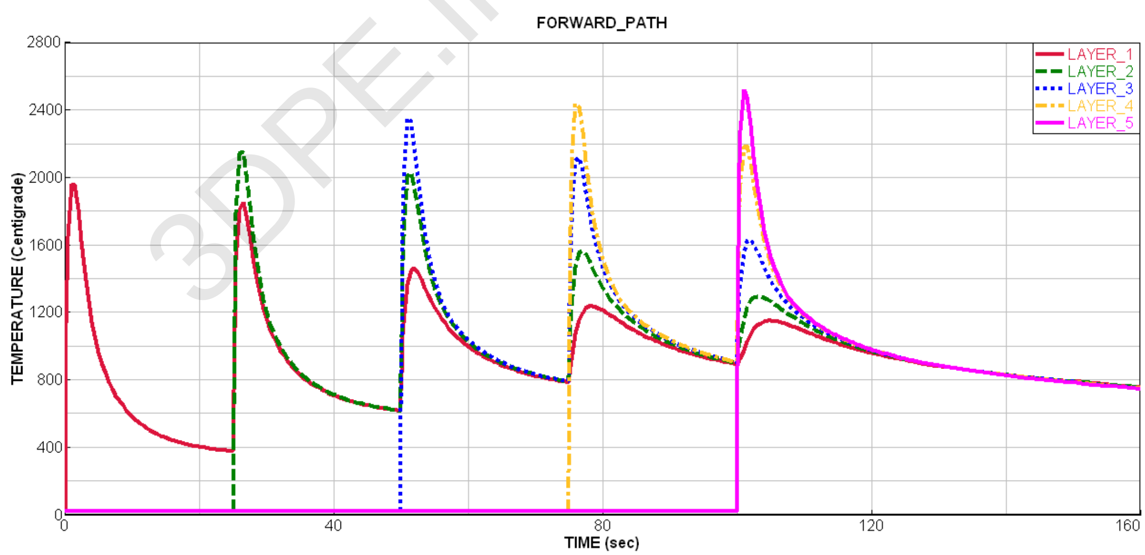

Figure 2.24 : Temperature profiles for forward path deposition

From the figure shown below the back forward deposition path – it was clear there was a high difference between the first node and the second. But, it also had a disadvantage: early deposition. SYSWELD needed to identify each filler material for each welded path. The filling materials were deposited part, not as continues deposition processes, and that can be observed by the temperature increase for the second node (second layer-green curve) at a time of 25 seconds. The node was deposited but not applied to the heat; instead, it was affected by the last layer temperature. So, it worked as a small heat sink for the previous layers. It could be considered as the preheat process, but the difference between preheating and this case was small in terms of the peak temperature, the region would melt, and the properties would be constructed again.

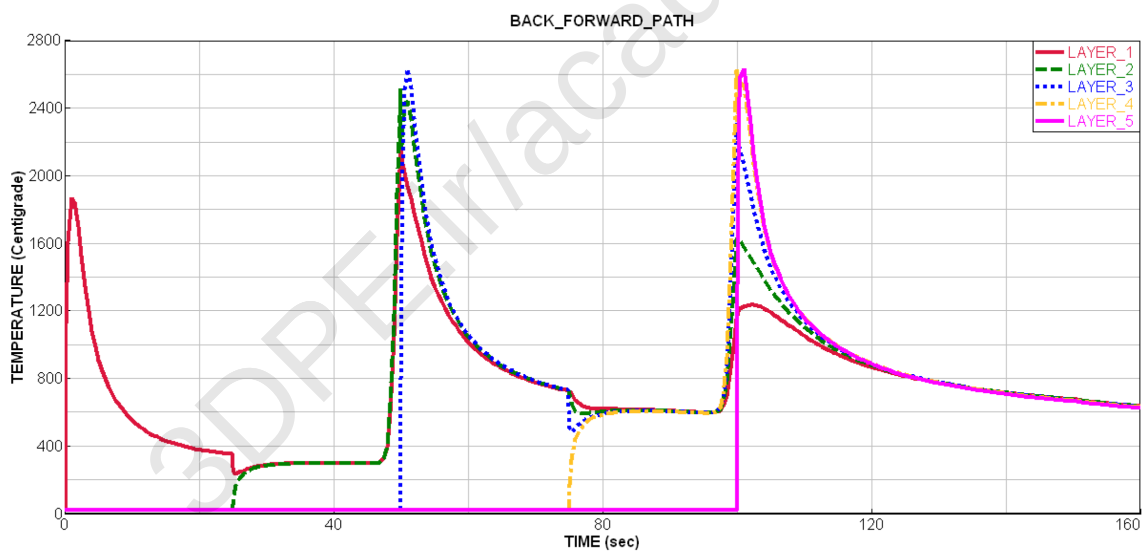

Figure 2.25 : Temperature profiles for back forward path deposition

Both paths have surface tension effects on the ends. Figure 2.26 shows the deformation caused by the heat on the end of forward path and the start has less deformation. The start also has lesser deformation than the middle. These were also comparisons made between the experiment of the actual sample and the simulated one.

[43]

Figure 2.26 : Distortion after printing (real, bottom; simulated, top) for forward path

Figure 2.27 shows the deformed ends for both back forward path and the actual sample. In contrast to the forward path, both endings have been deformed by the heat input, since the peak temperature occurred at the ends, as described on the temperature profiles in Figure 2.25

[43]

Figure 2.27 : Distortion after printing (real, bottom; simulate, top) for back forward path

These two techniques deform the ending in non-useful way, so it made the endings as non-active area. Figure 2.28 shows 3D contours for the σ_{XX} residual stress for the working pieces. Parts A and B show the outer part: they were almost equal in terms of stress. But, Parts C and D show the inside of the pieces, which were insulated thermally with some difference between these paths. The red region is tension (positive stress) and the blue region is compression (negative stress). Parts E and F show the clear difference between these paths by these cross-section contours. At the least, the similarity between them were the regions remaining in their position of comparison or tension but with difference in the values. In conclusion, these two paths had almost the same properties with trivial difference in the middle area, while the ends had the noticeable deformation difference.

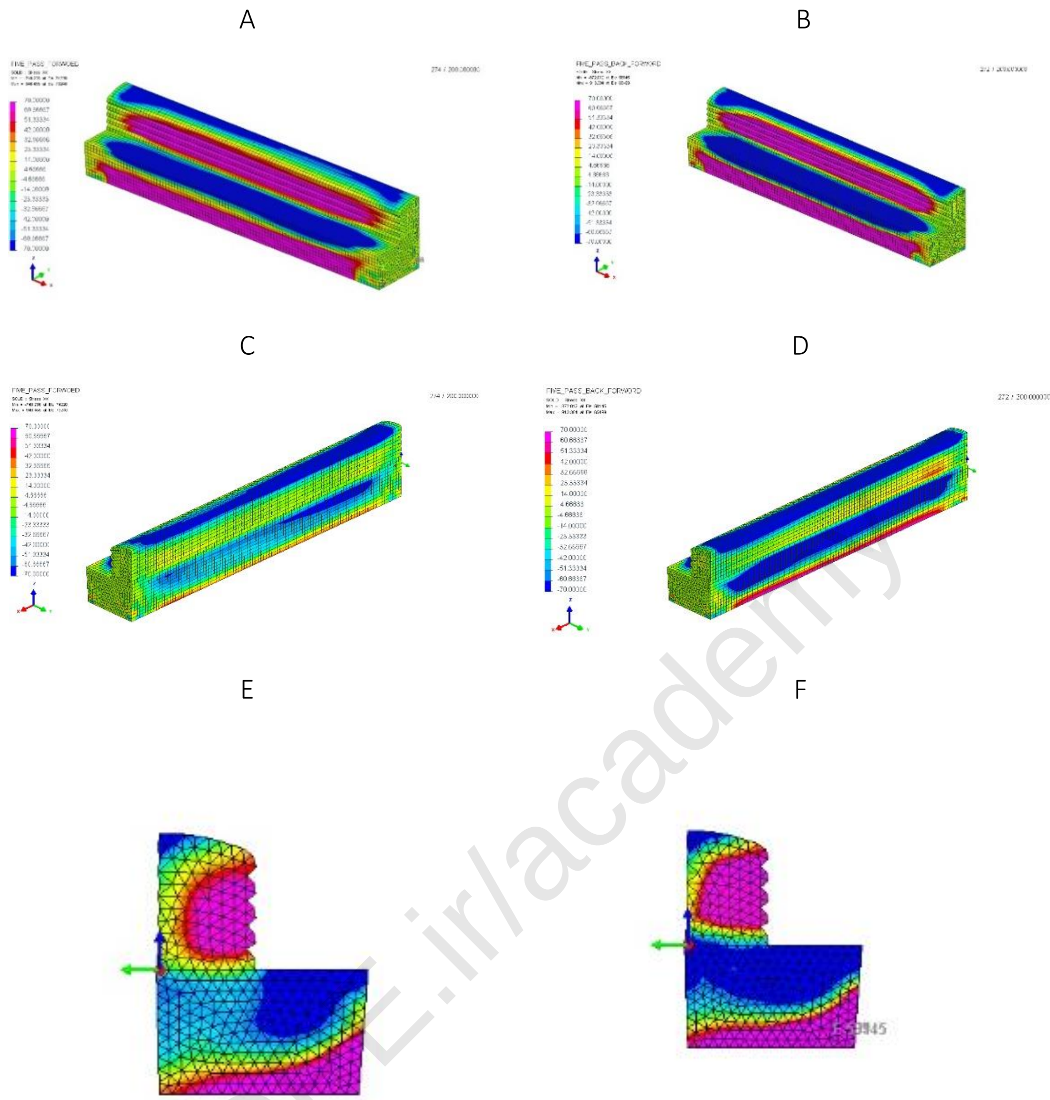

Figure 2.28 : Stress σ_{XX} contours for forward (left) and back forward (right)

Mesh test

Mesh test was important for result reliance; so, a single weld bead was tested thermally and mechanically. Also, the number of elements for the same sample was doubled: the less mesh sample had 7400 elements and the other sample had 14800 elements for the same dimensions. In Figure 2.29, the temperature disruptions were identical for both the samples at the same time (at 21 seconds). This made use of the less mesh sample more useful than the higher one in terms of thermal changes, because it needed lower time as well.

A B

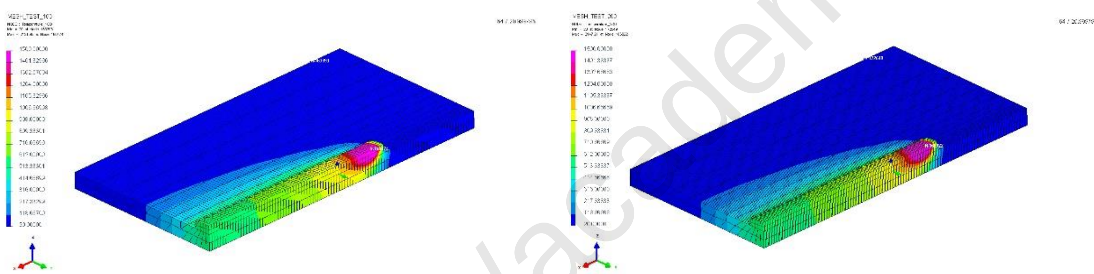

Figure 2.29 : Thermal contours for 7400 elements (left) and for 14800 elements (right)

The second aspect was the mechanical contours, as shown in Figure 2.30, for σ_{XX} residual stress. Similar to the thermal aspect, the contours looked identical in both mesh tests for 7400 and 14800 elements. So, that gave the less mesh elements the preference for time saving in the computational processes.

A B

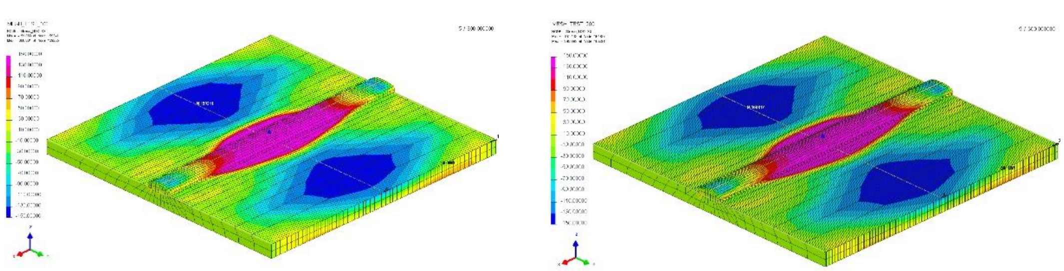

Figure 2.30 : σ_{XX} stress contours for 7400 elements (left) and for 14800 elements (right)

Moreover, for accuracy purposes, curves show a clearer picture of the relation between these two tests. Six node lines had been selected on the same position for both sample tests: three along X-axis (left, right, and wire) and three along Y-axis (front, rear, and middle), as seen in Figure 2.31.

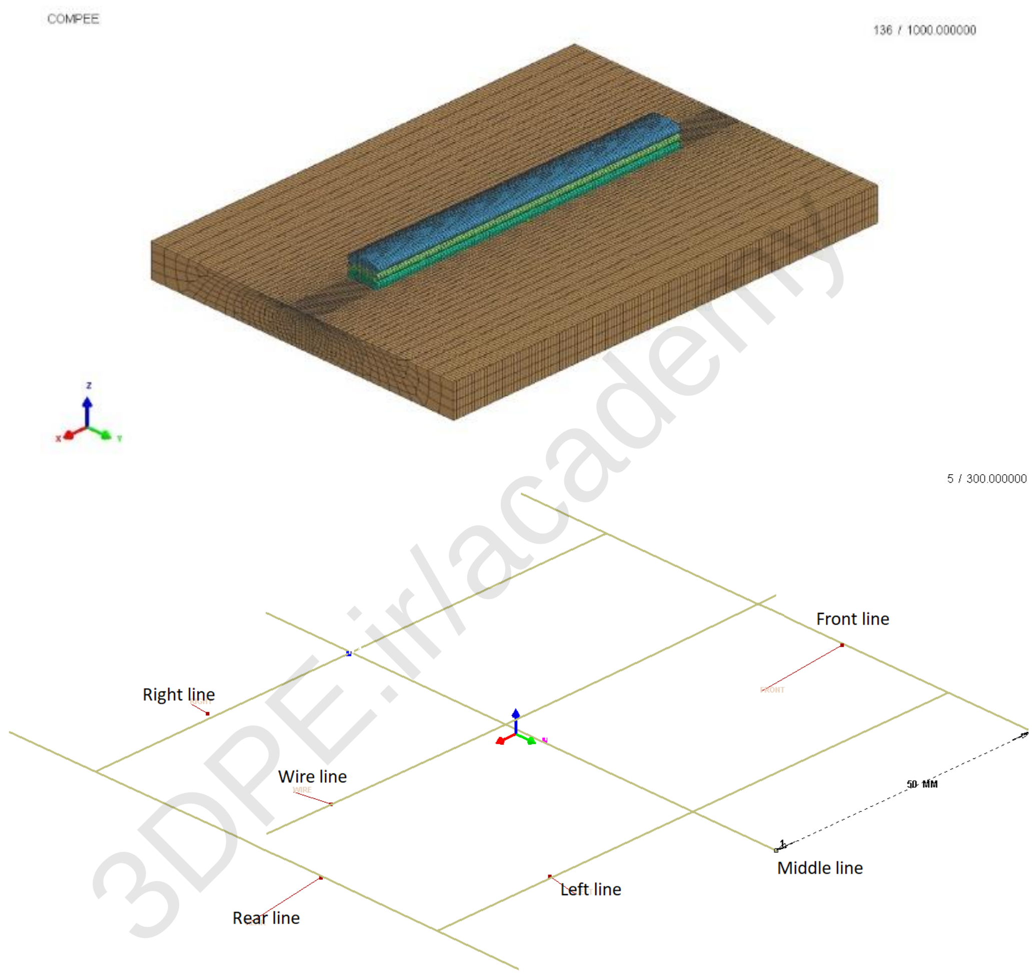

Figure 2.31 : Six lines on the work pieces for testing the mesh

Figure 2.32 shows σ_{XX} residual stress for the middle line. The profiles take the expected curves from welding process for single bead. At the center is the highest value, while it decreases from the center. The aim was to look at the similarity in the curves for 7400 and 14800 elements mesh tests. And, the highest difference between these two curves was found to be almost less than 0.01%, which made it easier to trust the less mesh sample for certain level of accuracy.

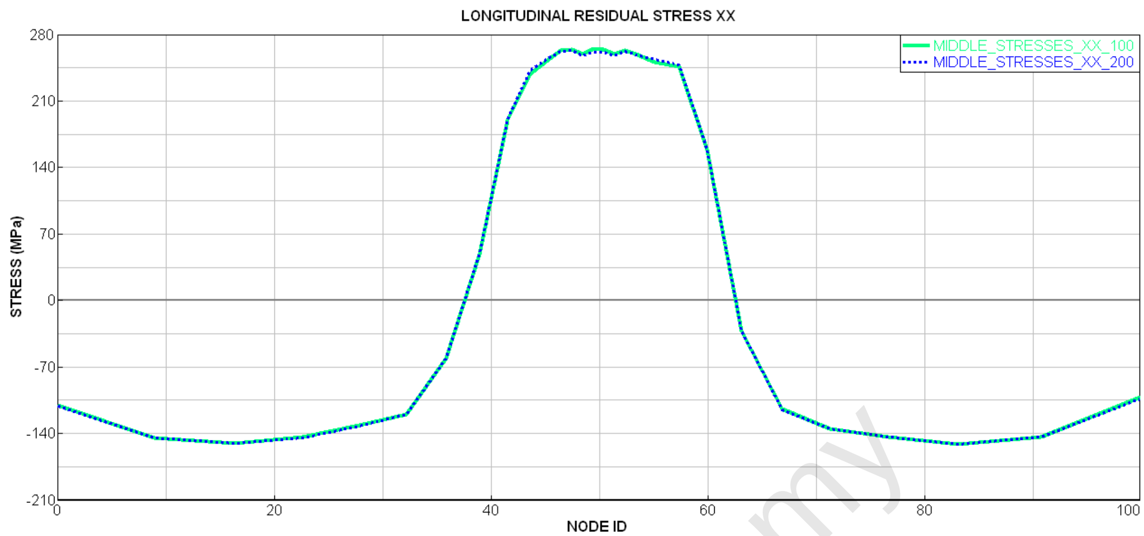

Figure 2.32 : σ_{XX} residual stress for the middle profiles in both the cases (7400 and 14800)

The second two test lines were placed on the wire for self-welding Figure 2.33. For the same curves, the σ_{YY} residual stress behavior was reasonable as the expected stress for welding single pass, and the same for both cases with the error less than 1% in certain areas.

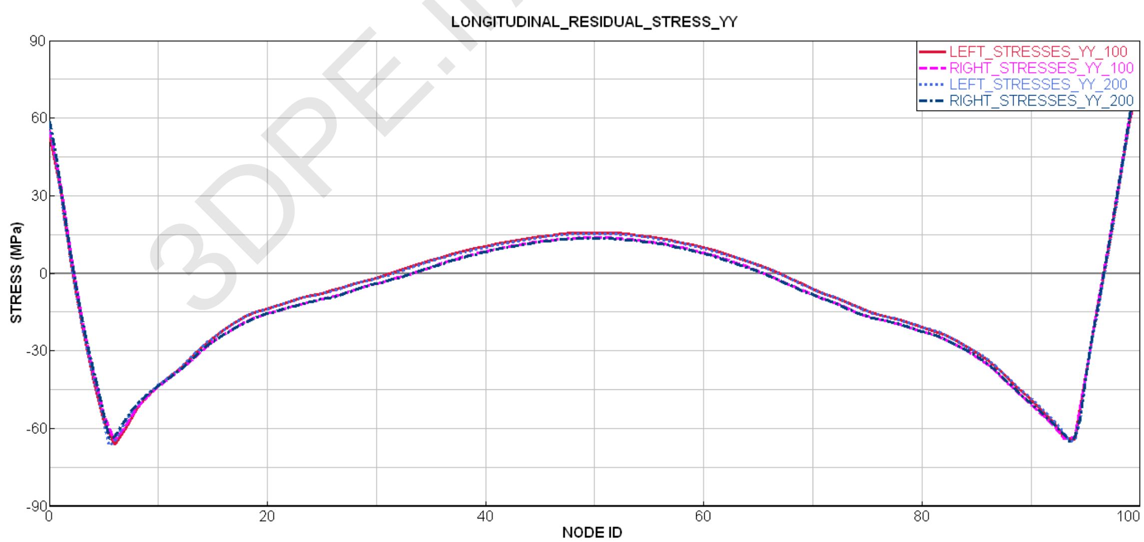

Figure 2.33 : σ_{YY} residual stress for the wire profiles in both the cases (7400 and 14800)

By looking at the σ_{XX} residual stress contours above in Figure2.30, both the left and right sides have the same behavior in terms of stress. Figure 2.34 shows the σ_{XX} residual stress for four lines, taken from two positions of the two samples: left and right line for samples with 7400 elements and left and right line for samples with 14800 elements. Thus, the four lines have the same behavior.

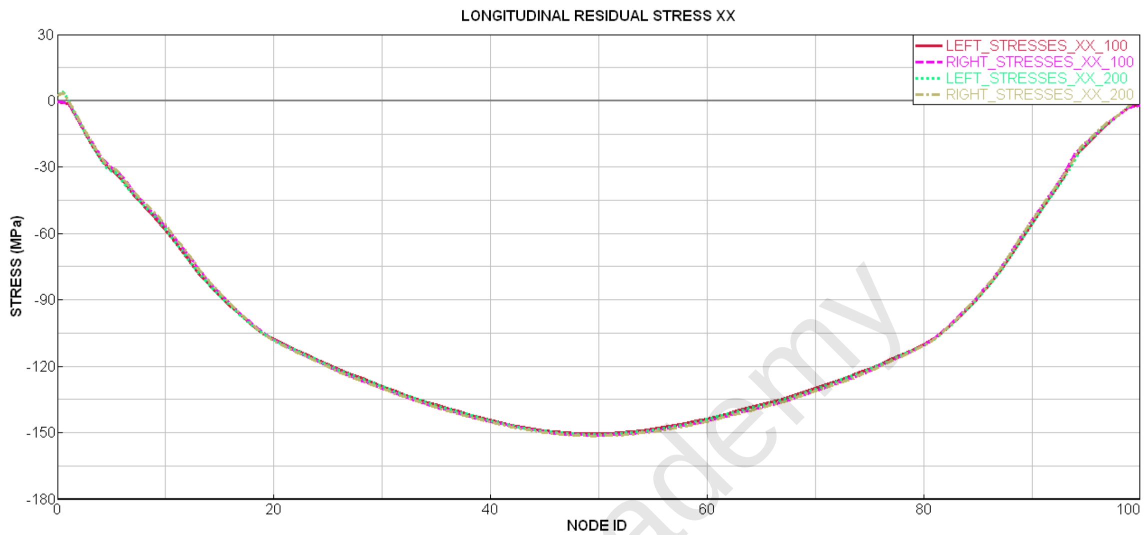

Figure 2.34 : σ_{XX} residual stress for the right and left profiles in both the cases (7400 and 14800)

In addition, these four lines, shown in Figure 2.31, were tests for σ_{XX} residual stress. To make sure even the other mechanical aspects had the same similarities, these four lines tested with σ_{XX} residual stress. For the same result Figure 2.35, the four lines had the same curvature for left and right lines in both the cases.

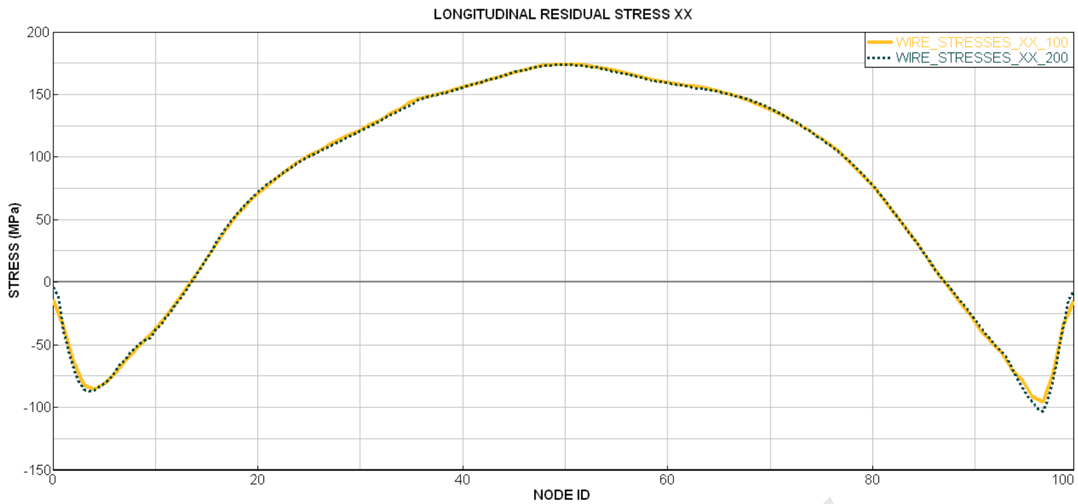

Figure 2.35 : σ_{XX} residual stress for the right and left profiles in both the cases (7400 and14800)

So, for all the previous lines the mesh size does not make difference to the importance of the mesh size; but, for front and rear lines from the samples they were found to be different. Figure 2.36 shows many unfitting areas for both cases: for the front lines, in the middle the behavior (sign) were the same. But, at the ends, the values did not follow at all.

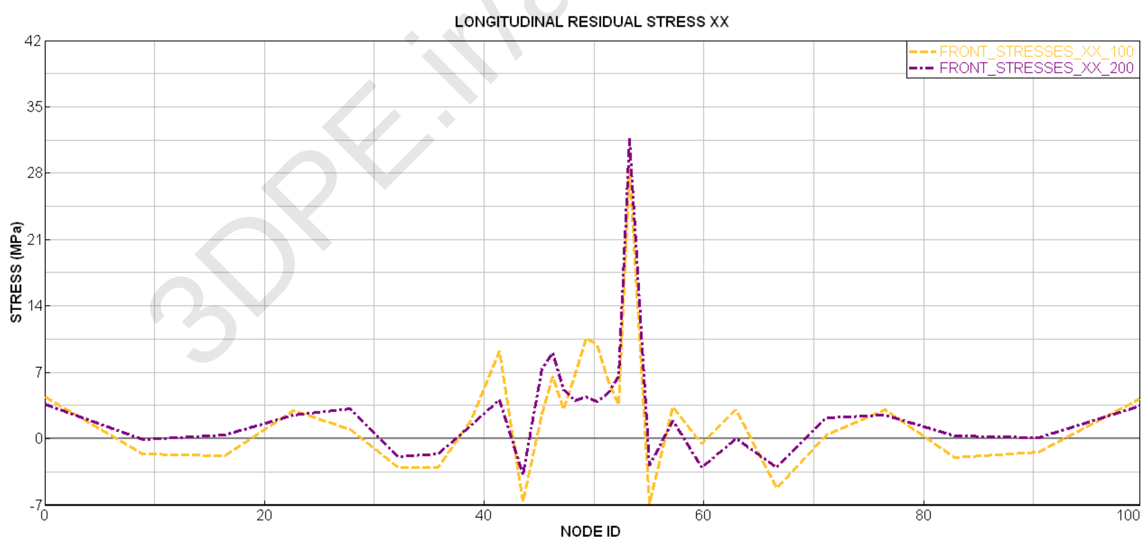

Figure 2.36 σ_{XX} residual stress for the front profiles in both cases (7400 and 14800)

Also Figure 2.37 shows rear lines σ_{XX} residual stress. These curves, as seen in B part of the figure, do not fit in most of the profiles, except in the middle, which is has the same sign, but different values. And by looking to the original mesh in Figure 2.30, it was noticeable that the size of elements got bigger at the ends, unlikely to the middle. As a conclusion, the size of the elements was important to a certain level, and t no matter the size, the result would be identical. Also, for the least affected areas from the heat, the results were not accurate. For research purposes, AM simulation needed smaller mesh size on the active and interest area, at least a couple of millimeters for an edge.

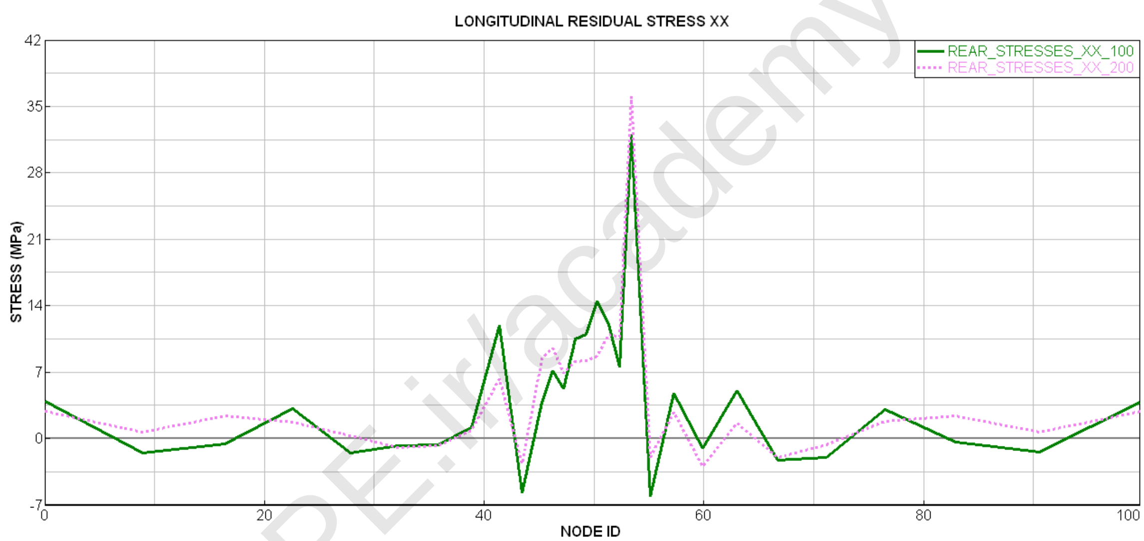

Figure 2.37 σ_{XX} residual stress for the rear profiles in both the cases (7400 and 14800)

Penetration test

For the simulation processes, the parameters of the melting pool and power parameters had been grabbed from Smart Weld. But, SYSWELD had the opportunity to fix the melting pool shape. AM needed that because the layer was not shaped as the regular melting pool in any welding processes. So, in order to look at the effects of these estimated dimensions for the melting pool on SYSWELD, three shapes were tested. The shape parameter is described in Figure 2.38 for the melting pool, and in Figure 2.39 A, the three-dimension parameters are shown as regular and large regular. The last shape was created to fit the layer (proposed) for all these shapes: the depth (penetration) was constant and the parameters were the width and the length. Figure 2.39 B, C, and D are the side views for the three shapes (back, left, and right).

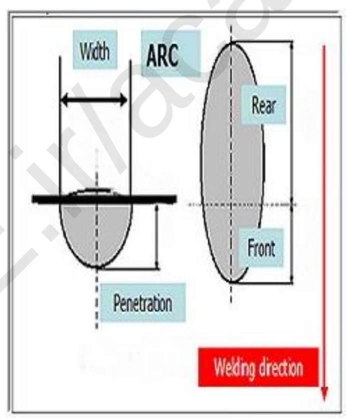

Figure 2.38 : The estimated dimension for the arc of welding from SYSWELD

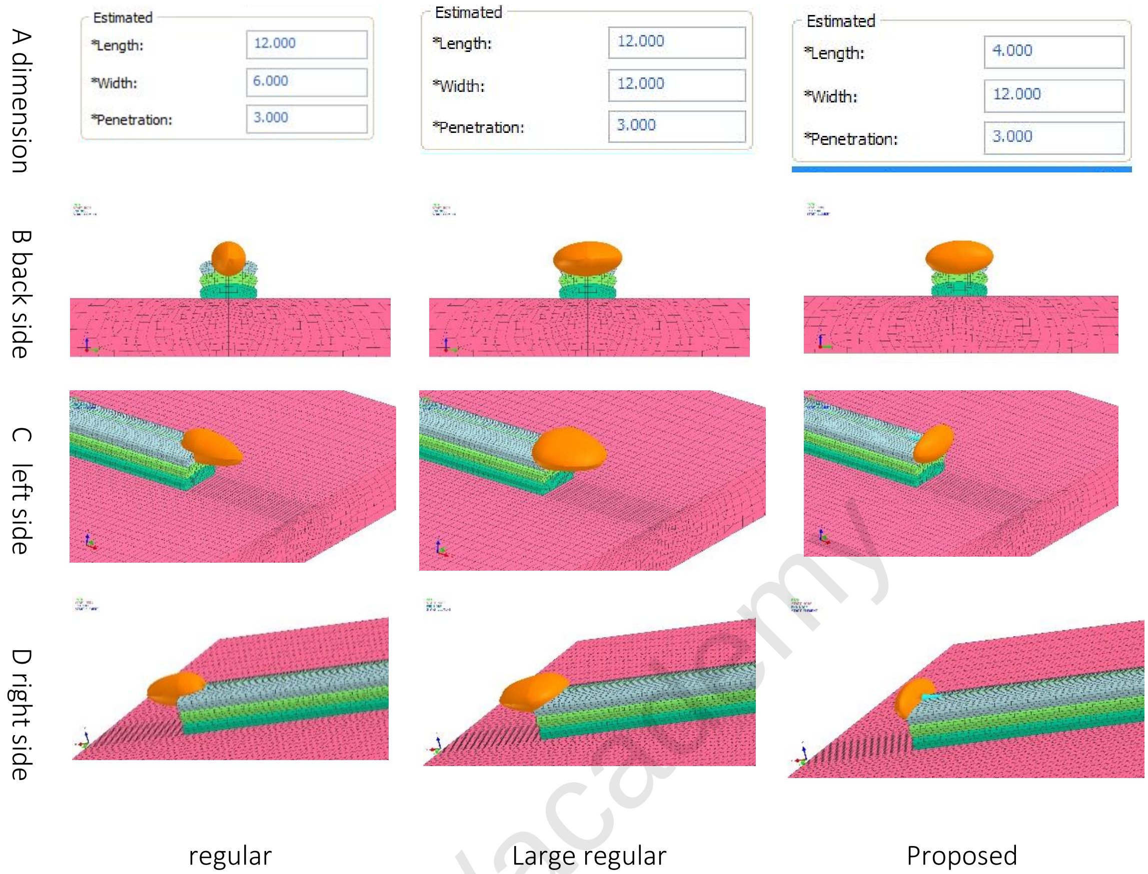

Figure 2.39 : The shape of the estimated arc of the welding

Therefore, the best way to judge was to draw the thermal contours at the 21st second. These images had been captured for the processes of the deposition of a third layer with different shapes for the estimated melting pool with same temperature color bar scale. Figure 2.40 A shows the right side for the melting pool, and it seemed the shapes were similar for the highest temperature and the heat regions. Figure 2.40 B shows slight difference on the front regions. The proposed shape received more sudden heat than other. Figure 2.40 C shows the cross section of the middle of the samples with the same estimated penetration depth. But, the simulated shapes were different among these three. On the large regular and the proposed shapes, the re-melting areas were bigger than the regular shape; besides that, all the top surfaces of the previous layer were re-melting, which was not the case. Figure 2.11 shows that the re-melting area is in the middle of the previous layer surface, and Figure 2.40 C (regular) shows the simulated re-melting similar area to the actual one. As a conclusion, the more realistic melting pool for the simulated process was the regular even if the shape of the welding bead was different from the regular welding processes.

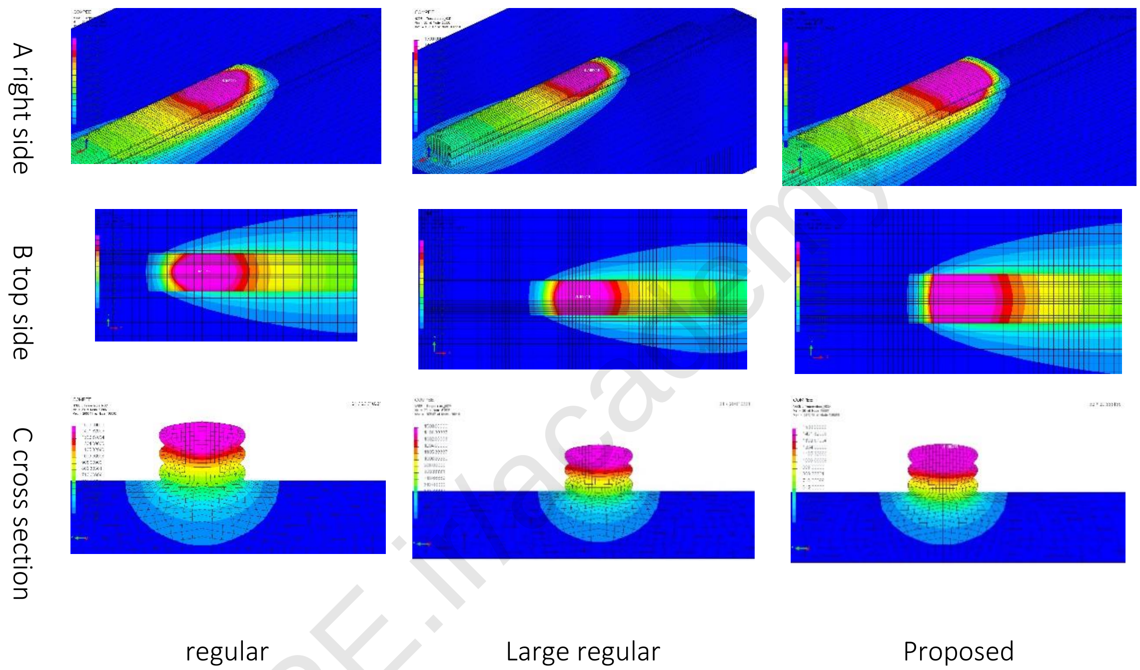

Figure 2.40 : Thermal contours from different sides for three estimated arc dimensions

Clamping test

As the previous Heat test proved that there was no difference if the sample was computed by the half or not, the temperature distribution around the sample was symmetric around the symmetric plane if the heat boundary conditions remained appropriate conditions. And, the purpose of that was to decrease the running time for computational processes. So, it was required to do the same for the residual stress, as they were interest areas for the research. This could be considered as the clamping effect or the clamping test for the AM for few layer depositions. The test had two samples: one was the complete sample and the second was half of it. The second sample was half of the complete one – at the middle of the large one – one of the tests was created from symmetric plane through the sample on the X axis; all the samples were tested for showing the σ_{XX} residual stress contours. Figure .2.41 A shows the symmetric plane of sample around X-axis and the complete one. Figure 2.41 B) shows the complete sample with three layers for decreasing the time of computation. Also Figure. 2.42 shows (in red) the clamping element for the first next tests.

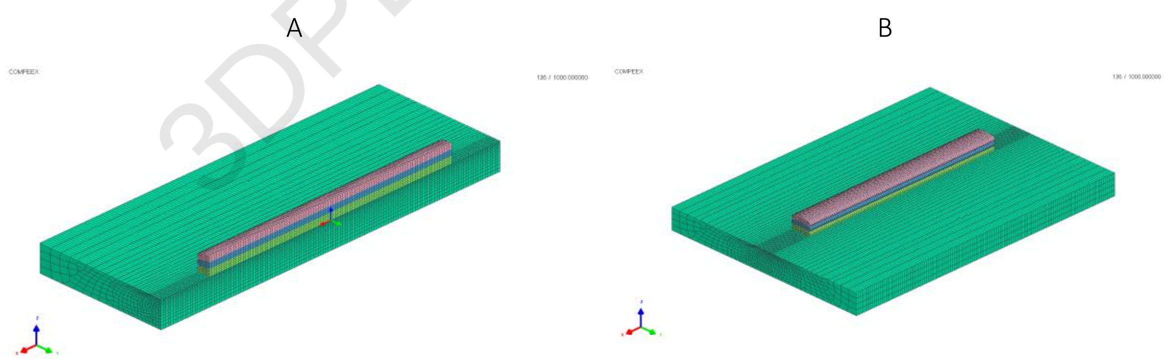

Figure 2.41: The complete sample(right) and the half sample (left)

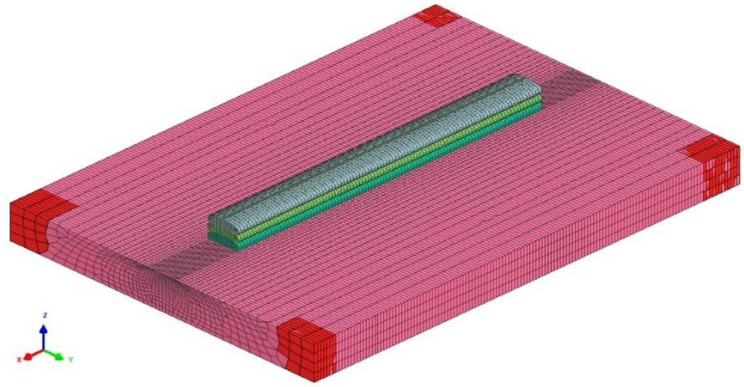

Figure 2.42 : The clamping condition for the whole sample.

The test was conducted when the clamping held the sample in one dimension (Z-axis): this axis was fixed. That meant the clamping elements were prevented from moving in this direction, which made them resistant to changes from neighboring elements. The half sample had another clamping condition: it was symmetrical assumption on the cross section cut. So, the cross section was fixed on moving Y axis

Figure. 2.43 shows the color scale for the residual stress, besides the used unit for the stresses on the test samples.

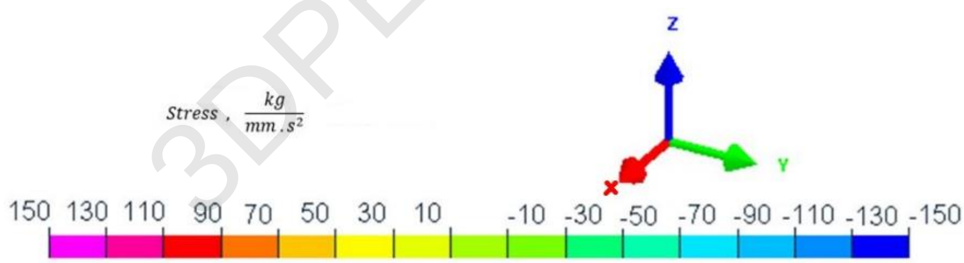

Figure 2.43 : Color scale for the stress

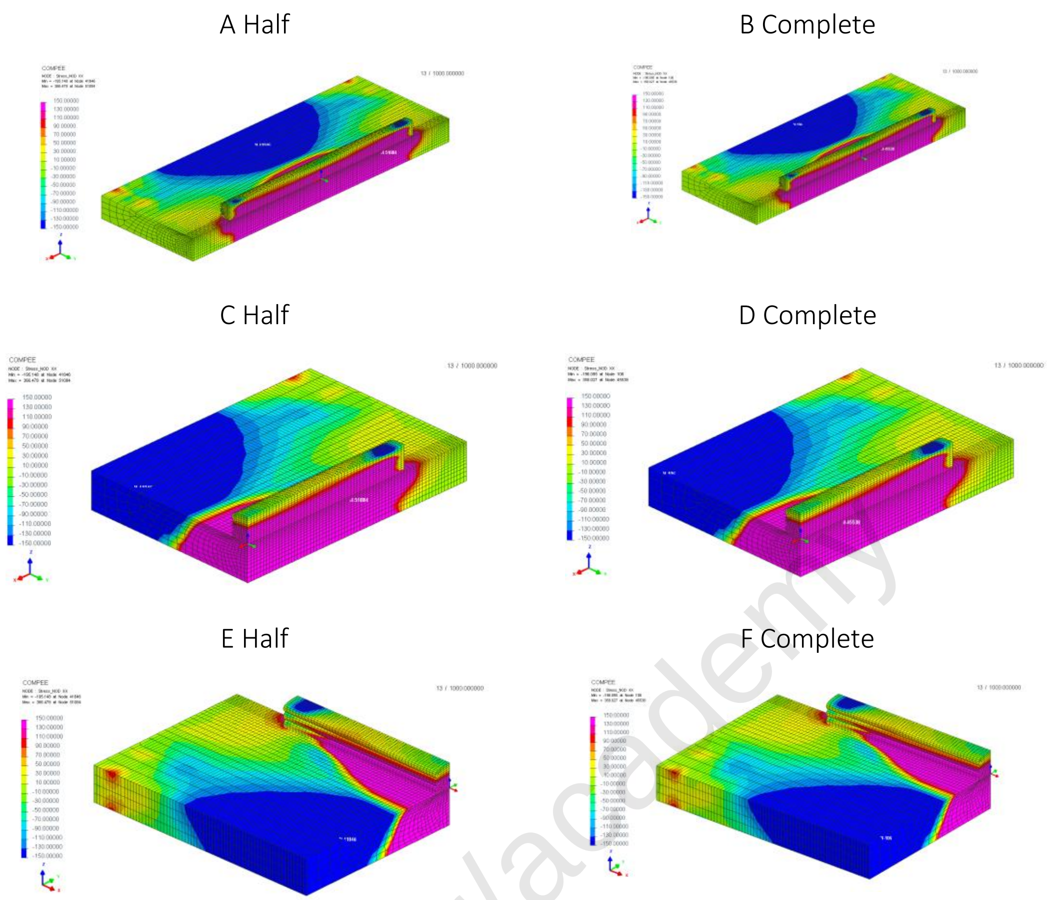

Figure 2.44 : Isometric σ_{XX} residual stress contours for regular clamping (fixed X, Y, and Z)

Figures 2.44 A, C, and E illustrate isometric contours for the σ_{XX} residual stress for the half sample and Figures 2.44 B, D, and F show the same result for the complete sample.

It is clear Figures 2.44 A, C, and E look like Figures 2.44 B, D, and F. Moreover, the complete sample was symmetric thermally and mechanically, as shown in the Mesh test (see Figures 2.29-36), also it was efficient to create a symmetric plane which divided the sample into two parts around the deposition direction to reduce the computation time because the number of elements was reduced to half. Furthermore, the affected factor, which was the welding heat, was on the center of the sample, and the heat contours were symmetric because there were other factors to change the distribution. The clamping effects were as much as the heat source effects on the mechanical properties. So, knowing the right boundary condition and the state of the models before and after made it easy to create less computational processes: in this case, the boundary conditions were two main conditions thermal and mechanical conditions. For the thermal making, the cross-section symmetric plane was insulated, while for the mechanical, the cross section symmetric plane was fixed for the symmetric axis. Moreover, Figure 2.45 shows the result of this test for the displacement on Z-axis. In addition, Figure 2.45 A similar to Figure 2.45 B, they were the same and there was no difference between the complete and the half sample in terms of stress and displacement. For sure, there may have been a slight difference but, overall, it looked the same

A Half B Complete

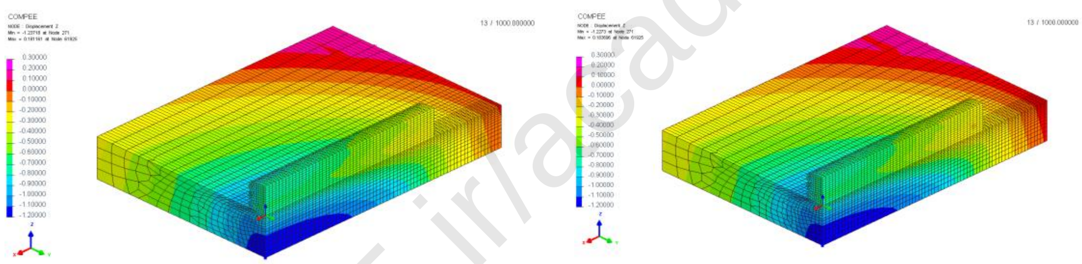

Figure 2.45 : Isometric σ_{XX} residual stress contours for fixed X-axis clamping condition

Chapter 3 Results

The models in Figure 2.1 and Figure 2.7 were formulated using two different materials with the welding parameters given in table 3.1. The purpose was to study the residual stress and distortion of this WAAM printed part as shown in Figure 2.1 using two different materials.

Table 3.1 WAAM simulation processes parameters in SYSWELD

Wire Type					welding speed	
austenitic stainless-steel grade 316L			Low carbon steel S355J2G3		2.5 mm/s	
Layers, Number	length	width	Thickness	Substrate Dimension	AMP	voltage
38 Layers	700 mm	8 mm	2.4 mm	5 X 100 X 800 mm	70	22V

Results for austenitic stainless-steel grade 316L at heat input 325 J/mm

The first simulation process was for austenitic stainless-steel grade 316L, which has specifications as below in Table 3.2 and mechanical properties as in Table 3.3.

Table 3.2 : Chemical composition of austenitic stainless-steel grade 316L from "ESI Group" software database

Element	C	Cr	Mn	Mo	Ni	P	S	Si
%	0.03	17	2	2.5	12	0.045	0.03	0.75

Table 3.3 : ASTM Mechanical Properties of Austenitic stainless-steel grade 316L

Element	Tensile strength (min)		Yield strength (min)		Hardness (max)	
	ksi	MPa	ksi	MPa	Brinell	Rockwell
316L	70	485	25	170	217	95

As the process was simulation welding, all the elements on the model would have to meet the melting temperature; in order to simulate the real processes as much as we can. For that, a set of nodes around a chosen layer have been selected Figure 3.1.

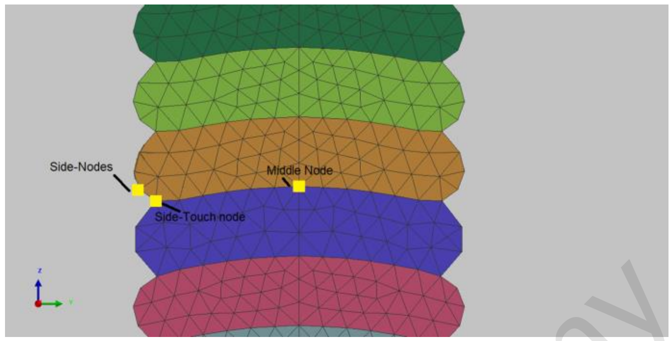

Figure 3.1 : Locations of interest nodes around a layer

Figure 3.2 shows the middle nodes temperature curves for layers 5,16,28, and 37. Knowing that the melting point is between 1371-1400°C, the middle node melts twice during the process; for example, the first melting time when the Layer_2 is formed and the second melting time when the layer_3 is deposited. Moreover, This case of melting the center of two layers describes what happens, as shown in Figure 2.11, when the real layer does not only have one, but two concave shapes.

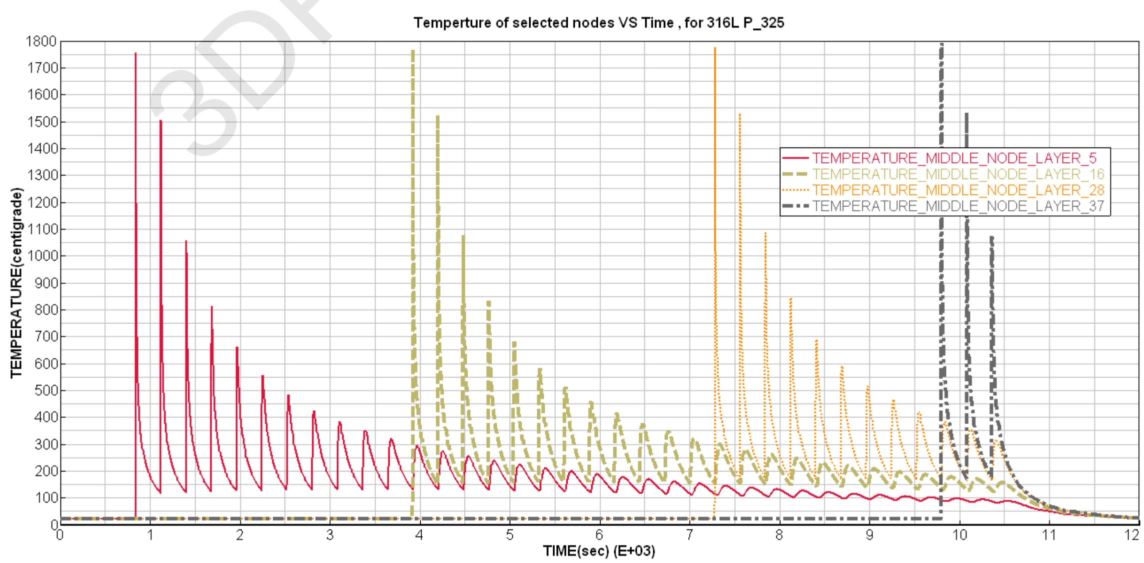

Figure 3.2 : Temperature behavior of Middle nodes for 316L, heat input 325 J/mm of Layers 5,16,28, and 37

For the middle nodes from figures 3.2, the peak temperature reaches 1700°C. This is because these nodes are under the heat source directly. Also, these nodes re-melt again with the next layer. The re-melting temperature reaches 1500°C, which is higher than the melting point. But for the third cycle the temperature reaches 1050°C for the center nodes, which is lower than the melting point by more than approximately 200°C.

Figure 3.3 shows the thermal curves pertaining to side-touch nodes for layers 5, 16, 28, and 37. For the side-touch node, which is the side-node farther from the middle node and has contact to the layers before and after it, this node melts twice, too. For e.g. one from layer 6 and the other from layer 7 deposits. But this particular node has a lower temperature from that of the middle nodes, since the middle nodes are closer to the heat source. In addition, these thermal cycles make the joining processes efficient on AM. But when the heat input is 325 J/mm, the simulation process indicates one full melting cycle. This means that this particular node at this power melted once at the first deposit. But when the latter layer deposited, it did not reach the melting-point temperature; which was approximately 1385°C.

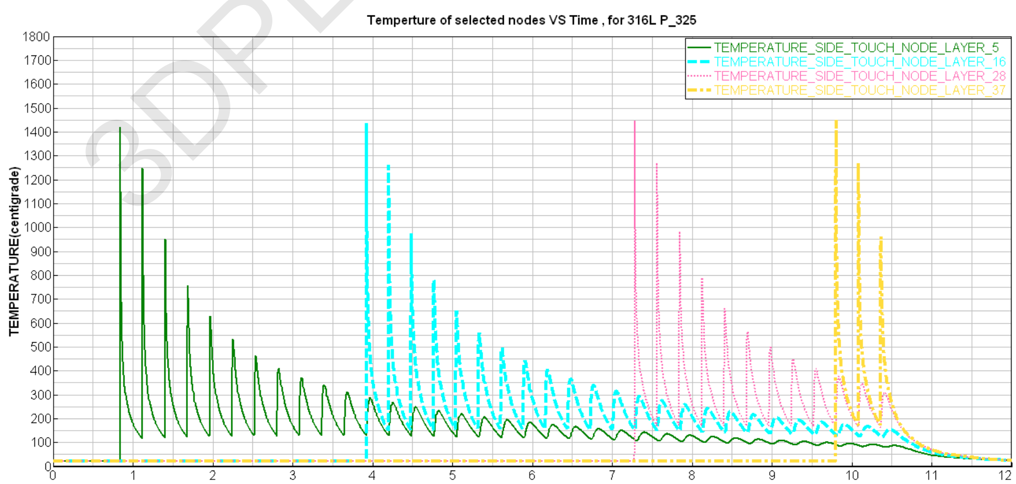

Figure 3.3 : Temperature behavior of side-touch nodes for 316L, heat input 325 J/mm of Layers 5,16,28, and 37

From figures 3.2 and 3.3, the thermal effect of the 25th layer or any layer beyond the first layer did not exceed 50°C. This meant that the WAAM processes are repeated after 25 layers This also meant that the layers repeat the same pattern of the first group of 25 layers. Also, the mechanical properties would not be affected by the heat directly but by the thermal and mechanical impact of the active layers.

The rest of the nodes, as shown in Figure 3.4, are those on the sides of layers 5, 16, 28 and 37. These have to be melted once for the same deposited layer. But, if they melt above the threshold, it will cause worse surface finishing. But, for these heat input parameters the peak of side nodes did not meet the melting temperatures, so it would cause un-melting nodes on the simulation, In the next section, a different heat input was simulated in order to see the effect of melting temperature for the nodes. From the previous figures 3.2 to 3.4, it seemed the peak temperature of a single layer decreased as an exponential function.

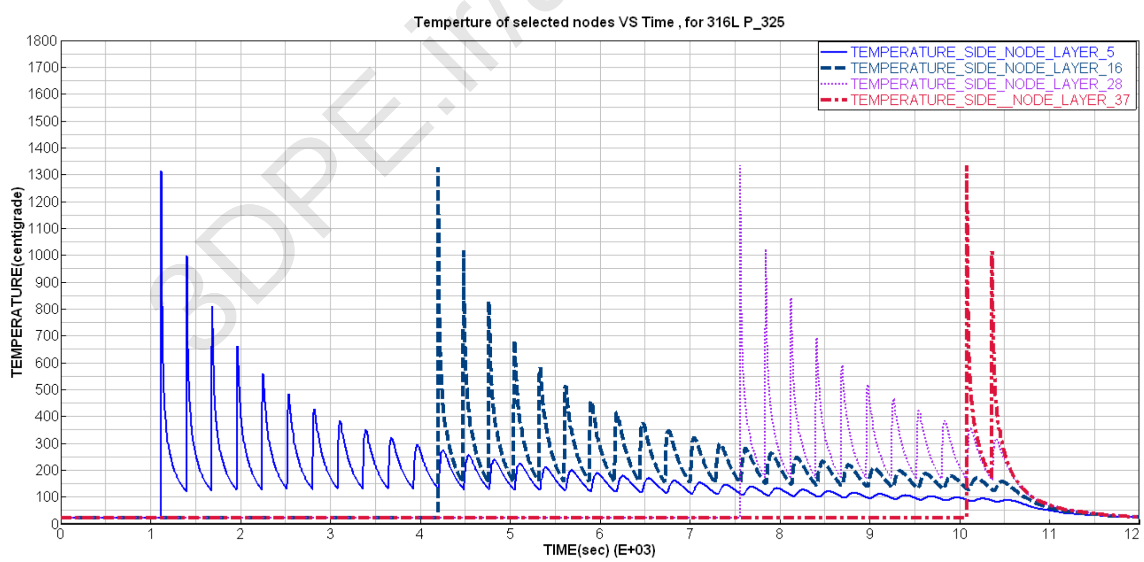

Figure 3.4 : Temperature behavior of side nodes for 316L, heat input 325 J/mm of layers 5,16,28, and 37

σ_{XX}- Residual Stress result of austenitic stainless-steel grade 316L at heat input 325 J/mm

Residual stress can change the shape of the part or its mechanical properties. For 3D printing WAAM, residual stresses are considered higher than that of other manufacturing processes. This was because of the effect of periodic welding heat on the part. This research focuses on two types of residual stresses - 1) Longitudinal and 2) Maximum principle stresses, the longitudinal stress is present to show the stress created in the same direction of the deposition processes, while the maximum is chosen in order to show the other types of stress effects in total. Also, all the results are taken after the sample cooled for 1500 seconds after completion of the welding, i.e., the sample cooled to room temperature.

Figure 3.5 shows σ_{XX}-Residual stresses (Longitudinal) for a cross section on the middle of the sample. The maximum σ_{XX}-residual stress is 361.26 MPa in tension and the minimum is -291.118 MPa in compression. The contour shows three main regions of residual stress. The first region is in the top region of the part, which is around the last 8 layers. The stress in this region is in a state of tension. The second region is between the 5th Layer and the 30th layer and is in compression. The third region comprises the layers around the base, which is in in tension. The right and left sides seem to have lower stresses compared with the regions in the middle. Also, it seems the clamping conditions made an alteration to the residual stresses because the values of the residual stresses in all the regions had a pattern that changes around the clamps either increase in the stress value or decrease .

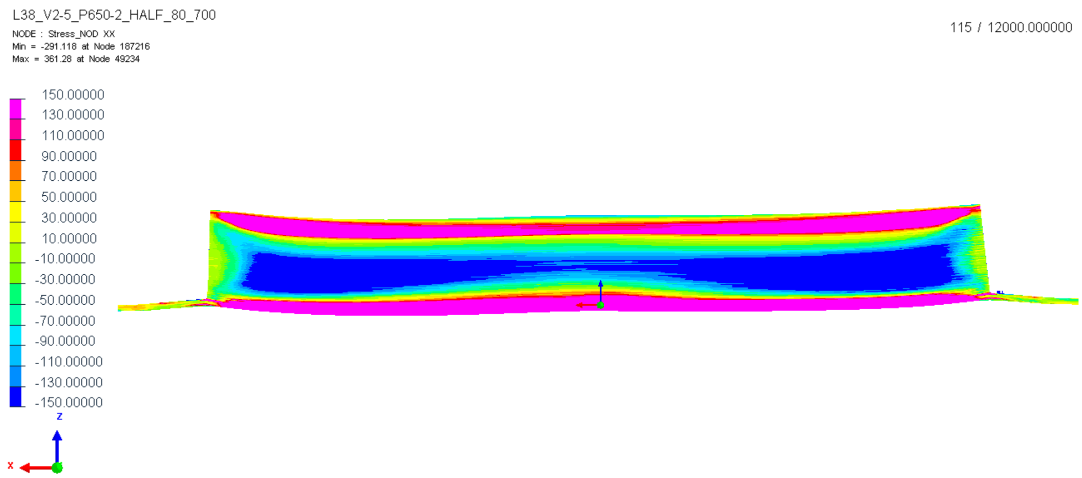

Figure 3.5 σ_{XX} - Longitudinal Residual stress of 3D printed 316L at heat input 325 J/mm X-Z plane -cross section view

Figure 3.6 shows the other side of figure 3.5. In this figure, the effects of clamp places are clearer than those in the last figure 3.5. Also, the regions are in the same state from the outside the pieces and the inside part of the symmetric plane. Furthermore, the base plate is in Compression. At the corners of the base, the stresses tend to be around a zero-stress situation since they are the farthest points from the direct heat effected region.

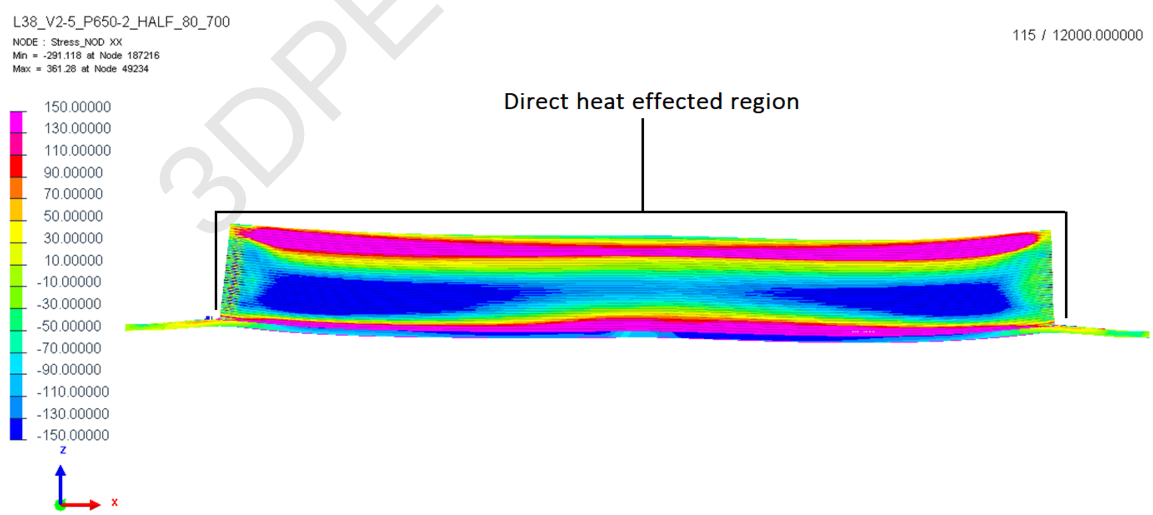

Figure 3.6 σ_{XX} - Longitudinal Residual stress of 3D printed 316L at heat input 325 J/mm X-Z plane view

Figures 3.7 and 3.8 show the same results as in figures 3.5 and 3.6, with an isometric view. These two figures show the effects of the clamps clearer than the last two figures 3.5 and 3.6, especially at the center of the base. Figure 3.8 shows the different regions of the stresses around the base. At the end and the start points of printing, the stress switches from compression to tension. The displacements of the z axis around the end and the start points are the highest among the base.

Figure 3.7 σ_{XX} - Longitudinal Residual stress of 3D printed 316L at heat input 325 J/mm Isometric-cross section view

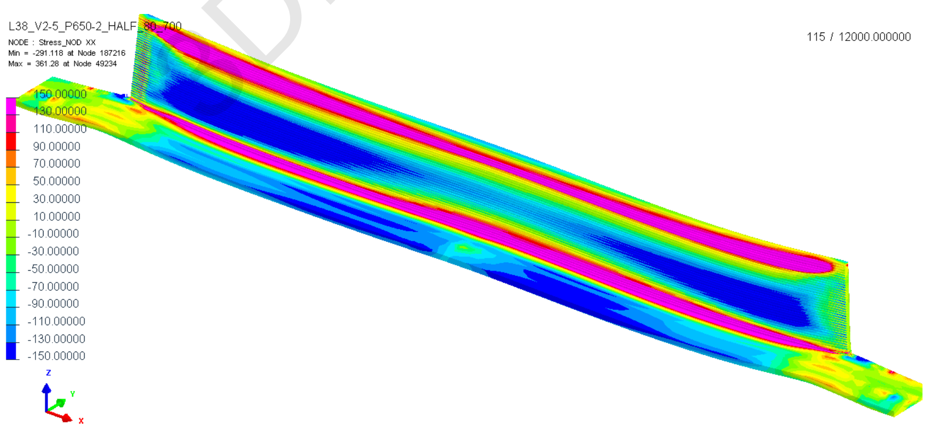

Figure 3.8 σ_{XX} - Longitudinal Residual stress of 3D printed 316L at heat input 325 J/mm Isometric view

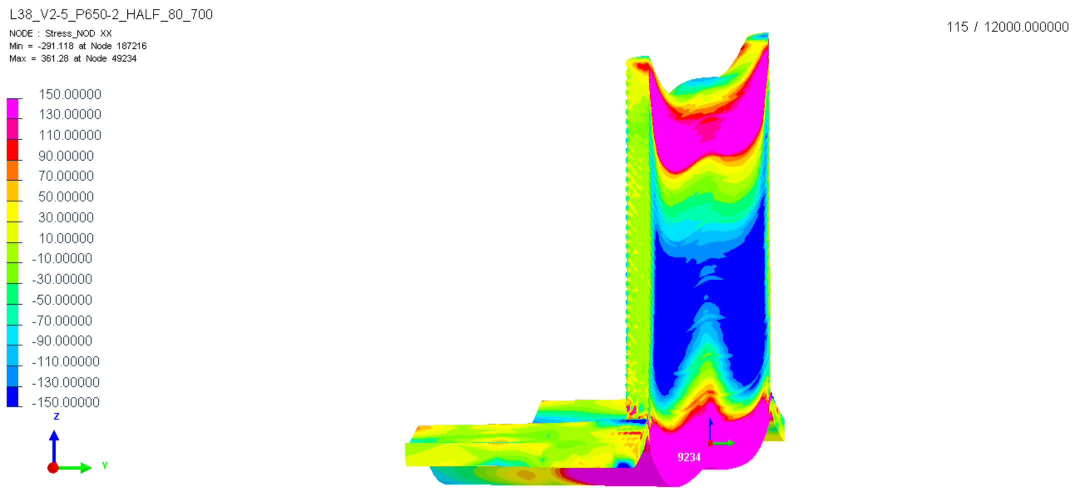

Figure 3.9 σ_{XX} - Longitudinal Residual stress of 3D printed 316L at heat input 325 J/mm Y-Z plane -cross section view

Figure 3.9 shows a cross section on the middle of the sample, as figure 3.5 is viewed from a different angle. From this side, the distortion is clear. It seems that the ends are higher than the center, also they have the lowest stress value. While comparing 3.9 with figure 3.10, the stresses' regions in figure 3.10 had a smaller area than the regions in figure 3.9. which means that the stresses inside the sample are in an 'intense' state.

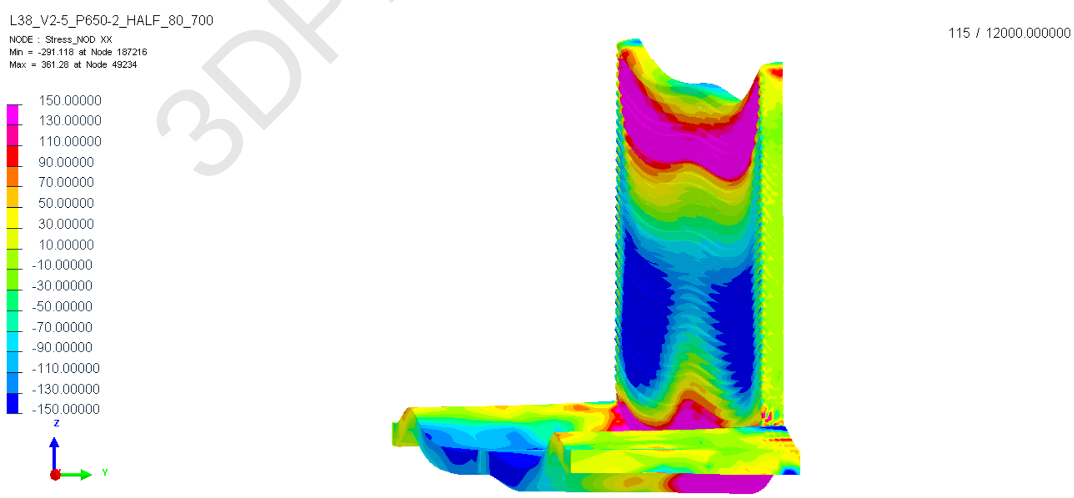

Figure 3.10 σ_{XX} - Longitudinal Residual stress of 3D printed 316L at heat input 325 J/mm Y-Z plane view

Figure 3.11 is an isometric view with slices selected parts and gives more insight into what happens inside the simulated part. It also shows the effects of the base on the printed part. It seems the base is in tension, with the printed part leads to different distortion shapes, if the printed part is cut from the base. In addition, the ends of printing part are not in the same pattern as the middle part. It is also clear here that the parts inside have much higher stresses than the parts outside.

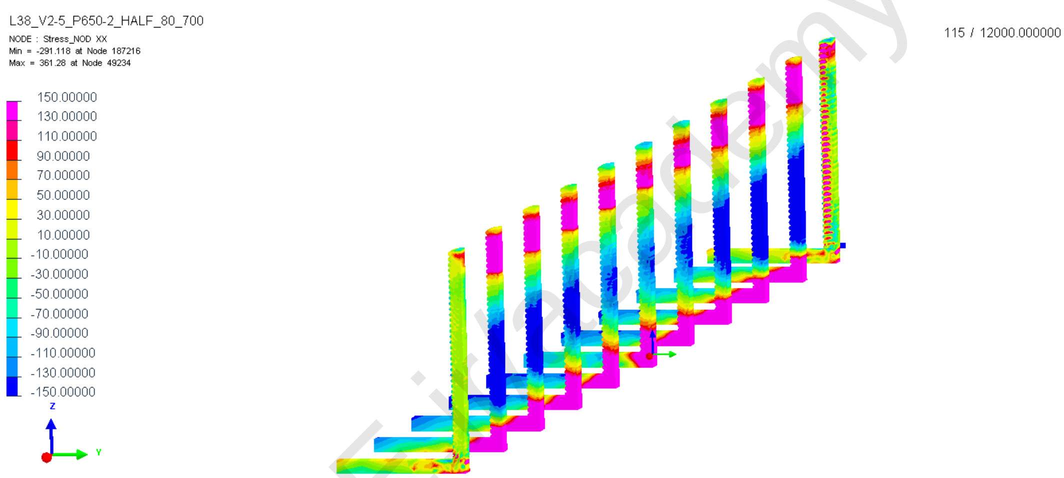

Figure 3.11 σ_{XX} -Longitudinal Residual stress of 3D printed 316L at heat input 325 J/mm Isometric-section-sliced parts view

First principle Residual Stress result of austenitic stainless-steel grade 316L with heat input 325 J/mm

The maximum principle residual stress gives a more general picture of the residual stress state than the contour plots of the σ_{XX} residual stress. As shown in figure 3.12, the contour is a cross section of the sample on the middle on the center line of the X axis. In this figure it appears that the first principle residual stress makes a “frame” around the sample and is very useful for determining the dimension of the frame in order to predict the actual stress distribution.. From figures 3.12 and 3.13, it is clear that the maximum stress value is 463.876 MPa in tension and the minimum is -83.1905 MPa in compression. It can also be observed from figures 3.12 and 3.13, that the stress divides the sample into two regions - the frame in tension and the active area in low compression, relatively. And that is applied on the both the contours, inside and outside.

Figure 3.12 First Principal Residual stress of 3D printed 316L at heat input 325 J/mm X-Z plane -cross section view

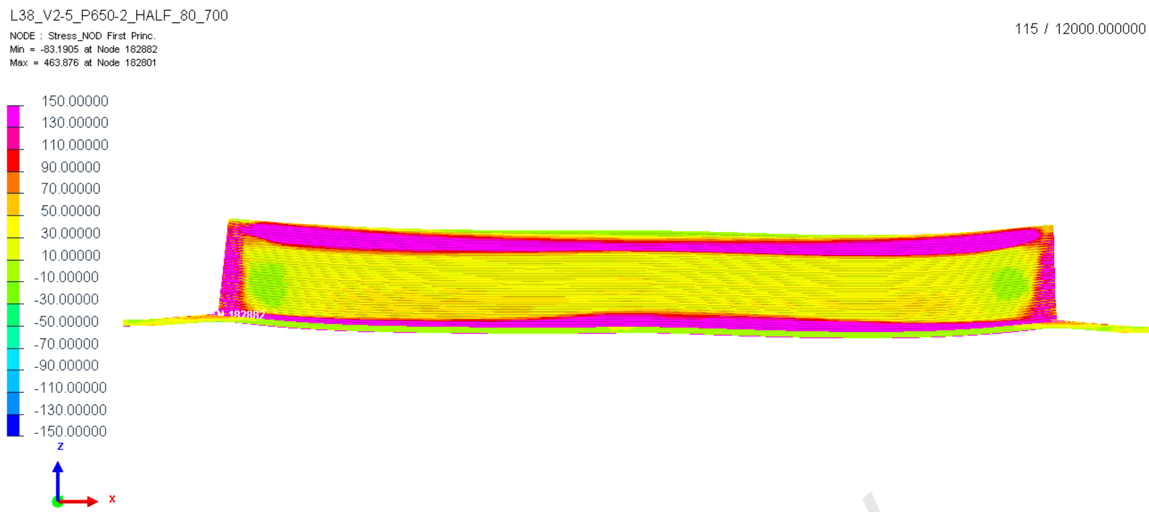

Figure 3.13 First Principal Residual stress of 3D printed 316L at heat input 325 J/mm X-Z plane view

The figures 3.14 and 3.15 show the isometric views for the sample. These two figures show the base of the printing in low stresses, which means the stress averages are low on the base as compared to the frame of the printed part.

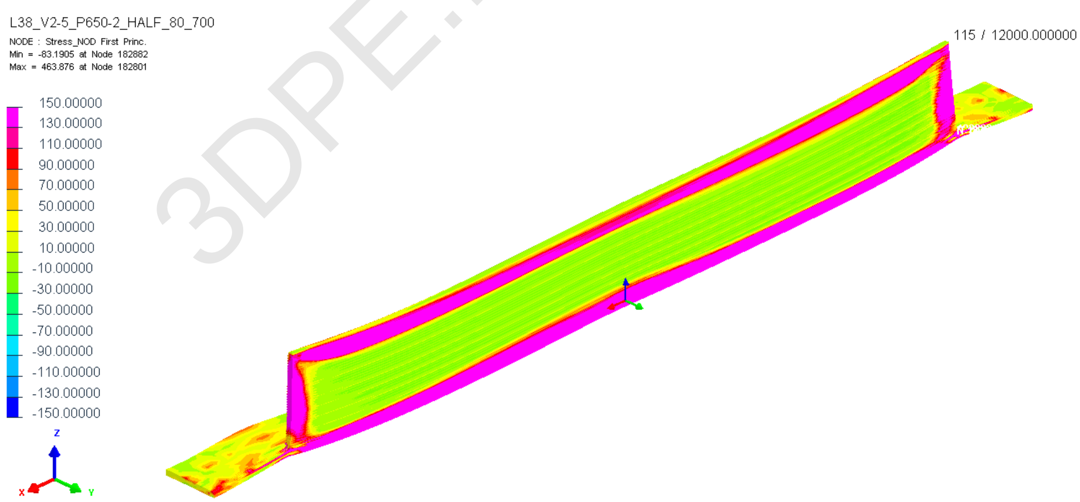

Figure 3.14 First Principal Residual stress of 3D printed 316L at heat input 325 J/mm Isometric-cross section view

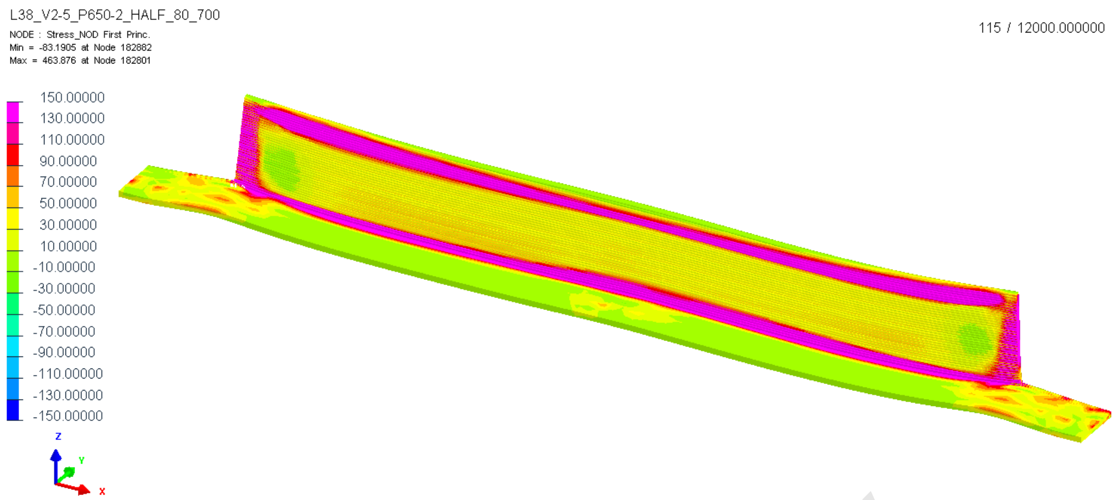

Figure 3.15 First Principal Residual stress of 3D printed 316L at heat input 325 J/mm Isometric view

In figures 3.16 and 3.17, the distortion is clear, but there is a unique occurrence between the layers. It seems that the layers inside are in compression mode while the areas between them are in tension mode. However, both these stresses are low as compared to the frame stresses around the active area.

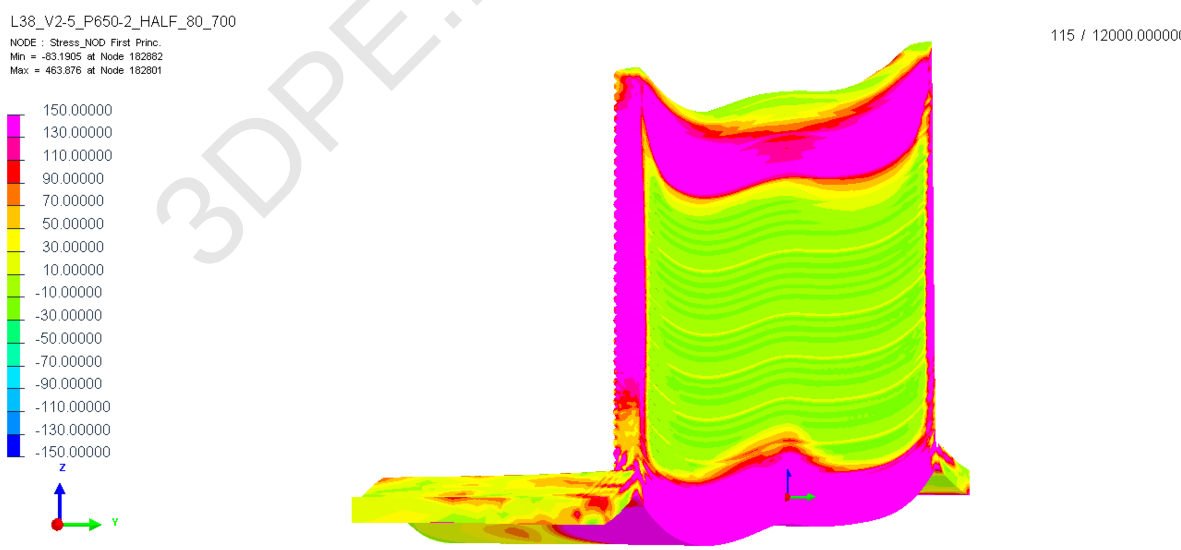

Figure 3.16 First Principal Residual stress of 3D printed 316L at heat input 325 J/mm Y-Z plane -cross section view

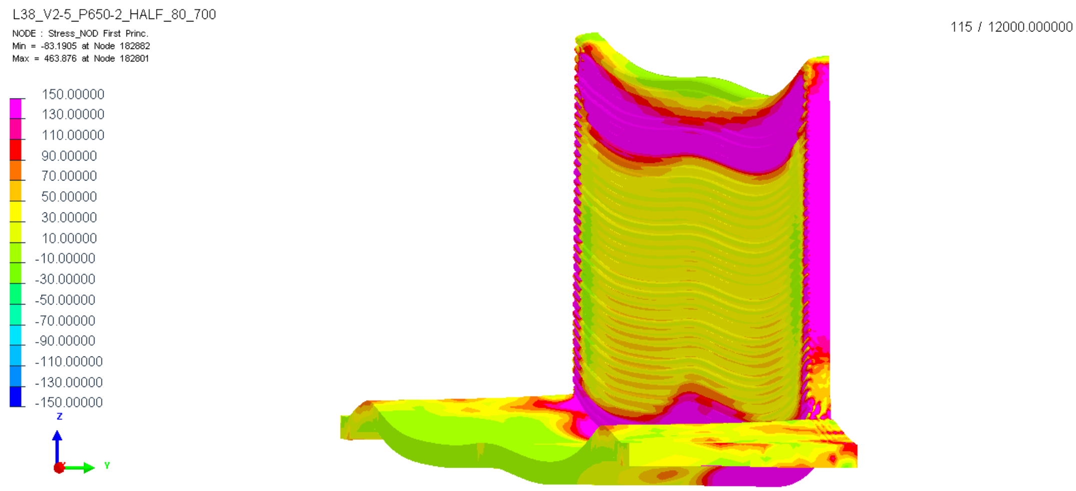

Figure 3.17 First Principal Residual stress of 3D printed 316L at heat input 325 J/mm Y-Z plane view

Figure 3.18 shows the sliced parts of the sample. In this figure the active area which has the lower first principle residual stress has a clear dimension and a clear edge for the cutting processes after printing. It could be because the stress frame has a certain level of layers, which for any 3D printing process has to be considered as a waste section.

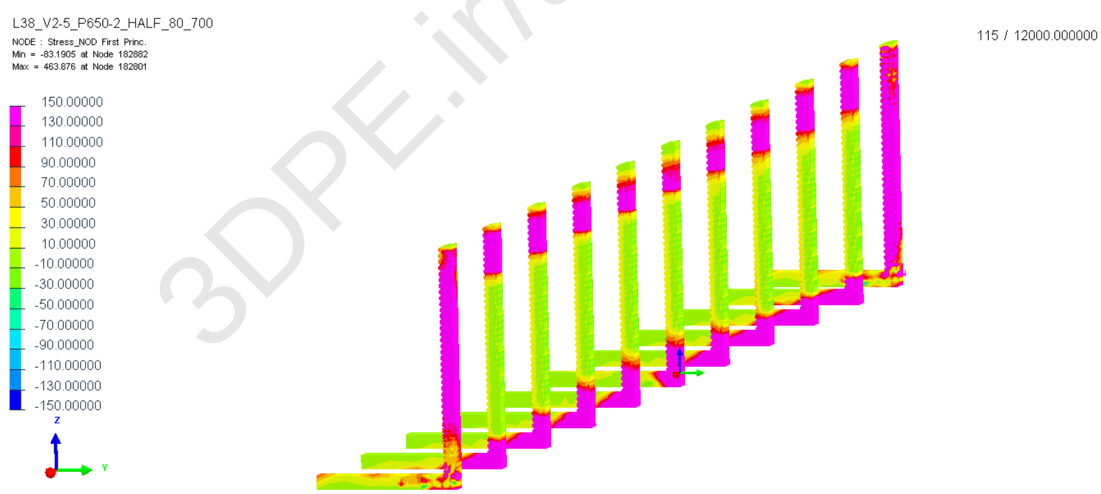

Figure 3.18 First Principal Residual stress of 3D printed 316L at heat input 325 J/mm Isometric-section-sliced view

Figures 3.19 shows the displacements on the Z-axis as curves for layers 3-14-25-36. These curves go below zero, the reason for which is the last free clamps, which distort the sample as if in a vacuum, without limits. The highest displacement is around 15 cm at the beginning of the 3D printing. Also, the lowest distortion is between the center and the ends. From this figure it appears that the clamps affect the distortion in a destructive manner for the clamp at the center. But it could perhaps be good for other clamping conditions. The highest displacement point relative to the length of the sample is around 2%, a high undesirable value, as a benchmark for good tolerance demands in the industry.

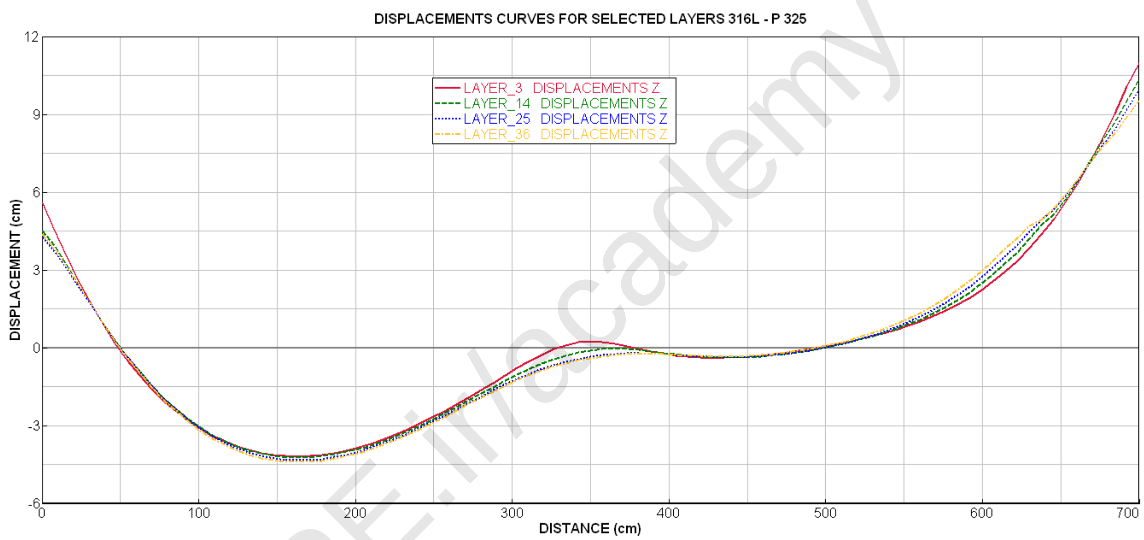

Figure 3.19 Displacements curves for Layers 3-14-25-36 of 316L , heat input 325 /mm after printing

Results of austenitic stainless-steel grade 316L at heat input 345 J/mm

As illustrated in the previous section, the heat input was 325 J/mm. For some nodes it does not meet the melting temperature. So, this case uses a higher heat input, which was determined by testing different heat inputs. Figure 3.20 shows the middle nodes' temperature curve for the same parameters in the last section but with heat input as 345 J/m. These temperature curves reach the melting temperature point twice. For the third cycle it reaches 1200°C. But this is a pattern different from the previous section. In this case (345 J/mm) the peak temperature for the first 16 layers is lower than the previous layers by about 200 degrees Celsius.

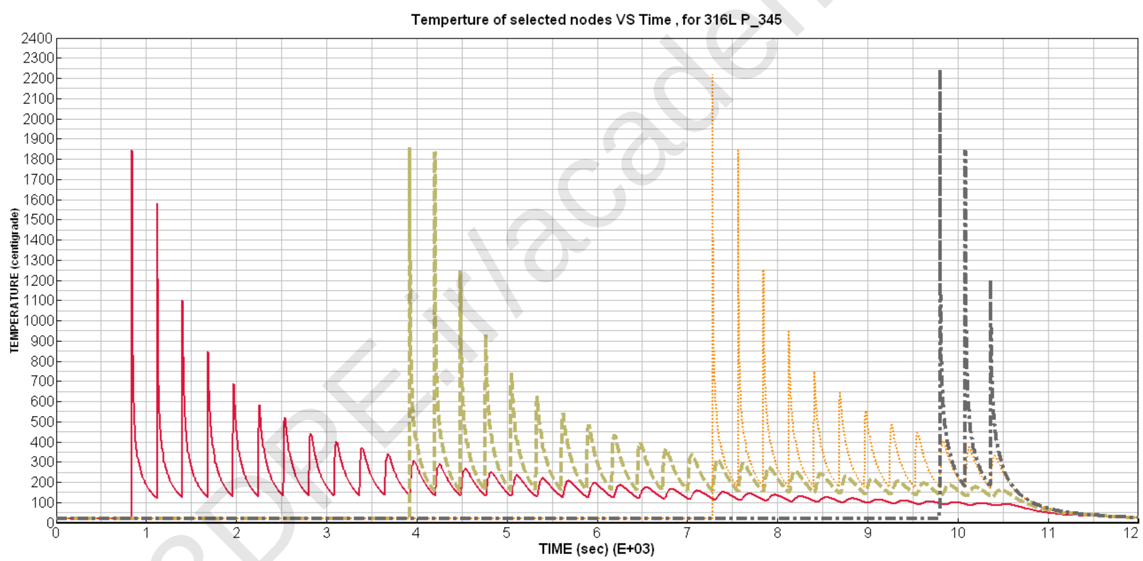

Figure 3.20 Temperature behavior of Middle nodes for 316L, heat input 345 J/mm of Layers 5,16,28, and 37

Figure 3.21 shows the temperature curves for the side-touch nodes, with the heat input as 345 J/mm. The problem of nodes with non-meeting melting temperature is thus resolved. All the side-touch nodes reach the melting-point temperature twice in this case, just as expected in the lab experiment.

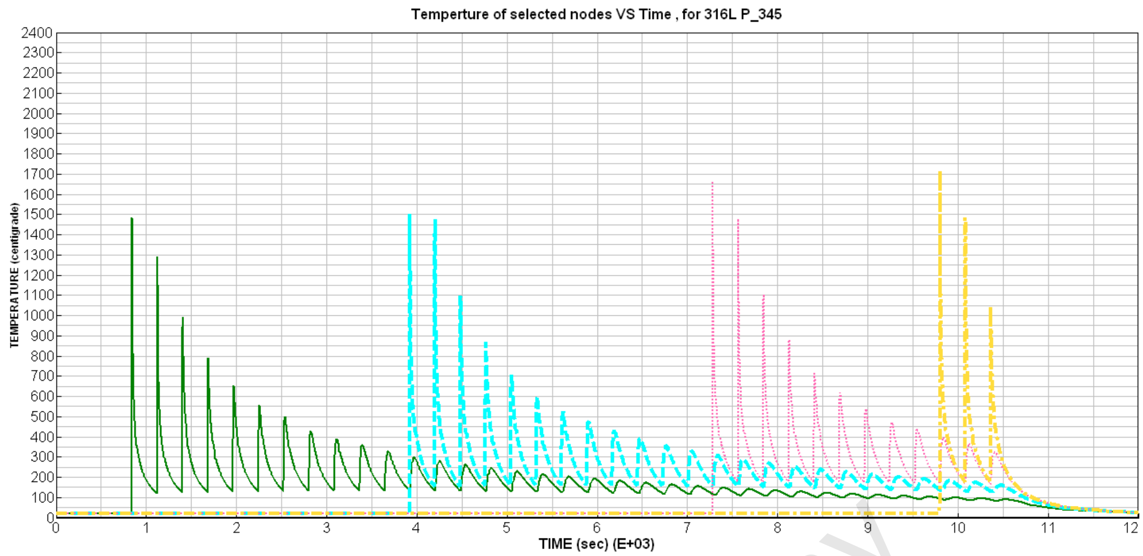

Figure 3.21 Temperature behavior of side-touch nodes for 316L, heat input 345 J/mm of Layers 5,16,28, and 37

The last temperature case is that of side nodes as in figure 3.22, which must melt at least once. In this case, with the new heat input, the peak temperature for these nodes reaches the melting point. For the second cycle, the temperature is lower than the melting temperature by around 200 degrees Celsius, as observed for each node.

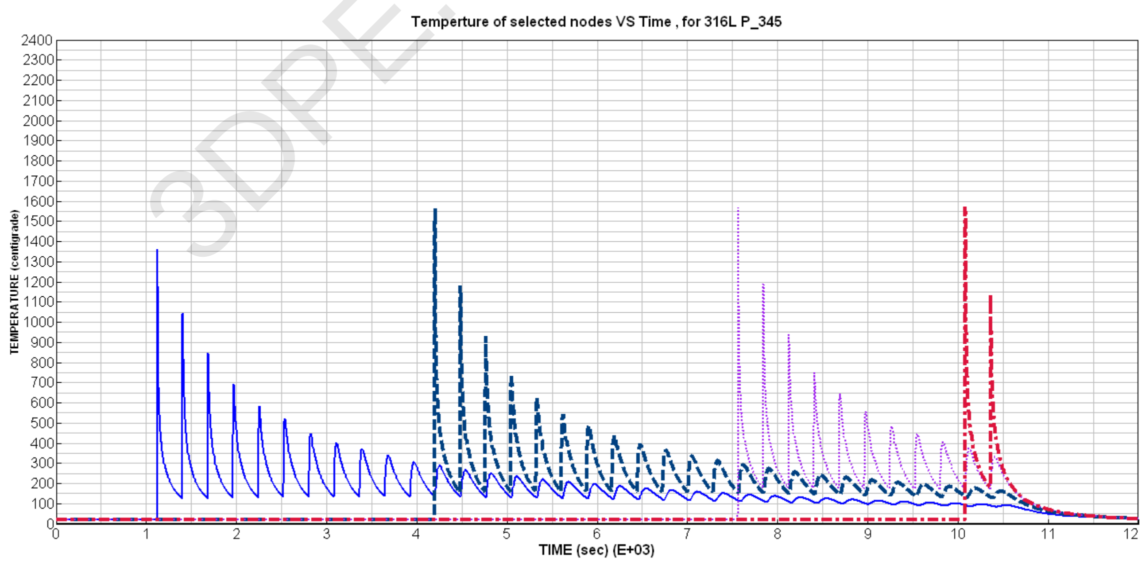

Figure 3.22 Temperature behavior of side nodes for 316L, heat input 345 J/mm of layers 5,16,28, and 37

σ_{XX} - Residual Stress result of austenitic stainless-steel grade 316L at heat input 345 J/mm

The main objective for repeating these simulations with different heat inputs was to observe the difference between the residual stresses of the sample nodes, whether they meet the melting-point temperature or not. For exhibiting σ_{XX} residual stress, it would suffice to present the last three figures of the previous section. Comparing information between figure sets 3.9, 3.10, 3.11 and 3.23, 3.24, 3.25, it seems they are similar in terms of contours and regions. Therefore, for σ_{XX} residual stress the melting-point temperature does not affect the final result of the stress, as long as the peak temperature of the nodes reaches near the melting-point temperature.

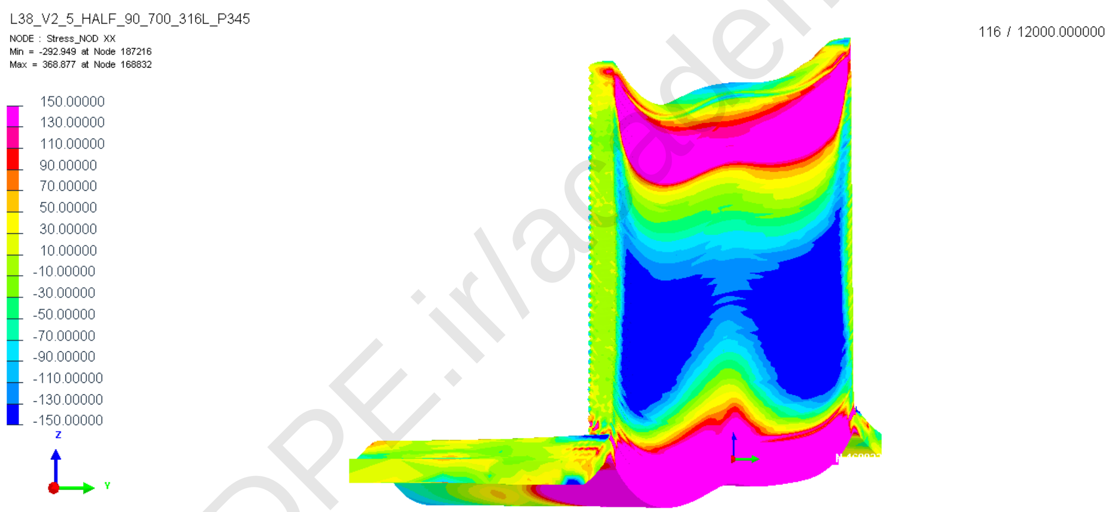

Figure 3.23 σ_{XX} - Longitudinal Residual stress of 3D printed 316L at heat input 345 J/mm Y-Z plane -cross section view

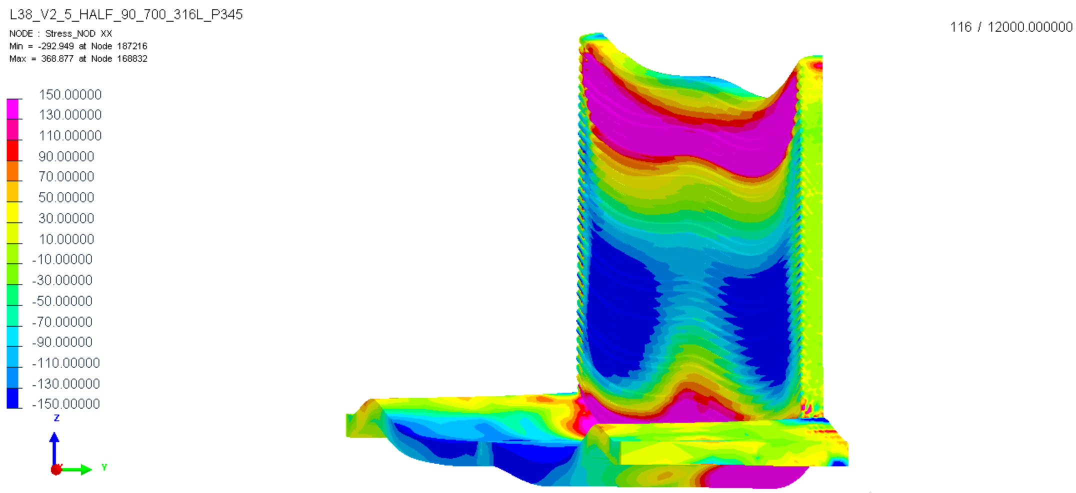

Figure 3.24 σ_{XX} - Longitudinal Residual stress of 3D printed 316L at heat input 345 J/mm Y-Z plane view

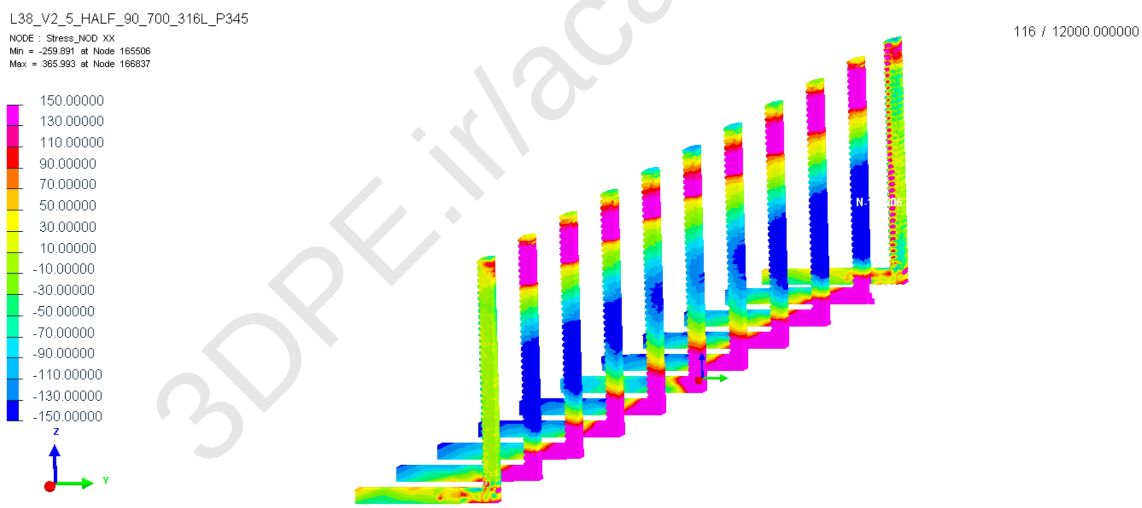

Figure 3.25 σ_{XX} -Longitudinal Residual stress of 3D printed 316L at heat input 345 J/mm Isometric-section-sliced view

First principle Residual Stress result of austenitic stainless-steel grade 316L at heat input 345 J/mm

Also, for first principle residual stresses, it does not need to compare each aspect. It is enough to compare three figures between these cases with different heat input. Comparing figure sets 3.16, 3.17, 3.18 and 3.26, 3.27, 3.28, they look similar as well. So as in σ_{XX} stress, the First principle does not alter much across different heat inputs.

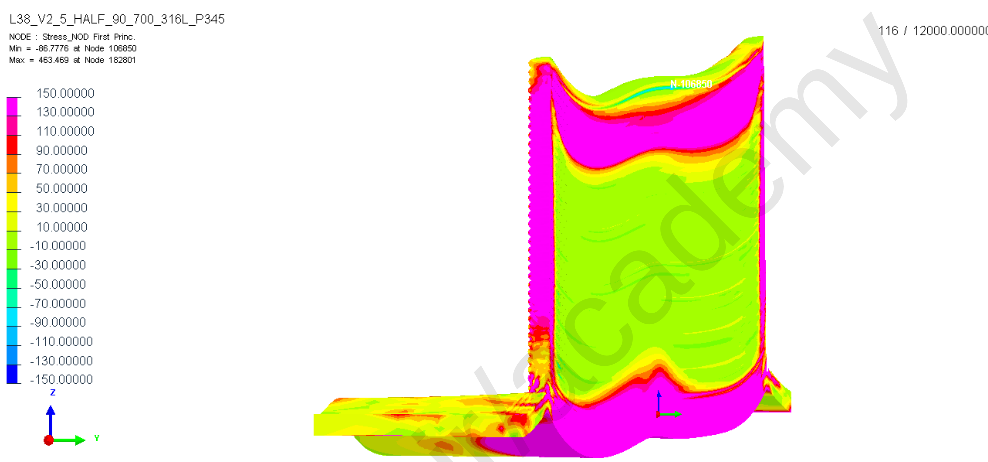

Figure 3.26 First Principal Residual stress of 3D printed 316L at heat input 345 J/mm Y-Z plane -cross section view

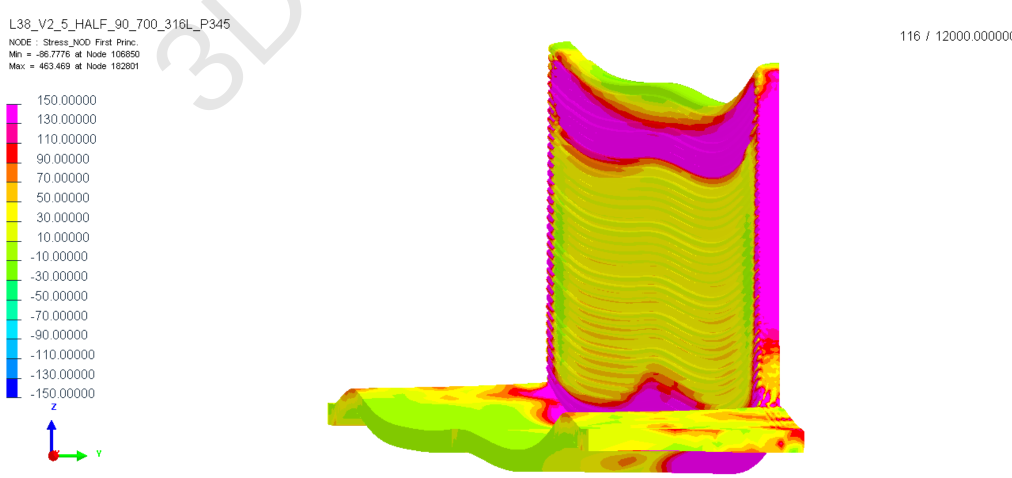

Figure 3.27 First Principal Residual stress of 3D printed 316L at heat input 345 J/mm Y-Z plane view

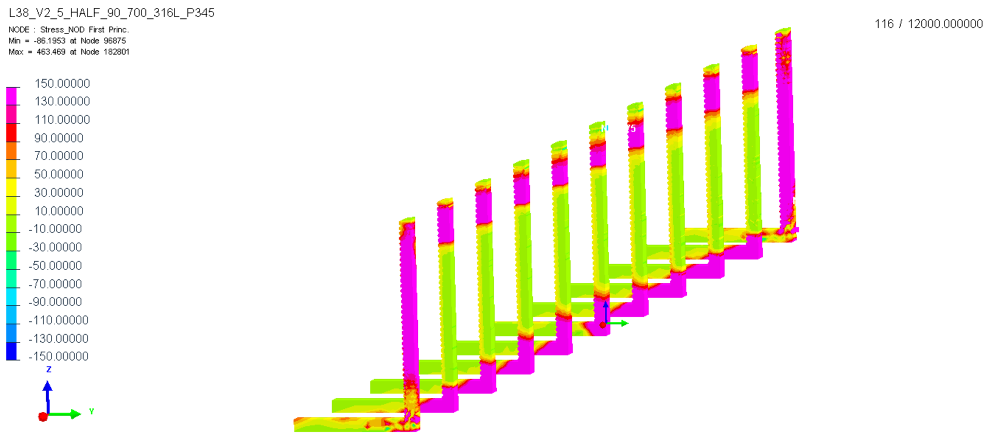

Figure 3.28 First Principal Residual stress of 3D printed 316L at heat input 345 J/mm Isometric-section-sliced view

In addition to the above comparisons, between figure 3.23 and figure 3.28, it is observed that, in general, the displacement curves' shapes are the same. However, there is a difference at node ID 150. The concave of the case with heat input 345 J/mm is slightly lower than the case where the heat input is 325 J/mm. The reason could be the increase in heat input. However, they follow the same pattern, as seen in the graphs.

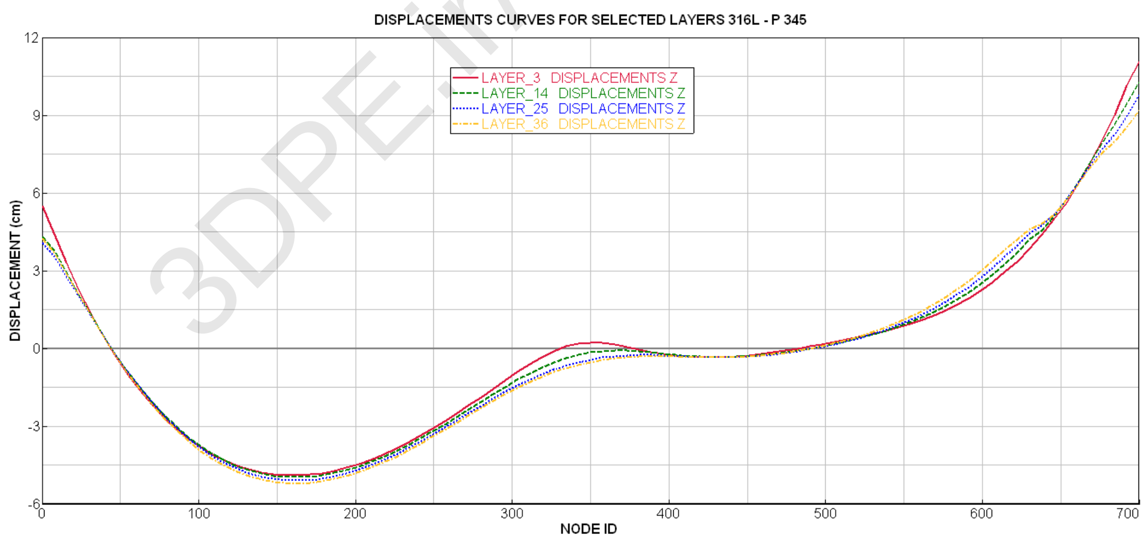

Figure 3.29 Displacements curves for Layers 3-14-25-36 of 316L , heat input 345 /mm after printing

Results for Low carbon steel S355J2G3 at heat input 405 J/mm

The third case is that of a 3D printing simulation process for the same parameters as in the first case and as shown in table 3.1. This is with a different material - Low Carbon Steel S355J2G3. This material melts around 1500°C, so it needs a higher heat input, the appropriate heat input value for this case is 405 J/mm. Table 3.4 shows the chemical composition of Low Carbon Steel S355J2G3, as it is used in the simulation software SYSWELD. Also, it has the mechanical properties shown in Table 3.5.

Table 3.4 : Chemical composition of Low carbon steel S355J2G3 from ESI database

Element	C	Mn	P	S	Si
%	0.18	1.6	0.035	0.035	0.55

Table 3.5 : Mechanical Properties of Low carbon steel S355J2G3

Element	Tensile strength, min		Yield strength, min		Hardness, max	
S355J2G3	ksi	MPa	ksi	MPa	Brinell	Rockwell
	98	680	50	345	187	90

For the same procedure, the nodes described in figure 3.1 have a temperature description for the layers. Figure 3.30 shows the temperature behavior of the middle nodes for layers 5,16,28, and 37 in this case. As the material melts around 1500°C, the peak temperature of the layers exceeds 2200°C and in the second cycle it reaches 1800°C, both of which are above the melting point. But for the third cycle, the temperature of the middle nodes for all layers reach 1250°C, which is below the melting point. This is the objective for re-melting the center of the layers for combining any two layers.

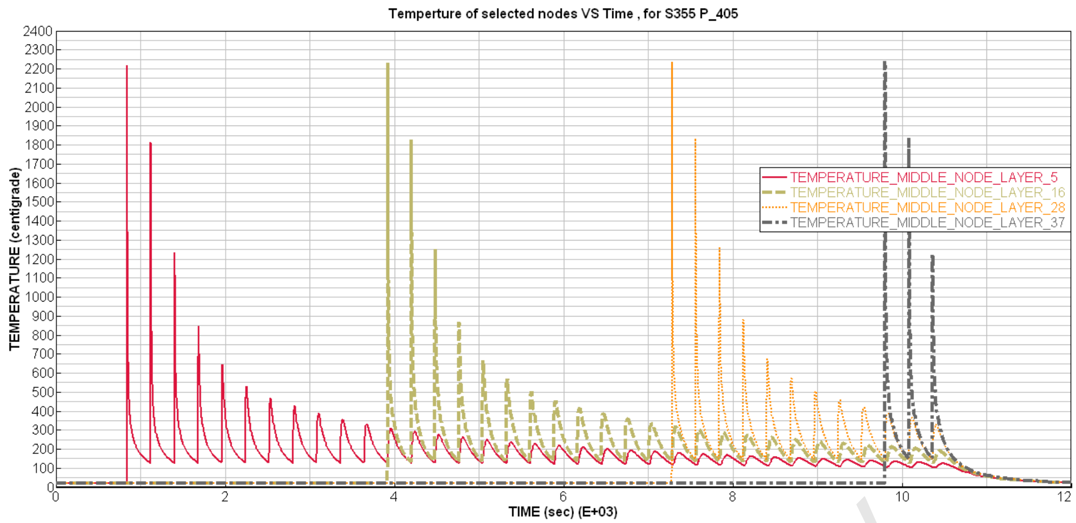

Figure 3.30 Temperature behavior of Middle nodes for S355, heat input 405 J/mm of Layers 5,16,28, and 37

Figure 3.31 describes the temperature for the side-touch nodes, as described in the earlier figure 3.1. These nodes must reach the melting point twice as the middle nodes but with a lower temperature rate. The curves in figure 3.31 are represented for layers 5, 16, 28 and 37. These nodes reach 1700°C for the first deposit and 1500°C for the second deposit. This means that the nodes melted twice. But for the third cycle all the layers do not exceed 1050°C, which is below the melting point.

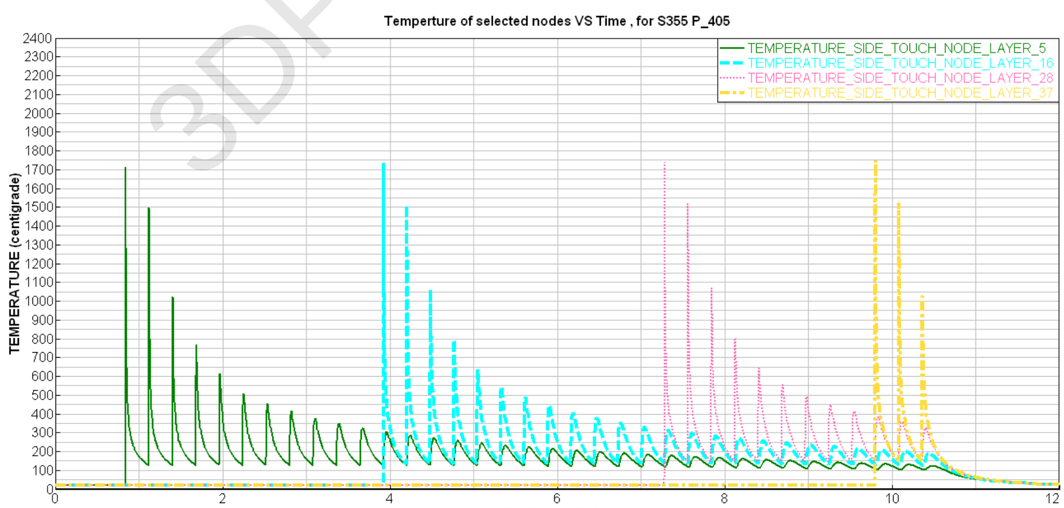

Figure 3.31 Temperature behavior of side-touch nodes for S355, heat input 405 J/mm of Layers 5,16,28, and 37

In contrast to the middle and side-touch nodes, side nodes must melt once. If the side nodes melt again, it means that the heat input is too high, and which makes the layers to not fit into each other. Figure 3.32 describes the temperature of these nodes for the selected layers - 5, 16, 28, and 37. All these layers exceed the melting point by a 100 degree Celsius. But for the second cycle none of the layers go beyond 1150°C, which is below the melting point by 300 degree Celsius.

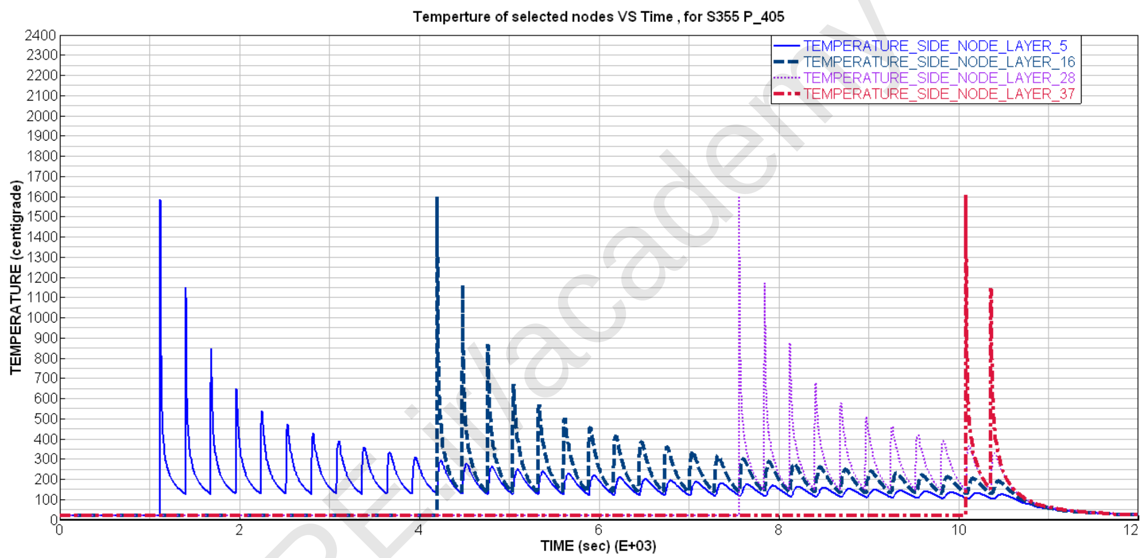

Figure 3.32 Temperature behavior of side nodes for S355, heat input 405 J/mm of layers 5,16,28, and 37

σ_{XX} - Residual Stress result of Low carbon steel S355J2G3 at heat input 405 J/mm

The most important residual stresses in any welding processes are the longitudinal residual stress which is σ_{XX} residual stress in this case. So, the first result of this case is for σ_{XX} residual stress. Figure 3.33 shows a color contour plot that describes the distribution of the σ_{XX} residual stress around the sample. In figure 3.33 the stress has a more complex distribution than in the case of stainless steel 316L. The maximum residual stress is 593.29 in tension and the minimum is -545.052. In compression, these values are higher than the yielding stress. This figure below shows the symmetric plane of the middle, around the X-axis. The last three deposited layers of the sample have stress in comparison, while the layers underneath them are in tension. That happens directly without any gradual changes in the stress values. The most dominant stress type is tension with a small area of compression on the sides. Also, there is a hump on the center which may be caused by the clamps because the clamps prevent the printed part from distortion, which is to stress. In fact, after cooling, when the clamps are removed the stresses could not change the shape of the sample, thereby, turning to residual stresses.

Figure 3.33 σ_{XX}- Longitudinal Residual stress of 3D printed S355 at heat input 405 J/mm X-Z plane -cross section view

Figure 3.34 shows different dominant stress types from outside the sample, this side of the sample on the figure generally in compression state. Also, it has the last three deposited layers, but with a sharp little gradual transformation between compression and tension states. The effect of the clamps still exists on this side as well.

Figure 3.34 σ_{XX}- Longitudinal Residual stress of 3D printed S355 at heat input 405 J/mm X-Z plane view

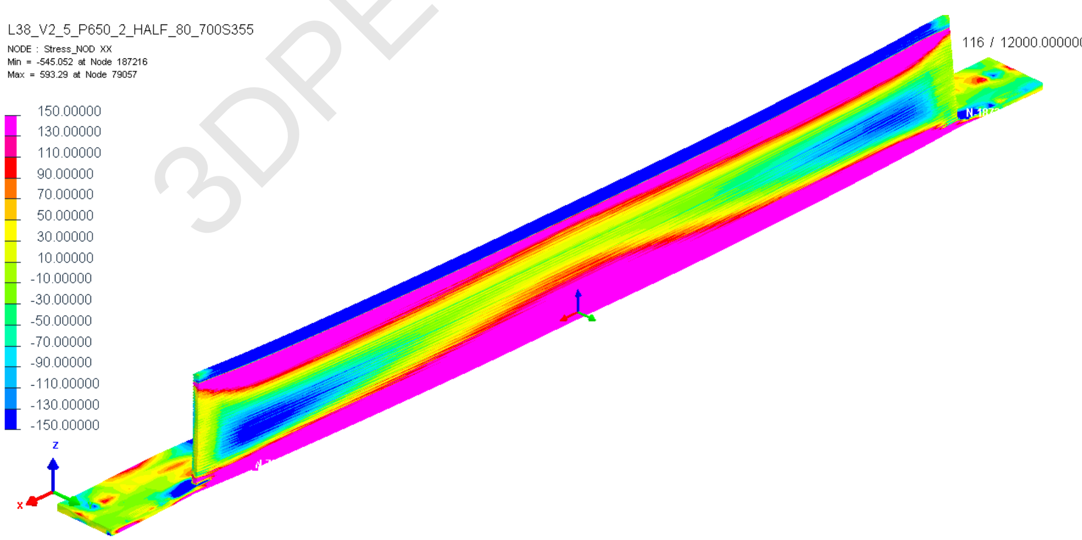

Figure 3.35 σ_{XX}- Longitudinal Residual stress of 3D printed S355 at heat input 405 J/mm Isometric-cross section view

Figures 3.35 and 3.36 are isometric views for the sample, from these figures it is clear that the start and the end of the printing (welding) path have the most effects on the base. The base generally in compression state, which makes sense; because the melting layers shrink and grab the sides of the base with it. While the ends of the base are in a low value of stresses comparing to the center of it.

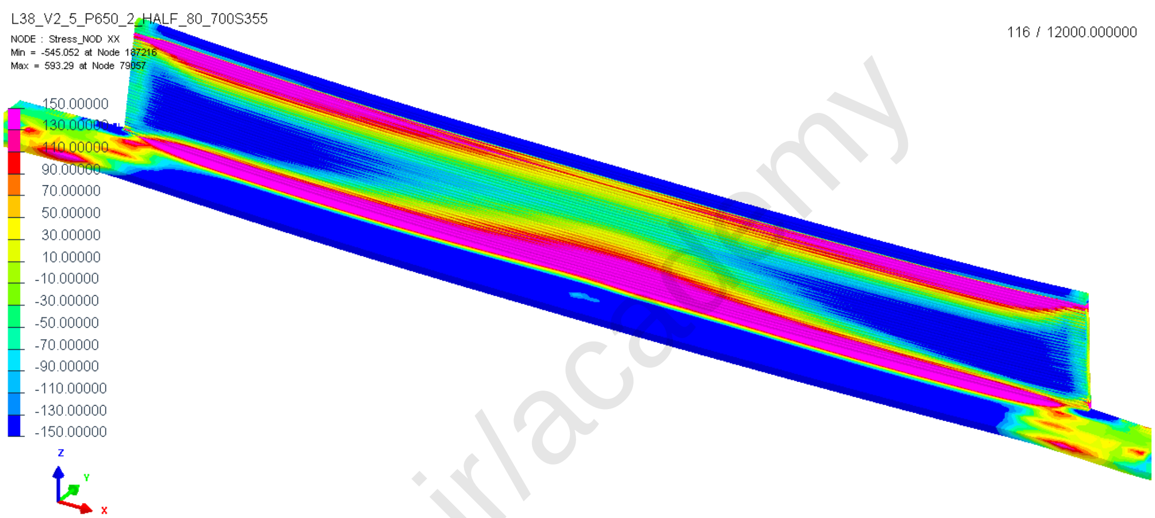

Figure 3.36 σ_{XX}- Longitudinal Residual stress of 3D printed S355 at heat input 405 J/mm Isometric view

Figures 3.37 and 3.38 describe the plane Z-Y with little of rotation. For the same data σ_{XX} residual stress, these figures describe clearly how the tension stresses grow up from outside of the plate to inside it; while the last three layers are in different pattern. Also, these figures show the displacements of the base and the plate as one curve; which is not the case in the sample of 316L. Furthermore, the range of the distortion is lower than the sample of 316L.

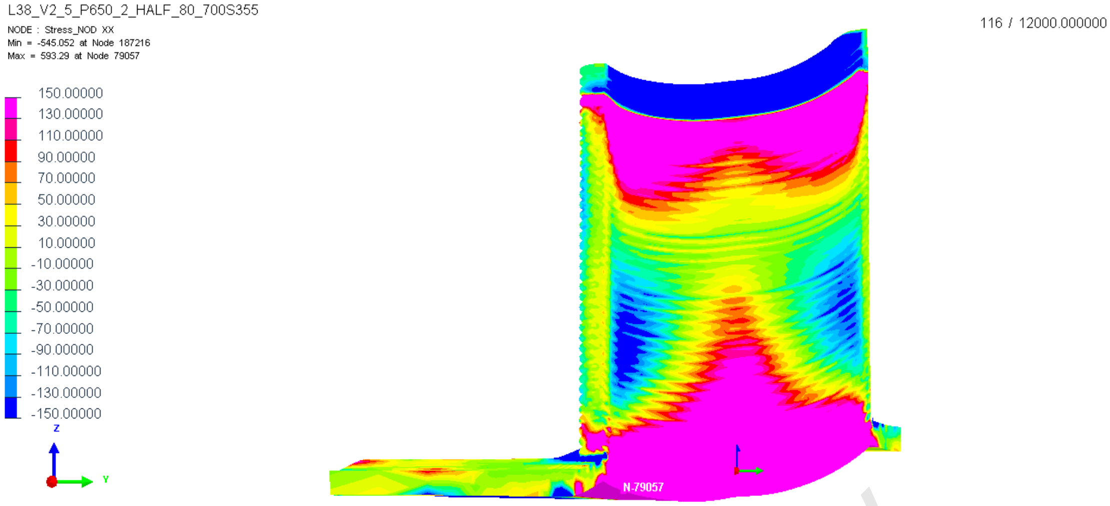

Figure 3.37 σ_{XX}- Longitudinal Residual stress of 3D printed S355 at heat input 405 J/mm Y-Z plane -cross section view

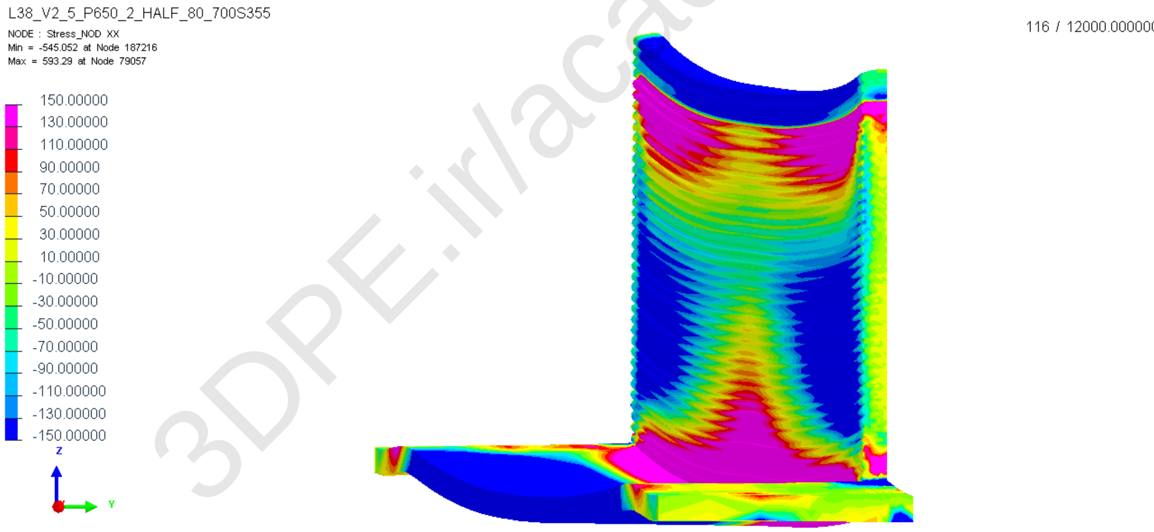

Figure 3.38 σ_{XX}- Longitudinal Residual stress of 3D printed S355 at heat input 405 J/mm Y-Z plane view

Figure 3.39 is a sliced parts of the isometric view of the σ_{XX} residual stress. It seems that the residual stresses inside the cuts are not encompassing the four regions. The contact area between the base and the printed part is in tension, while the second region is in compression and the third region is in tension below the last three layers. The last three layers have a pattern that is different from the others. So, it may be the same as in 316L for the divided regions pattern, but with different range of stress value.

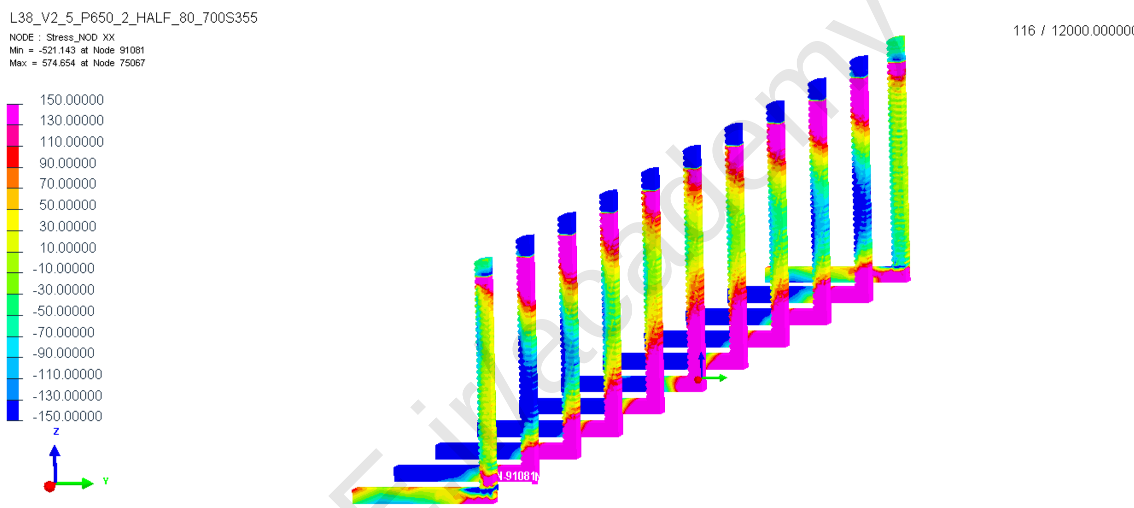

Figure 3.39 σ_{XX}-Longitudinal Residual stress of 3D printed S355 at heat input 405 J/mm Isometric-section-sliced view

First principle Residual Stress result of Low carbon steel S355J2G3 at heat input 405 J/mm

Figure 3.40 is a contour representing the First principle residual stress for internal face from the cross section at the center of the sample. In this figure the stresses are divided into three regions. The last three layers, as in σ_{xx} residual stress, have the lowest rate as compared to other regions. The second region is a frame surrounding the center with tension stresses and it gets high at the origin because of the clamps. The third region is the center which is in between tension and compression states. The maximum stress point is 593.291, in tension, and the minimum is -208.029, in compression.

Figure 3.40 First Principal Residual stress of 3D printed S355 at heat input 405 J/mm X-Z plane -cross section view

Figure 3.41 describes the external face of the sample which is the opposite face of figure 3.40. Figure 3.41 has the same divided regions, but with different dimensions. Moreover, the stress rate of the internal face is in contrast to the external face. In other words, the external surface of the sample has the First principle residual stress in low compression, while the inside of the printed part is in tension state.

Figure 3.41 First Principal Residual stress of 3D printed S355 at heat input 405 J/mm X-Z plane view

Figure 3.42 and 3.43 are isometric views of the same sample. In these two figures, the base area around the printed part is in tension, while the rest of the base area is in low compression, except the ends of the base, which have a combined stress.

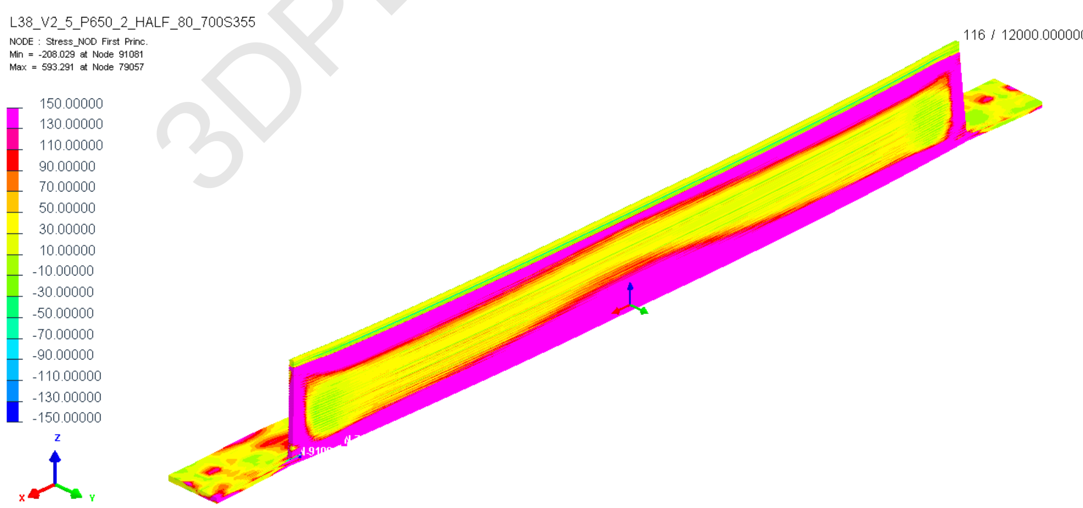

Figure 3.42 First Principal Residual stress of 3D printed S355 at heat input 405 J/mm Isometric-cross section view

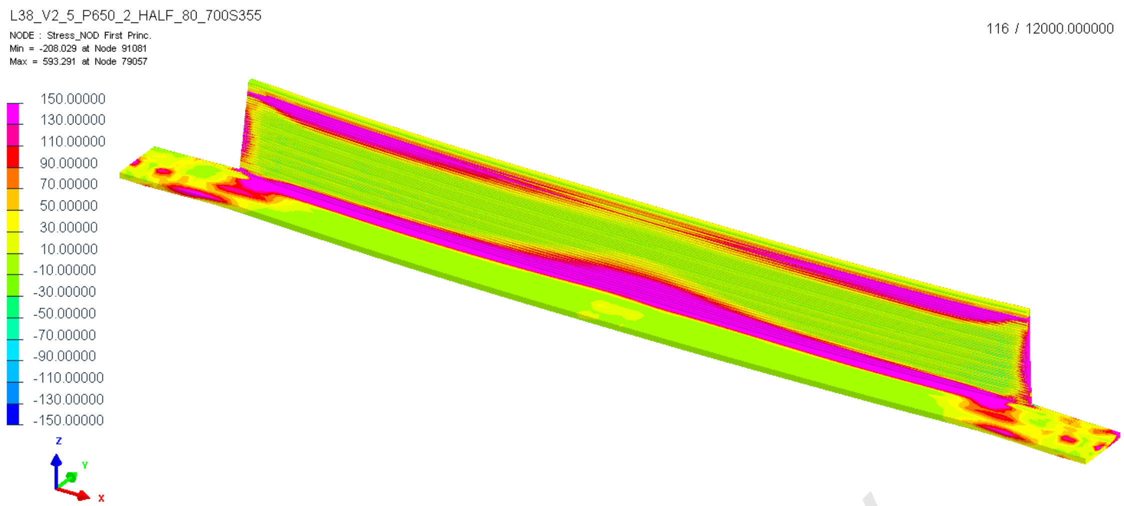

Figure 3.43 First Principal Residual stress of 3D printed S355 at heat input 405 J/mm Isometric view

Figures 3.44 and 3.45 show the last three layers clearly in a different pattern, as what happens in longitudinal stress. Also, in these two figures, the boundaries of any layer are in a state different from the layer itself. This may be because of the re-melting processes during printing. Also, it is observed that the ends of the printed part are in complete tension state.

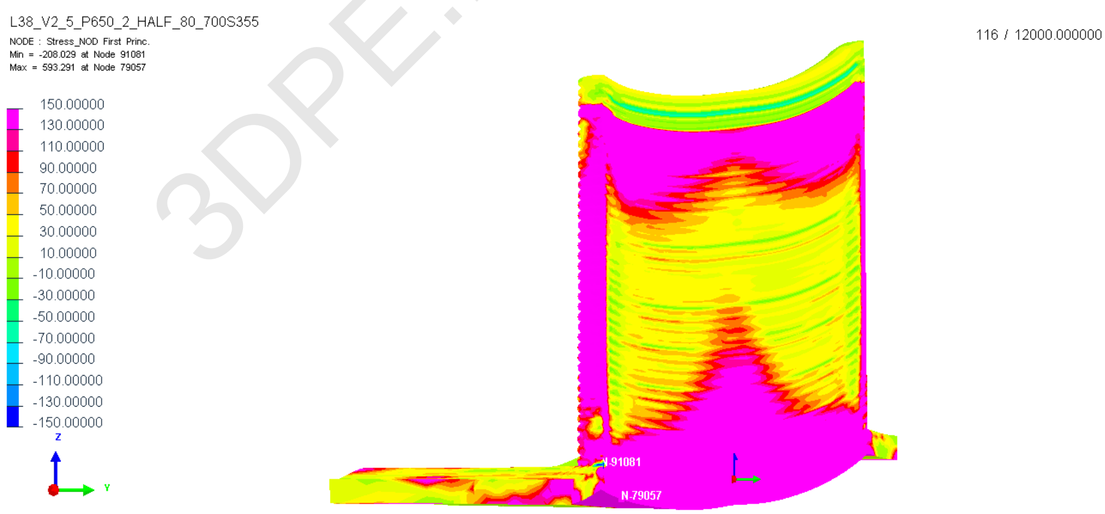

Figure 3.44 First Principal Residual stress of 3D printed S355 at heat input 405 J/mm Y-Z plane -cross section view

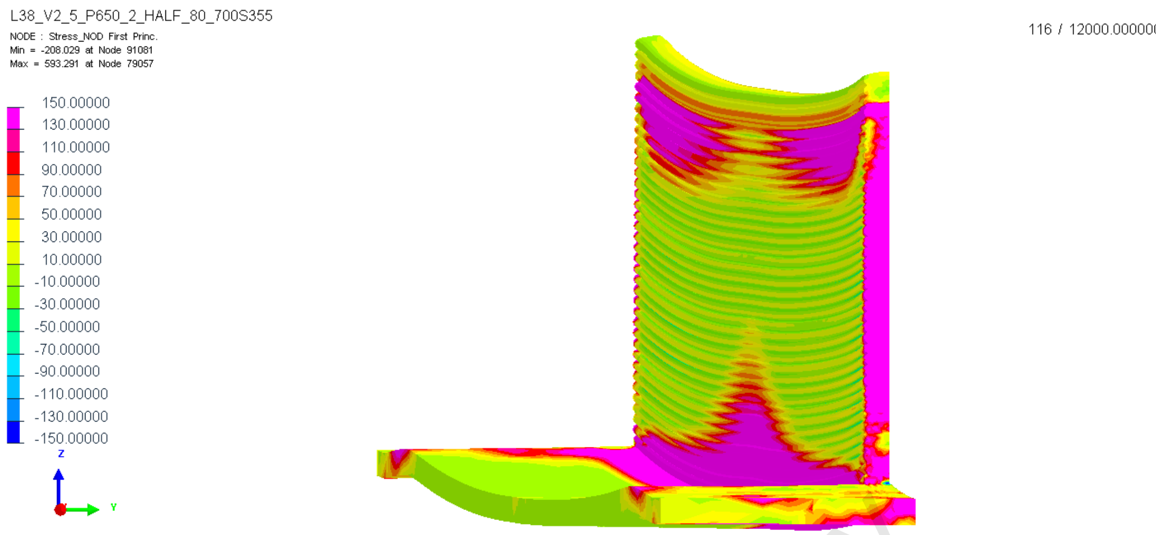

Figure 3.45 First Principal Residual stress of 3D printed S355 at heat input 405 J/mm Y-Z plane view

Figure 3.46 is a sliced parts of the sample. It shows how the stresses transform from the outside of the surface to the inside. Also, it shows how the base holds the printed part using tension stress. In fact, the ends of the printed part are in complete tension stress state. So, the frame is not a rectangular but resembles that of sunglasses, somewhat.

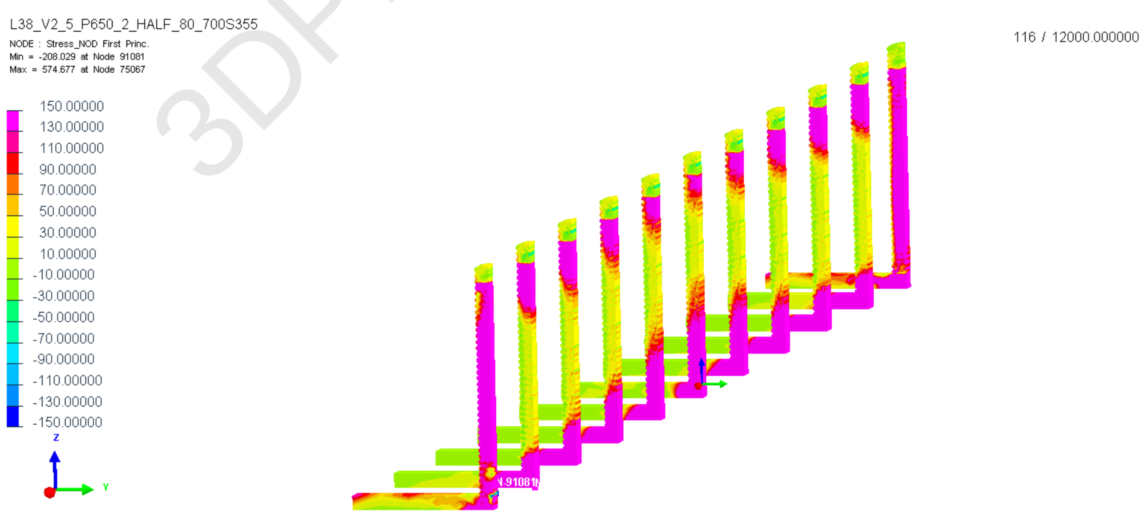

Figure 3.46 First Principal Residual stress of 3D printed S355 at heat input 405 J/mm Isometric-sectioncut-sliced view

Figure 3.47 has curves of Z-axis displacement of selected layers 3-14-25-36. These curves take an arc shape with little distortion in the middle. The sample moves to the negative Z-axis, which is practically impossible, since in real life there would be some support, for e.g. a table holding it. But in simulation processes, the clamps are free after the 3D printing processes is over, which is the cause for the negative sign. If this is factored, the maximum displacement would be around 8 cm, which is 1% of the total sample length.

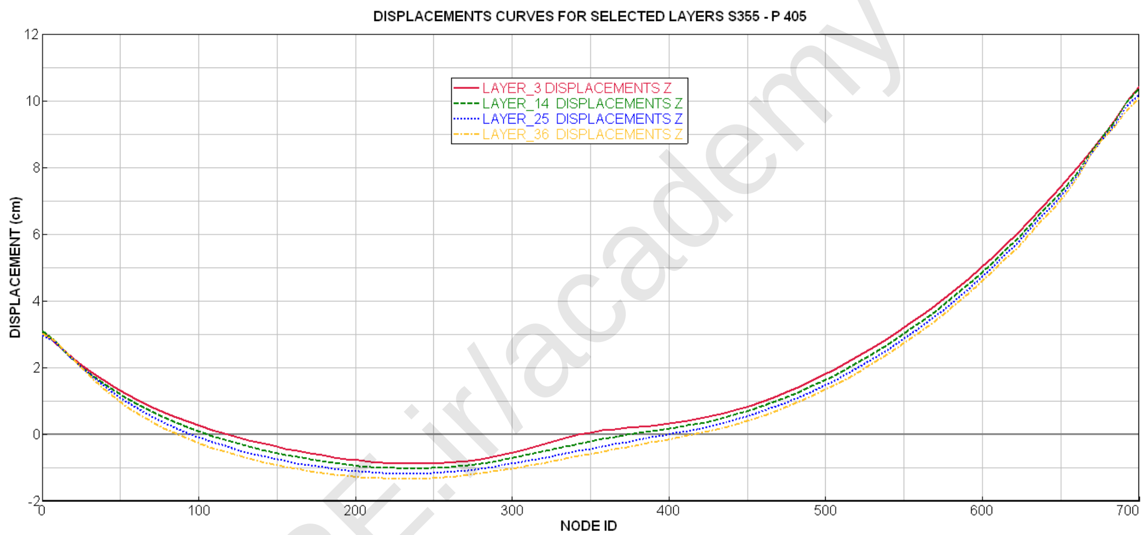

Figure 3.47 Displacements curves for Layers 3-14-25-36 of S355 , heat input 405 /mm after printing

Discussion

These results are made to compare between the residual stresses behaviors of two types of materials. In this case, they were - Austenitic stainless-steel grade 316L and Low carbon steel S355J2G3. These will be tested and validated subsequently with reference to an experimental sample in the future. There are two individuals' sections – one for austenitic stainless-steel grade 316L and the other for Low carbon steel S355J2G3.

In this study, there were two result sections for the austenitic stainless-steel grade 316L - one had heat input rate of 325 J/mm and the other one had 345 J/mm. For lower heat input, the sample nodes did not meet the melting temperature in certain cases, for e.g. the side nodes. Therefore, for these two results, the temperature of the nodes did not affect the final residual stress result so long as the temperature of the nodes reach close to a difference of less than almost200 degree Celsius. In general, the result looks similar but are really not identical; In fact, for the maximum and the minimum temperatures, they appear the same.

In conclusion, the methodology of employing the Welding heat input law or using Smart Weld software are very useful means to predict the appropriate heat input required to produce an explainable result for evidencing residual stresses.

So, the comparison is between two results, instead of three, since the heat input does not impact the result. In general, the stainless-steel result depicts the effect of lower longitudinal and first principle residual stress more, as compared to carbon steel. Though in both materials the residual stress types exceed the yielding strength, they do not suffice the tensile strength parameters.

For the longitudinal residual stress, in this case σ_{XX} residual stress being the longitudinal, the stainless-steel result has more compression stress while the carbon steel was observed to be in complex distribution between the inside and outside surfaces. But in general, tension areas are on the top and on the bottom of the printed part for both materials. On the other side, compression area is the central area of the printed part. Furthermore, the clamps on Y-axis and zero X-axis increase the rate of the tension stresses of the printed part, which is parallel to these clamps. So, for σ_{XX} residual stresses, the tension stress is focused around the base and the top of the printed part for both materials. In contrast, the middle area is in compression. In addition, the inside surface of the printed part tends to have the opposite properties of the stresses type of the outside surface. Also, the clamps must be tested for other conditions in order to identify their effects on residual stresses.

The second kind of stress, namely the First principle residual stresses, shows lesser complexity among the σ_{XX} residual stresses. For this kind of stress, the colorful contours show two different clear areas. One is a frame around the second which is usually in a high rate of tension stress, while the second area is one which appears to be of compression stress type with a low rate, as compared to the frame area. In comparison with the yield strength, the frame area is in a state close to the yielding strength. The internal area, which is surrounded by the frame area, has a very low value relative to the yielding strength. As a conclusion, for 3D printing using WAAM, the active useful area is surrounded by a frame of high residual stress area. So, it is useful to predict the stress distribution by employing simulation processes before the actual printing and machining processes. For both kinds of stresses, the base holds the printed part by tension residual stresses which increase the tension area inside the printed part.

Also, it has to be mentioned that the last three layers of the carbon steel sample have different stress types from the area below them.

The last point is that of the Z-axis displacement in both cases. For stainless steel the distortion is higher than that in carbon steel. In stainless steel it may reach twice the displacement of carbon steel, after the cooling processes. They are both distorted at the ends of the printing path, which is understandable, since the ends are held by the center area of the printed part. Also, stainless steel has a concave area in the middle of the sample, while in the carbon steel sample, this area looks like an arc.

For the computation time for the simulation processes in SYSWELD with a workstation has 16 GB as RAM and around 600 GB as storages, each case took at least 5 days to simulate the 3D printing processes as WAAM; and for the memory requirements, it needs more than 400 GB for the data and the result. For more accuracy by using finer mesh size, the requirements should be higher than the mentioned numbers.

Bottom line is that while the austenitic stainless-steel grade 316L sample has lower longitudinal and first principle residual stresses, low carbon steel S355J2G3 sample has higher longitudinal and first principle residual stresses. In addition, the austenitic stainless-steel grade 316L sample has higher Z-axis displacement, while low carbon steel S355J2G3 sample has the lower Z-axis displacement.

Chapter 4 Conclusion and future work

WAAM 3D printing is one of the promising technologies of the future. For reducing expenses related to such printing, simulation processes are a very effective in predicting the properties of the printed parts after the entire process is done. WAAM is considered as one of the lower priced 3D printers for metals.

It should, however, be noted that before fully trusting this above-mentioned simulation processes, the methodology should undergo several tests as mentioned in the second chapter - Heat test, Path test, Mesh test, Penetration test, and Clamping test. These tests determine the appropriate conditions to be employed in the simulation processes. SYSWELD is a commercial welding simulation software and has one of the higher computational ability among software packages used for welding. Since WAAM is essentially a welding process, adopting SYSWELD in 3D printing is highly recommended.

A 3D printed plate has been printed in Lehigh 3D lab and tested for fatigue. Therefore, in this thesis, for most of the parameters of this experimental sample, a simulation sample has been subject to comprehensive tests. The test results should be applicable to and the sample would represent a range of many similar materials. One of the main objectives of this thesis is to show the residual stresses types in color contour plots for comprehensiveness and clarity. As mentioned earlier, the simulation samples used were austenitic stainless-steel grade 316L and Low carbon steel S355J2G3 as materials for the 3D printing processes.

The primary result is to demonstrate Longitudinal residual stress (σ_{XX}) and First principle residual stresses. The main outcome for longitudinal residual stress (σ_{XX}) is that the austenitic stainless-steel grade 316L sample has lower rate than Low carbon steel S355J2G3, and in both cases there are three main areas of stress types. The top and the bottom areas are in the same residual stress type, and the middle area contrasts with these areas. In both the materials' samples, the residual stress exceeds the yielding strength, but not tensile strength.

A main finding for the First principle residual stresses is that in both samples, for the materials, namely austenitic stainless-steel grade 316L and Low carbon steel S355J2G3, the residual stress made a frame of tension stress around the middle area. This meant that the boundaries of the plate have a different residual stress type than the middle area. As in the longitudinal residual stress, the First principle residual stress exceeds the yielding strength in certain spots. Also, it is higher in Low carbon steel S355J2G3 than in austenitic stainless-steel grade 316L.

Lastly, the Z-axis displacement is high in the austenitic stainless-steel grade 316L sample and it is low in other sample of Low carbon steel S355J2G3. The main reason for this is that the ductility of stainless steel is higher than that of carbon steel. This allows the residual stress to deform the samples.

The next step for this research is to validate and verify the simulation sample with an experimental sample for the identical properties of WAAM. This would contribute, in great measure, a high trust factor in the simulation exercise. Also, based on observations from the simulation sample, the residual stresses were very high; this provides a great opportunity to look for a solution to reduce them by using heat treatment or modifying welding parameters. And for effecting physical changes, the dimension of the base could change the value of the residual stresses. Besides the exhibited and proven effects of the clamps, other clamping conditions could also alter the behavior of residual stresses.

Reference

[1] J. Du, Z. Wei, X. Wang, X. Fang, and G. Zhao, "A novel high-efficiency methodology for metal additive manufacturing," *Appl. Phys. A Mater. Sci. Process.*, vol. 122, no. 11, pp. 1–10, 2016.

[2] I. Gibson, D. Rosen, and B. Stucker, "Additive Manufacturing Technologies," pp. 351–374, 2015.

[3] W. Gao *et al.*, "The status, challenges, and future of additive manufacturing in engineering," *CAD Comput. Aided Des.*, vol. 69, pp. 65–89, 2015.

[4] L. Yang *et al.*, *Additive Manufacturing of Metals: The Technology, Materials, Design and Production*. 2017.

[5] P. A. Colegrove, "High deposition rate high quality metal addi- tive manufacture using wire + are technology," 2010.

[6] J. Ding *et al.*, "Thermo-mechanical analysis of Wire and Arc Additive Layer Manufacturing process on large multi-layer parts," *Comput. Mater. Sci.*, vol. 50, no. 12, pp. 3315–3322, 2011.

[7] T. Wohlers and T. Gornet, "History of additive manufacturing Introduction of non-SL systems Introduction of low-cost 3D printers," *Wohlers Rep. 2012*, pp. 1–23, 2012.

[8] D. Bourell *et al.*, "Materials for additive manufacturing," *CIRP Ann. - Manuf. Technol.*, vol. 66, no. 2, pp. 659–681, 2017.

[9] Y. Zhai, D. A. Lados, and J. L. Lagoy, "Additive Manufacturing: Making imagination the major Limitation," *Jom*, vol. 66, no. 5, pp. 808–816, 2014.

[10] B. A. Szost *et al.*, "A comparative study of additive manufacturing techniques: Residual stress and microstructural analysis of CLAD and WAAM printed Ti-6Al-4V components," *Mater. Des.*, vol. 89, pp. 559–567, 2016.

[11] J. Ding, P. Colegrove, J. Mehnen, S. Williams, F. Wang, and P. S. Almeida, "A computationally efficient finite element model of wire and arc additive manufacture," *Int. J. Adv. Manuf. Technol.*, vol. 70, no. 1–4, pp. 227–236, 2014.

[12] A. Busachi, J. Erkoyuncu, P. Colegrove, F. Martina, C. Watts, and R. Drake, "A review of Additive Manufacturing technology and Cost Estimation techniques for the defence sector," *CIRP J. Manuf. Sci. Technol.*, vol. 19, pp. 117–128, 2017.

[13] D. Yang, C. He, and G. Zhang, "Forming characteristics of thin-wall steel parts by double electrode GMAW based additive manufacturing," *J. Mater. Process. Technol.*, vol. 227, pp. 153–160, 2016.

[14] M. Seifi, A. Salem, J. Beuth, O. Harrysson, and J. J. Lewandowski, "Overview of Materials Qualification Needs for Metal Additive Manufacturing," *Jom*, vol. 68, no. 3, pp. 747–764, 2016.

[15] D. Ding, Z. Pan, C. Dominic, and H. Li, “Robotic Welding, Intelligence and Automation,” vol. 88, 2011.

[16] C. Dordlofva, A. Lindwall, and P. Törlind, “Opportunities and Challenges for Additive Manufacturing in Space Applications,” *Proc. Nord. 2016*, 2016.

[17] H. Bikas, P. Stavropoulos, and G. Chryssolouris, “Additive manufacturing methods and modeling approaches: A critical review,” *Int. J. Adv. Manuf. Technol.*, vol. 83, no. 1–4, pp. 389–405, 2016.

[18] D. Ding, Z. Pan, D. Cuiuri, and H. Li, “A tool-path generation strategy for wire and arc additive manufacturing,” *Int. J. Adv. Manuf. Technol.*, vol. 73, no. 1–4, pp. 173–183, 2014.

[19] J. Ruan, T. E. Sparks, Z. Fan, J. K. Stroble, and A. Panackal, “No Title,” pp. 233–245.

[20] X. Bai, H. Zhang, and G. Wang, “Improving prediction accuracy of thermal analysis for weld-based additive manufacturing by calibrating input parameters using IR imaging,” *Int. J. Adv. Manuf. Technol.*, vol. 69, no. 5–8, pp. 1087–1095, 2013.

[21] N. Guo and M. C. Leu, “Additive manufacturing: Technology, applications and research needs,” *Front. Mech. Eng.*, vol. 8, no. 3, pp. 215–243, 2013.

[22] T. Abe and H. Sasahara, “Dissimilar metal deposition with a stainless steel and nickel-based alloy using wire and arc-based additive manufacturing,” *Precis. Eng.*, vol. 45, pp. 387–395, 2016.

[23] C. M. Lee, W. S. Woo, J. T. Baek, and E. J. Kim, “Laser and arc manufacturing processes: A review,” *Int. J. Precis. Eng. Manuf.*, vol. 17, no. 7, pp. 973–985, 2016.

[24] J. Džugan and Z. Nový, “Powder Application in Additive Manufacturing of Metallic Parts,” L. A. B. T.-P. M.-F. and C. S. Dobrzanski, Ed. Rijeka: InTech, 2017, p. Ch. 08.

[25] M. Megahed, H.-W. Mindt, N. N’Dri, H. Duan, and O. Desmaison, *Metal additive-manufacturing process and residual stress modeling*, vol. 5, no. 1. Integrating Materials and Manufacturing Innovation, 2016.

[26] J. J. Yan *et al.*, “Selective laser melting of H13: microstructure and residual stress,” *J. Mater. Sci.*, vol. 52, no. 20, pp. 12476–12485, 2017.

[27] Z. Fan and F. Liou, “Numerical Modeling of the Additive Manufacturing (AM) Processes of Titanium Alloy,” *Titan. Alloy. - Towar. Achiev. Enhanc. Prop. Divers. Appl.*, no. March 2015, 2012.

[28] D. Ding, Z. Pan, D. Cuiuri, and H. Li, “A multi-bead overlapping model for robotic wire and arc additive manufacturing (WAAM),” *Robot. Comput. Integr. Manuf.*, vol. 31, pp. 101–110, 2015.

[29] Y. Ma, D. Cuiuri, N. Hoye, H. Li, and Z. Pan, “Effects of wire feed conditions on in situ alloying and additive layer manufacturing of titanium aluminides using gas tungsten arc welding,” *J. Mater. Res.*, vol. 29, no. 17, pp. 2066–2071, 2014.

[30] Z. Pan, D. Ding, B. Wu, and D. Cuiuri, “Arc Welding Processes for Additive Manufacturing: A Review,” no. 2, pp. 3–24, 2018.

[31] W. J. Sames, F. A. List, S. Pannala, R. R. Dehoff, and S. S. Babu, "The metallurgy and processing science of metal additive manufacturing," *Int. Mater. Rev.*, vol. 61, no. 5, pp. 315–360, 2016.

[32] Y. Zhang *et al.*, "Additive Manufacturing of Metallic Materials: A Review," *J. Mater. Eng. Perform.*, vol. 27, no. 1, 2018.

[33] M. J. Bermingham, D. Kent, H. Zhan, D. H. Stjohn, and M. S. Dargusch, "Controlling the microstructure and properties of wire arc additive manufactured Ti-6Al-4V with trace boron additions," *Acta Mater.*, vol. 91, pp. 289–303, 2015.

[34] D. Ding, Z. Pan, D. Cuiuri, and H. Li, "Wire-feed additive manufacturing of metal components: technologies, developments and future interests," *Int. J. Adv. Manuf. Technol.*, vol. 81, no. 1–4, pp. 465–481, 2015.

[35] D. Herzog, V. Seyda, E. Wycisk, and C. Emmelmann, "Additive manufacturing of metals," *Acta Mater.*, vol. 117, pp. 371–392, 2016.

[36] C. Shen, Z. Pan, D. Cuiuri, J. Roberts, and H. Li, "Fabrication of Fe-FeAl Functionally Graded Material Using the Wire-Arc Additive Manufacturing Process," *Metall. Mater. Trans. B*, vol. 47, no. 1, pp. 763–772, 2016.

[37] O. Yilmaz and A. A. Ugla, "Development of a cold wire-feed additive layer manufacturing system using shaped metal deposition method," *J. Mech. Sci. Technol.*, vol. 31, no. 4, pp. 1611–1620, 2017.

[38] F. Montevecchi, G. Venturini, A. Scippa, and G. Campatelli, "Finite Element Modelling of Wire-arc-additive-manufacturing Process," *Procedia CIRP*, vol. 55, pp. 109–114, 2016.

[39] H. Geng, J. Xiong, D. Huang, X. Lin, and J. Li, "A prediction model of layer geometrical size in wire and arc additive manufacture using response surface methodology," *Int. J. Adv. Manuf. Technol.*, vol. 93, no. 1–4, pp. 175–186, 2017.

[40] J. Donoghue, A. A. Antonysamy, F. Martina, P. A. Colegrove, S. W. Williams, and P. B. Prangnell, "The effectiveness of combining rolling deformation with Wire-Arc Additive Manufacture on β-grain refinement and texture modification in Ti-6Al-4V," *Mater. Charact.*, vol. 114, pp. 103–114, 2016.

[41] F. Xu *et al.*, "Multi-Sensor System for Wire-Fed Additive Manufacture of Titanium Alloys," *26th Int. Conf. Flex. Autom. Intell. Manuf. (FAIM 2016)*, no. January 2017, p. Article in Press, 2016.

[42] G. Venturini, F. Montevecchi, A. Scippa, and G. Campatelli, "Optimization of WAAM Deposition Patterns for T-crossing Features," *Procedia CIRP*, vol. 55, pp. 95–100, 2016.

[43] J. Xiong, Z. Yin, and W. Zhang, "Forming appearance control of arc striking and extinguishing area in multi-layer single-pass GMAW-based additive manufacturing," *Int. J. Adv. Manuf. Technol.*, vol. 87, no. 1–4, pp. 579–586, 2016.

[44] J. Gockel and J. Beuth, "Understanding Ti-6Al-4V Microstructure Control in Additive Manufacturing via Process Maps Joy Gockel and Jack Beuth Department of Mechanical Engineering, Carnegie Mellon University, Pittsburgh, PA 15213," *Solid Free. Fabr. Proc.*, pp.

666–674, 2013.

[45] G. Manogharan, B. Yelamanchi, R. Aman, and Z. Mahbooba, “Experimental Study of Disruption of Columnar Grains During Rapid Solidification in Additive Manufacturing,” *Jom*, vol. 68, no. 3, pp. 842–849, 2016.

[46] Y. Liu, Y. Yang, and D. Wang, “A study on the residual stress during selective laser melting (SLM) of metallic powder,” *Int. J. Adv. Manuf. Technol.*, pp. 1–10, 2016.

[47] Sarah Saunders, “After Successful Testing and Verification, 3D Printed WAAMpeller is Introduced to the Public,” 2017. [Online]. Available: https://3dprint.com/195791/3d-printed-waampeller-verified/.

[48] A. Busachi, J. Erkoyuncu, P. Colegrove, F. Martina, and J. Ding, “Designing a WAAM based manufacturing system for defence applications,” *Procedia CIRP*, vol. 37, no. 2013, pp. 48–53, 2015.

[49] A. Haboudou, P. Peyre, A. B. Vannes, and G. Peix, “Reduction of porosity content generated during Nd: YAG laser welding of A356 and AA5083 aluminium alloys,” *Mater. Sci. Eng. A*, vol. 363, no. 1–2, pp. 40–52, 2003.

[50] S. W. Williams, F. Martina, A. C. Addison, J. Ding, G. Pardal, and P. Colegrove, “Wire + Arc Additive Manufacturing,” *Mater. Sci. Technol.*, vol. 32, no. 7, pp. 641–647, 2016.

[51] J. Y. Bai, C. L. Yang, S. B. Lin, B. L. Dong, and C. L. Fan, “Mechanical properties of 2219-Al components produced by additive manufacturing with TIG,” *Int. J. Adv. Manuf. Technol.*, vol. 86, no. 1–4, pp. 479–485, 2016.

[52] PandeyM. and Pulak, “Rapid prototyping technologies, applications and part deposition planning,” *Retrieved Oct.*, no. June, p. 15, 2010.

[53] X. Zhou and C. Liu, “Three-dimensional Printing for Catalytic Applications: Current Status and Perspectives,” *Adv. Funct. Mater.*, vol. 1701134, p. 1701134, 2017.

[54] W. World, L. E. Soudage, D. Le, T. Guwahati, and T. Bombay, “In Fusion Welding Process Simulation EFFICIENT ESTIMATION OF VOLUMETRIC HEAT SOURCE IN FUSION WELDING PROCESS SIMULATION,” vol. 56, no. January 2016, pp. 88–97, 2013.

[55] P. Pratt, S. D. Felicelli, L. Wang, and C. R. Hubbard, “Residual stress measurement of laser-engineered net shaping AISI 410 thin plates using neutron diffraction,” *Metall. Mater. Trans. A Phys. Metall. Mater. Sci.*, vol. 39, no. 13, pp. 3155–3163, 2008.

[56] T. Kik, M. Slovacek, J. Moravec, and M. Vanek, “Numerical Simulations of Heat Treatment Processes,” *Appl. Mech. Mater.*, vol. 809–810, pp. 799–804, 2015.

[57] M. Moradi Eshkafti, “Influence of various welding sequence schemes on the load bearing capacity of square hollow section T-joint.,” vol. 35, no. 4, pp. 41–50, 2017.

[58] C. V. Haden, G. Zeng, F. M. Carter, C. Ruhl, B. A. Krick, and D. G. Harlow, “Wire and arc additive manufactured steel: Tensile and wear properties,” *Addit. Manuf.*, vol. 16, pp. 115–123, 2017.

[59] V. M. J. Varghese, M. R. Suresh, and D. S. Kumar, “Recent developments in modeling of

heat transfer during TIG welding—a review," *Int. J. Adv. Manuf. Technol.*, vol. 64, no. 5–8, pp. 749–754, 2013.

[60] D. Deng and H. Murakawa, "Numerical simulation of temperature field and residual stress in multi-pass welds in stainless steel pipe and comparison with experimental measurements," *Comput. Mater. Sci.*, vol. 37, no. 3, pp. 269–277, 2006.

[61] G. Casalino and A. D. Ludovico, "Finite element simulation of high speed pulse welding of high specific strength metal alloys," *J. Mater. Process. Technol.*, vol. 197, no. 1–3, pp. 301–305, 2008.

[62] S. Murugan, S. Rai, and P. Kumar, "Temperature distribution and residual stresses due to multipass welding in type 304 stainless steel and low carbon steel weld pads," *Int. J. …*, vol. 78, no. 4, pp. 307–317, 2001.

[63] R. K. Chin, J. L. Beuth, and C. H. Amon, "Successive deposition of metals in solid freeform fabrication processes, Part 1: thermomechanical models of layers and droplet columns," *J. Manuf. Sci. Eng.*, vol. 123, no. 4, pp. 623–631, 2001.

[64] R. K. Chin, J. L. Beuth, and C. H. Amon, "Successive Deposition of Metals in Solid Freeform Fabrication Processes, Part 2: Thermomechanical Models of Adjacent Droplets," *J. Manuf. Sci. Eng.*, vol. 123, no. 4, pp. 632–638, May 2000.

[65] J. Mehnen, J. Ding, H. Lockett, and P. Kazanas, "Global Product Development," pp. 721–727, 2011.

[66] D. Yang, G. Wang, and G. Zhang, "Thermal analysis for single-pass multi-layer GMAW based additive manufacturing using infrared thermography," *J. Mater. Process. Technol.*, vol. 244, pp. 215–224, 2017.

[67] S. Suryakumar, K. P. Karunakaran, U. Chandrasekhar, and M. A. Somashekara, "A study of the mechanical properties of objects built through weld-deposition," *Proc. Inst. Mech. Eng. Part B J. Eng. Manuf.*, vol. 227, no. 8, pp. 1138–1147, 2013.

[68] M. P. Mughal, H. Fawad, and R. A. Mufti, "Three-dimensional finite-element modelling of deformation in weld-based rapid prototyping," *Proc. Inst. Mech. Eng. Part C J. Mech. Eng. Sci.*, vol. 220, no. 6, pp. 875–885, 2006.

[69] P. A. Colegrove *et al.*, "Microstructure and residual stress improvement in wire and arc additively manufactured parts through high-pressure rolling," *J. Mater. Process. Technol.*, vol. 213, no. 10, pp. 1782–1791, 2013.

[70] J. Ding, "Thermo-mechanical Analysis of Wire and Arc Additive Manufacturing Process," no. January, p. 216, 2012.

[71] X. Qiu, "Effect of rolling on fatigue crack growth rate of Wire and Arc Additive Manufacture (WAAM) processed Titanium," no. November, pp. 2012–2013, 2013.

[72] Z. Feng, *Processes and mechanisms of welding residual stress and distortion*. Elsevier, 2005.

[73] P. Staron, M. Koçak, S. Williams, and A. Wescott, "Residual stress in friction stir-welded A1 sheets," *Phys. B Condens. Matter*, vol. 350, no. 1–3 SUPPL. 1, pp. 491–493, 2004.

[74] D. A. Price *et al.*, “Distortion control in welding by mechanical tensioning,” *Sci. Technol. Weld. Join.*, vol. 12, no. 7, pp. 620–633, 2007.

[75] J. Altenkirch, A. Steuwer, P. J. Withers, S. W. Williams, M. Poad, and S. W. Wen, “Residual stress engineering in friction stir welds by roller tensioning,” *Sci. Technol. Weld. Join.*, vol. 14, no. 2, pp. 185–192, 2009.

[76] S. W. Wen, P. A. Colegrove, S. W. Williams, S. A. Morgan, A. Wescott, and M. Poad, “Rolling to control residual stress and distortion in friction stir welds,” *Sci. Technol. Weld. Join.*, vol. 15, no. 6, pp. 440–447, 2010.

[77] C. L. Tsai, S. C. Park, and W. T. Cheng, “Welding Distortion of a Thin-Plate Panel Structure,” *Am. Weld. Soc. - Weld. J.*, no. May, pp. 156–165, 1999.

[78] T. L. Teng, P. H. Chang, and W. C. Tseng, “Effect of welding sequences on residual stresses,” *Comput. Struct.*, vol. 81, no. 5, pp. 273–286, 2003.

[79] I. Sattari-Far and Y. Javadi, “Influence of welding sequence on welding distortions in pipes,” *Int. J. Press. Vessel. Pip.*, vol. 85, no. 4, pp. 265–274, 2008.

[80] Y. A. Song, S. Park, and S. W. Chae, “3D welding and milling: Part II - Optimization of the 3D welding process using an experimental design approach,” *Int. J. Mach. Tools Manuf.*, vol. 45, no. 9, pp. 1063–1069, 2005.

[81] A. H. Nickel, D. M. Barnett, and F. B. Prinz, “Thermal stresses and deposition patterns in layered manufacturing,” *Mater. Sci. Eng. A*, vol. 317, no. 1–2, pp. 59–64, 2001.

[82] M. P. Mughal, R. A. Mufti, and H. Fawad, “The mechanical effects of deposition patterns in welding-based layered manufacturing,” *Proc. Inst. Mech. Eng. Part B J. Eng. Manuf.*, vol. 221, no. 10, pp. 1499–1509, 2007.

[83] M. V. Deo and P. Michaleris, “Mitigation of welding induced buckling distortion using transient thermal tensioning,” *Sci. Technol. Weld. Join.*, vol. 8, no. 1, pp. 49–54, 2003.

[84] N. W. Klingbeil, J. L. Beuth, R. K. Chin, and C. H. Amon, “Residual stress-induced warping in direct metal solid freeform fabrication,” *Int. J. Mech. Sci.*, vol. 44, no. 1, pp. 57–77, 2002.

[85] R. Jendrzejewski, G. Śliwiński, M. Krawczuk, and W. Ostachowicz, “Temperature and stress fields induced during laser cladding,” *Comput. Struct.*, vol. 82, no. 7–8, pp. 653–658, 2004.

[86] P. Michaleris and A. Debiccari, “Prediction of welding distortion,” *Am. Weld. Soc. - Weld. J.*, vol. 76, no. April, p. 172–s, 1997.

[87] K. Masubuchi, *Analysis of welded structures: residual stresses, distortion, and their consequences*, vol. 33. Elsevier, 2013.

[88] K. Li, J. Chen, and Y. Zhang, “Double-electrode GMAW process and control,” *Weld. J.*, pp. 231–237, 2007.

[89] K. H. Li and Y. M. Zhang, “Consumable Double-Electrode GMAW — Part I : The Process,” *Weld. J.*, vol. 87, no. January, p. 11s–17s, 2008.

[90] K. Li and Y. M. Zhang, “Consumable Double-Electrode GMAW Part II: Monitoring, Modeling, and Control,” *Control*, pp. 1–34, 2007.

[91] Y. M. Zhang, M. Jiang, and W. Lu, “Double electrodes improve GMAW heat input control,” *Weld. J.*, vol. 83, no. 11, pp. 39–41, 2004.

[92] X. Bai, H. Zhang, and G. Wang, “Modeling of the moving induction heating used as secondary heat source in weld-based additive manufacturing,” *Int. J. Adv. Manuf. Technol.*, vol. 77, no. 1–4, pp. 717–727, 2015.

[93] P. Mercelis and J. Kruth, “Residual stresses in selective laser sintering and selective laser melting,” *Rapid Prototyp. J.*, vol. 12, no. 5, pp. 254–265, 2006.

[94] H. Zhao, G. Zhang, Z. Yin, and L. Wu, “A 3D dynamic analysis of thermal behavior during single-pass multi-layer weld-based rapid prototyping,” *Journal of Materials Processing Technology*, vol. 211, no. 3. 2011.

[95] H. Zhao, G. Zhang, Z. Yin, and L. Wu, “Three-dimensional finite element analysis of thermal stress in single-pass multi-layer weld-based rapid prototyping,” *J. Mater. Process. Technol.*, vol. 212, no. 1, pp. 276–285, 2012.

[96] M. P. Mughal, H. Fawad, R. A. Mufti, and M. Siddique, “Deformation modelling in layered manufacturing of metallic parts using gas metal arc welding: effect of process parameters,” *Model. Simul. Mater. Sci. Eng.*, vol. 13, no. 7, p. 1187, 2005.

[97] M. P. Mughal, H. Fawad, and R. Mufti, “Finite element prediction of thermal stresses and deformations in layered manufacturing of metallic parts,” *Acta Mech.*, vol. 183, no. 1–2, pp. 61–79, 2006.

[98] J. D. Spencer, P. M. Dickens, and C. M. Wykes, “Rapid prototyping of metal parts by three-dimensional welding,” *Proc. Inst. Mech. Eng. Part B J. Eng. Manuf.*, vol. 212, no. 3, pp. 175–182, 1998.

[99] J. Fessler, R. Merz, A. Nickel, F. Prinz, and L. Weiss, “Laser deposition of metals for shape deposition manufacturing,” *Solid Free. Fabr. Symp. Proceedings, Univ. Texas Austin*, pp. 117–124, 1996.

[100] R. Jendrzejewski and G. Śliwiński, “Investigation of temperature and stress fields in laser cladded coatings,” *Appl. Surf. Sci.*, vol. 254, no. 4, pp. 921–925, 2007.

[101] L. Costa, R. Vilar, T. Reti, and A. M. Deus, “Rapid tooling by laser powder deposition: Process simulation using finite element analysis,” *Acta Mater.*, vol. 53, no. 14, pp. 3987–3999, 2005.

[102] E. R. Denlinger, J. C. Heigel, P. Michaleris, and T. A. Palmer, “Effect of inter-layer dwell time on distortion and residual stress in additive manufacturing of titanium and nickel alloys,” *J. Mater. Process. Technol.*, vol. 215, pp. 123–131, 2015.

[103] W. C. Spencer DJ, Dickens PM, “Rapid prototyping of metal parts by three dimentional welding,” *Mech E J. Eng. Manuf.*, vol. 212, pp. 175–182, 1998.

[104] J. Xiong, G. Zhang, Z. Qiu, and Y. Li, “Vision-sensing and bead width control of a single-bead multi-layer part: Material and energy savings in GMAW-based rapid manufacturing,” *J. Clean. Prod.*, vol. 41, pp. 82–88, 2013.

[105] J. Xiong and G. Zhang, “Adaptive control of deposited height in GMAW-based layer

additive manufacturing," *J. Mater. Process. Technol.*, vol. 214, no. 4, pp. 962–968, 2014.

[106] Y. M. Zhang, P. Li, Y. Chen, and A. T. Male, "Automated system for welding-based rapid prototyping," *Mechatronics*, vol. 12, no. 1, pp. 37–53, 2002.

[107] Y. M. Zhang, Y. Chen, P. Li, and A. T. Male, "Weld deposition-based rapid prototyping: A preliminary study," *J. Mater. Process. Technol.*, vol. 135, no. 2–3 SPEC., pp. 347–357, 2003.

[108] Y. A. Song and S. Park, "Experimental investigations into rapid prototyping of composites by novel hybrid deposition process," *J. Mater. Process. Technol.*, vol. 171, no. 1, pp. 35–40, 2006.

[109] X. W. Bai, H. O. Zhang, and G. L. Wang, "Electromagnetically confined weld-based Additive Manufacturing," *Procedia CIRP*, vol. 6, pp. 515–520, 2013.

[110] J. V. Gordon, C. V. Haden, H. F. Nied, R. P. Vinci, and D. G. Harlow, "Fatigue crack growth anisotropy, texture and residual stress in austenitic steel made by wire and arc additive manufacturing," *Mater. Sci. Eng. A*, vol. 724, no. March, pp. 431–438, 2018.

Vita

Abdulrahman Alrumayh is born in Unaizah, Saudi Arabia on January 2nd, 1991. He is the third son for his parents Amer and Ruqayyah.

He received a bachelor's degree from Qassim University in 2014, and he started his master program in Lehigh University in January 2017.